Dynamic Control of Network Level Information Processing through Cholinergic Modulation

by

James Patrick Roach

A dissertation submitted in partial fulfillment
of the requirements for the degree of
Doctor of Philosophy
(Neuroscience)
in The University of Michigan
2018

Doctoral Committee:

Professor Michal R. Zochowski, Chair
Assistant Professor Sara J. Aton
Associate Professor Victoria Booth
Professor Geoffrey G. Murphy
Professor Emeritus Leonard M. Sander

Spatiotemporal Patterning

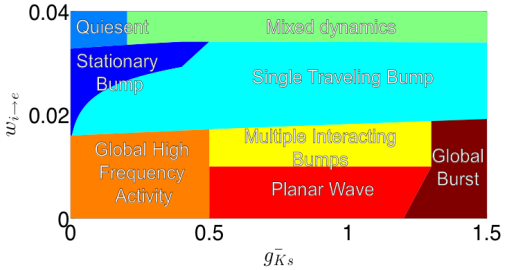

Memory Recall

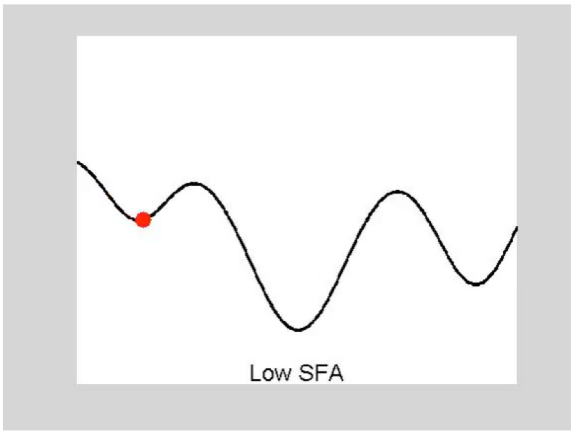

Memory Storage

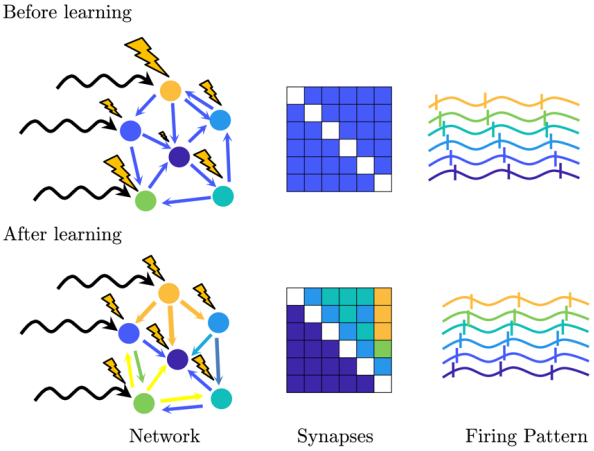

James Patrick Roach

roachjp@umich.edu

ORCID iD: 0000-0002-1034-9615

© James Patrick Roach 2018

To my parents and everyone who has given me a place to stay over the past ten years

ACKNOWLEDGEMENTS

I have often said that being a grad student is the best job I've ever had. This is by far the biggest thing I've ever done. I've made a mark in the world and have helped expand what the world knows about the brain. Graduate school has given me an opportunity to travel to many new places, meet people I'd never have met, and do things that hadn't been invented when I graduated high school. I absolutely didn't do this alone and there are too many people to single out for recognition. First I would like to thank the University of Michigan, the Rackham Graduate School, and the National Science Foundation for financially supporting my education. This institutional backing provided me with the freedom and support to complete my research program.

Without the support of my family I don't know where I'd be. To my parents, Patrick and Rachel: first, thanks for somehow getting me through high school. You were always patient with me no matter how many times I've needed to start over. Thanks for never giving up on me. To my brother Jason: thanks for being the best role model and for always making your home open to me when I needed to get away from it all. It's really true that my brother joined the army and I got to see the world. Laura, my sister: thanks for always being there for me and being one of my closest friends. You're the best. To my uncle Angus and my Aunt Mariana: thanks for feeding me and giving me a couch to sleep on all those years I was in Miami. I would not have finished college without you. Thank you all for your unwavering

support.

Naturally, I'd like to thank my Chair Michal Zochowski. I knew you'd be a great advisor when we would have prolonged arguments about the meaning of data and how the brain actually works. You never shut down any of my ideas, no matter how hare-brained, always allowing me to prove or disprove them. You've taught me how to be a thoughtful scientist by example and always encouraged me to expand my education outside the lab. I'm thankful that you always struck a balance between freedom and oversight. Most of all I want to that you for being a kind supervisor and fostering a friendly lab. I can't imagine doing all this with a better teacher.

Of course I need to thank Len Sander, who has been every much as the teacher Michal has. You taught me how to approach neuroscience from a physical perspective. You brought a skepticism and a focus on predictions to our projects that I hope to emulate. To the rest of my committee, Victoria Booth, Sara Aton, and Geoff Murphy, I appreciate the time you took to advise me over the past four years. Your feedback improved all the work I've done and I've enjoyed our fruitful and collaborative relationships.

I was fortunate to pivot between two groups of great lab mates. All of you have been great friends, travel companions, and coworkers. Thanks for making the office feel like home. To those who were there when I arrived: Chris Fink, Liz Shtrahman, Sima Mofakham, and Dan Maruyama. You guys showed me the ropes when I started. Thanks for all the advice, code, and good times. To Quinton Skilling, Jiaxing Wu, Maral Budak, Bola Eniwaye, and Yihao Yang, who came while I was here, thanks for keeping the office fun, all the help fleshing out my ideas, and putting up with me being silly. You all were great companions during my time at Michigan.

I never would have taken as many opportunities or achieved as much without the

patient assistance and never ending support of the Neuroscience Graduate Program. Everyone in the office provided me with a home at the university and would always address any problems that I had. Edward Stuenkel, thanks for pushing me to take advantage of all the programs available to us and to go to Israel and to Woods Hole. You were always a good source of advice. To Rachael Seidler and Audrey Seasholtz thanks for you dedication to improving an already great program. Finally, to Rachel Harbach, Carol Skala, and Valerie Smith, you three are the backbone of the program and I can't count how many times you've helped me personally.

I would have never gotten to this point without the guidance, support, and motivation from so many people at Florida International University. Both the MARC-USTAR and QBIC programs ignited my interest in science and prepared me exceptionally well for grad school. Philip Stoddard, David Chatfield, Marcy Lowenstein, Ophelia Weeks, and Bryan Dewsbury were professors and teachers that took an interest in me early and never let me give up. Most importantly, my mentor Anya Goldina helped me navigate being a student while doing research and pushing me to achieve my goals. Anya, thank you for recruiting me as a research assistant all those years ago.

I've benefited from the greatest friends a grad student could have while I've been at Michigan. I can't thank you enough for the support, stress relief, and good times. Chris Fitzpatrick you've been my best friend in Michigan and have been a great roommate. Jonte Jones, Veronica Valera, Nicholas Silva, Natalie Nevarez, Caitlin Rodriguez, Jaclyn Durkin, Brittany Kuhn, and Graham Jones: you all have been a well-spring of support and helped me fight my inclination to be alone. Finally, I'd like to thank Kat Miles. Kat always reminded how far I've come from and how well I'm doing. Thanks for being the best friend I've ever had.

TABLE OF CONTENTS

LIST OF FIGURES

Figure

LIST OF TABLES

LIST OF VIDEOS

LIST OF ABBREVIATIONS

ACh Acetylcholine

AMD Average Minimum Difference

DC Direct Current

EEG Electroencephologram

HH Hodgkin-Huxley

I_C Critical Current

I_M the Muscarinic Current

ISI Inter-Spike Interval

LFP Local Field Potential

LTD Long-Term Depression

LTP Long-Term Potentiation

MPC Mean Phase Coherence

NE Norepinepherine

NREM Non-REM

PRC Phase Response Curve

REM Rapid Eye Movement

SFA Spike-Frequency Adaptation

STDP Spike Timing-Dependent Plasticity

SWS Slow Wave Sleep

ABSTRACT

Acetylcholine (ACh) release is a prominent neurochemical marker of arousal state within the brain. Changes in ACh are associated with changes in neural activity and information processing, though its exact role and the mechanisms through which it acts are unknown. Here I show that the dynamic changes in ACh levels that are associated with arousal state control informational processing functions of networks through its effects on the degree of Spike-Frequency Adaptation (SFA), an activity dependent decrease in excitability, synchronizability, and neuronal resonance displayed by single cells. Using numerical modeling I develop mechanistic explanations for how control of these properties shift network activity from a stable high frequency spiking pattern to a traveling wave of activity. This transition mimics the change in brain dynamics seen between high ACh states, such as waking and Rapid Eye Movement (REM) sleep, and low ACh states such as Non-REM (NREM) sleep. A corresponding, and related, transition in network level memory recall is also occurs as ACh modulates neuronal SFA. When ACh is at its highest levels (waking) all memories are stably recalled, as ACh is decreased (REM) in the model weakly encoded memories destabilize while strong memories remain stable. In levels of ACh that match Slow Wave Sleep (SWS), no encoded memories are stably recalled. This results from a competition between SFA and excitatory input strength and provides a mechanism for neural networks to control the representation of underlying synaptic information. Finally I show that during the low ACh conditions, oscillatory conditions allow for external inputs to be properly stored in and recalled from synaptic

weights. Taken together this work demonstrates that dynamic neuromodulation is critical for the regulation of information processing tasks in neural networks. These results suggest that ACh is capable of switching networks between two distinct information processing modes. Rate coding of information is facilitated during high ACh conditions and phase coding of information is facilitated during low ACh conditions. Finally I propose that ACh levels control whether a network is in one of three functional states: (High ACh; Active waking) optimized for encoding of new information or the stable representation of relevant memories, (Mid ACh; resting state or REM) optimized for encoding connections between currently stored memories or searching the catalog of stored memories, and (Low ACh; NREM) optimized for renormalization of synaptic strength and memory consolidation. This work provides a mechanistic insight into the role of dynamic changes in ACh levels for the encoding, consolidation, and maintenance of memories within the brain.

CHAPTER I

Introduction

Nervous systems are adapted to integrate sensory information in order to generate meaningful behavior which enhances the fitness of organisms. By far the most common basis for neural information processing is the action potential (or spike). In the large networks which comprise the brains of vertebrates, input patterns from external sources generate spatiotemporal patterns of spiking activity through complex interactions between the biophysical properties of neurons and the connections between them. Over the course of time brain networks need to accurately represent the external world, store representations within synaptic connections, and recall stored representations as memories. Switching between these information processing modes require that networks be dynamically plastic on relatively stable network structures. The purpose of this work is to highlight the role of neuromodulatory neurotransmitters in regulating and switching between information processing modes at the network level.

1.1 The action potential and information representation between neurons

Neurons operate as dynamic units through the interaction of ionic currents crossing the neural membrane. Absent any external input neurons rest at a steady state

membrane potential, V_{rest}, which results from the balance of intrinsic currents entering and leaving the neuron. When a neuron receives depolarizing, or excitatory, input its membrane potential rises above V_{rest} opening voltage-gated sodium channels further depolarizing the neuron. If a neuron becomes sufficiently depolarized enough sodium channels will open to initiate a spike [1]. During a spike the inflow of sodium ions is followed by a delayed outflow of potassium ions which repolarizes the neuron. Generally, currents of positive charge into a neuron are referred to as depolarizing (increasing membrane potential, V_m) and while currents of positive charge out of a neuron are referred to as hyperpolarizing (decreasing V_m).

The predominant form of information transfer between neurons is through chemical synapses which translate an action potential in a presynaptic neuron to either depolarizing (excitatory) or hyperpolarizing (inhibitory) currents in the postsynaptic cell. On the presynaptic side, an action potential initiates the release of neurotransmitter (glutamate in the case of excitatory neurons or GABA in the case of inhibitory neurons) into the space between the neurons, the synaptic cleft. The neurotransmitter then binds to receptors which are selective to the neurotransmitter. In most cases these receptors are ligand-gated ion channels which allow cations (excitatory) or anions (inhibitory) to flow with the concentration and potential gradients across the cell membrane into the cell.

The more depolarizing input a neuron receives in a given time bin the more spikes it will fire in that time. This provides for representation of information by the rates neurons fire [2]. In this coding modality patterns of input intensity across a network of neurons is reflected in neural firing rates. Rate coding is widely represented in the brain and is commonly associated with sensory circuits like the visual system [3, 4]. There are limitations to the efficacy of rate coding, such as its limited capacity of

pattern separation [5] and that it fails to fully explain the activity in sensory areas of the cerebral cortex [6].

Aside from simply comparing the firing rates of neurons, information can be represented by the relative timing between neurons, or phase coding [7, 8, 9, 10]. Phase coding is often defined in the context oscillatory network activity. Oscillatory activity in neural circuits is frequently measured through the frequency content of the Local Field Potential (LFP) which is generated by coherent postsynaptic currents aligned in space. An example of phase coding is the theta-phase precession observed in the hippocampus [11]. In this system, information about an animal's location in space is represented in the time of firing with respect to a 4-8 Hz (theta band) oscillation.

1.2 Acetylcholine neuromodulation and how to model it

Rather than directly depolarizing or hyperpolarizing neurons to evoke or suppress spiking like glutamate or GABA, neuromodulators are neurotransmitters that alter neuronal firing by altering the biophysical properties of target neurons. Neuromodulators act through second messenger systems to turn off, turn on, or modify voltage gated ion channels in postsynaptic neurons. This mechanism of action occurs on a longer time scale than the fast neurotransmission mediated through glutamate and GABA, but can have profound effects of the firing rate and quality of firing in the target neurons.

1.2.1 Cholinergic modulation

Acetylcholine (ACh) is an important regulator of neural excitability that is essential for brain processes ranging from sleep to cue detection [12, 13]. Of its various effects, ACh modulates the excitability of neurons by its interaction with the

muscarinic receptor system, which activates a G-protein signaling cascade [14]. Important downstream targets of these signals are slow non-inactivating potassium channels. These channels, and their corresponding ionic current, the Muscarinic Current (I_M), are blocked when ACh is high and and this blockade is responsible for a switch between integrator and resonator excitability types [15].

ACh modulation of I_M exerts continuous control of neuronal excitability properties. On the poles of this range are two predominant excitability types: Type 1 (integrators) or Type 2 (resonators). These two excitability types differ in the dynamical mechanism of spike generation. A detailed mathematical analysis can be found [16], but in short Type 2 neurons have increased competition between depolarizing and hyperpolarizing currents which must be overcome to initiate a spike, while Type 1 neurons do not. This leads to several differences in characteristics between the two types, most notably Type 1 neurons initiate firing through a saddle-node on the limit cycle bifurcation while Type 2 neurons initiate firing through a Hopf bifurcation [17, 18].

The two characteristics that undergo the most dramatic change with the excitability type are the frequency response to an injected constant current and the Phase Response Curve (PRC) [19]. In terms of spike frequency response to an injected current curve (or a gain function) [20], both types have a Critical Current (I_C) below which no spiking occurs, but are quite different in terms of spiking response around this point. Type 1 neurons will fire at arbitrarily small frequencies as the critical value of I_C is reached leading to a continuous curve, whereas Type 2 neurons have a discontinuous frequency increase from quiescence and initiate firing at a higher frequency (Fig 1A). Another critical feature difference between Type 1 and Type 2 neurons is that Type 2 neurons vary their firing rate much less in response to changes

in injected current, or have reduced gain [20]. The difference in gain between these neuron types leads to larger differences in firing rates between cells receiving different inputs in Type 1 networks compared to Type 2 networks.

A concurrent change in excitability that occurs with activating the ion channels associated with I_M is differential response to brief and weak stimuli in terms of spike timing perturbation (i.e. advance or delay). This cellular property is quantified by the PRC [19]. The PRC is measured, both experimentally and numerically, by driving a neuron to fire at a stable periodic frequency and delivering small, brief, and depolarizing perturbations between its spikes, at different timings (phases) within the spiking cycle. In response to these perturbations the timing of the following spike will be earlier, later, or the same as an unperturbed period (Fig 1.1D&E). Type 1 and Type 2 neurons display significant differences in PRC shape. A Type 1 PRC is uniformly positive, meaning that perturbations will always advance the timing of the next spike. Type 2 neurons have a biphasic PRC, meaning that when a perturbation arrives determines if it will either advance or delay the next spike. The biphasic character of the Type 2 PRC allows these neurons to synchronize spike firing due to the ability to either shorten or elongate the period, with synchrony becoming a stable fixed point of the dynamics.

In addition to controlling membrane excitability type of a neuron, the changes in I_M also regulate SFA [21]. SFA effectively represents a negative feedback on neuronal firing and is frequently due to a hyperpolarizing current that builds up as a neuron fires action potentials. Here, I_M acts as an adaptation current and its blockade causes a significant reduction in SFA (Fig 1.1B&C). The effects of SFA and gain modulation are related by the fact the neuronal gain shows the firing rate of a neuron when I_M has saturated. Here we refer to SFA as the short-time scale effect of reducing the

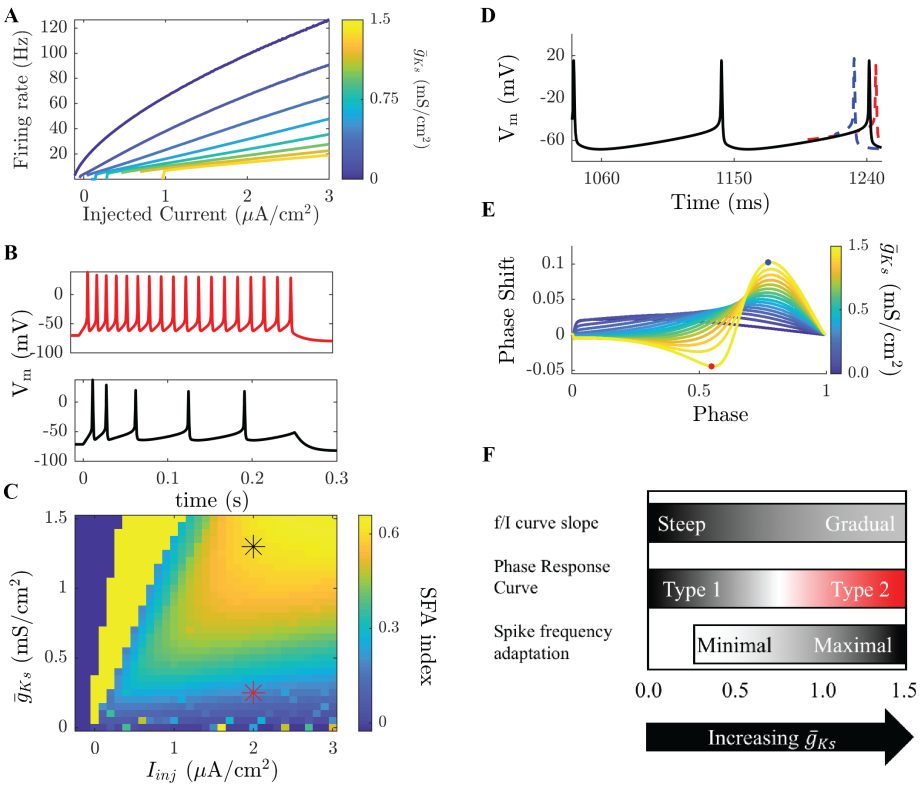

Figure 1.1: **Modulation of neuronal properties in a model of cholinergic modulation.** (A) The f/I curve increases its slope as ACh increases ($\bar{g}_{Ks}$ decreases). Blue colors represent the high ACh case. The onset of spike frequency adaptation in the Ks model occurs at a high $\bar{g}_{Ks}$. SFA is quantified here by the SFA index, which compares the inter-spike interval between the first two and the last two spikes in an induced burst. (B top) When gKs is low SFA is minimal and ISIs are equivalent throughout the burst. (B bottom) When $\bar{g}_{Ks}$ is high ISIs gradually increase though out the burst. (C) Measured SFA indices for various $\bar{g}_{Ks}$ and injected current values show that SFA is only significantly reducing frequency during the burst above $\bar{g}_{Ks} = 0.25$ mS/cm2, below this the effects are negligible. Stars indicate the parameters of the voltage traces shown in B. Dark blue squares indicate parameters that do not elicit spikes and bright yellow squares parameters that yield less than 3 spikes. (D) The PRC is measured by comparing perturbed versus unperturbed periods when neurons fire at a fixed frequency. When the next spike is earlier the phase response is positive (blue), when it is delayed it is negative (red). (E) Type 1 neurons have a strictly positive PRC (gray) while Type 2 neurons have a biphasic PRC. (F) Transitions in biophysical properties in the Ks model occur over different ranges of $\bar{g}_{Ks}$. Modulation of the f/I slope occurs continuously over the range of $\bar{g}_{Ks}$. The slope is steep for low $\bar{g}_{Ks}$ and gradual for high $\bar{g}_{Ks}$. The transition between a Type 1 and a Type 2 PRC occurs for high $\bar{g}_{Ks}$, though the PRC shape does change in a continuous manner as $\bar{g}_{Ks}$ changes. SFA has little effect for low $\bar{g}_{Ks}$ and only significantly effects the frequency of neurons for high $\bar{g}_{Ks}$.

frequency of a neuron as it fires, possibly terminating a burst of firing.

1.2.2 Conductance based neuron models and the slow potassium current

To investigate the effect of cholinergic modulation on the patterning of neural spiking across space and time it is useful to employ numerical modeling of networks of neurons. This method allows for tracking of every neuron in a network and fully recording the internal variables of neurons and interactions between them. Since much of how neurons act as dynamic unit is through the effects of voltage-gated conductances biophysical models seek to recreate these explictitly. This was pioneered using the Hodgkin-Huxley (HH) model [1], which has the following equation for currents passing through the membrane:

$$c_m \frac{dV_i}{dt} = -\bar{g}_{Na} m^3(V) h(V)(V - E_{Na}) - \bar{g}_K n^4(V)(V - E_K) - \bar{g}_L(V - E_L) + I_{syn_i} + I_{ext_i}, \tag{1.1}$$

where $m(V)$ and $n(V)$ reflect the fraction of sodium and potassium channels open, while $\bar{g}_{Na}$ and $\bar{g}_K$ are the conductances for these ions when all channels are open respectively. $h(V)$ reflects the fraction of sodium channels that are inactivated, which occurs near the peak voltage of the spike. E_{Na} and E_K are reversal potentials for the respective ions and determine whether current flow into or out of the neuron. Along with voltage dependent currents, $\bar{g}_L$ and E_L is a catchall for any currents that do not change conductance based on the membrane potential. I_{syn} is the summed effect of postsynaptic currents from all inputs the neuron receives and I_{ext} is any other currents injected to the neuron during the simulation. Numerically solving the current balance equation, as well as the equations for $m(V)$, $h(V)$, and $n(V)$, allows the for recreation of the voltage dynamics of a neuron for various input conditions, including fully reproducing the shape of a spike.

One useful feature of the conductance based neuron model is that ionic currents

and conductances can be directly measured in neurons and used to adapt the equations and parameters of the model to recreate various neuronal types and conditions. For the case of ACh this was done by adding a slow potassium conductance modeled after I_m as well as fitting the sodium and potassium voltage gated conductances to recreate the spiking properties of a cortical pyramidal neuron [22]. The resulting current balance equation is :

$$c_m \frac{dV_i}{dt} = -\bar{g}_{Na} m_\infty^3(V) h(V)(V - E_{Na}) - \bar{g}_{Kdir} n^4(V)(V - E_K) \\ -\bar{g}_{Ks} s(V)(V - E_K) - \bar{g}_L(V - EL) - I_{syn_i} - I_{ext_i}. \tag{1.2}$$

The most important difference between this model and the HH model is the addition of $s(V)$ and its associated maximal conductance $\bar{g}_{Ks}$, hence this model will be referred to as the Ks model. Since the main neuromodulatory effect of ACh, when acting on the muscarinic receptor, is a reduction of I_M the level of ACh release in a neural network is controlled as a model parameter by changing $\bar{g}_{Ks}$. When ACh is high, $\bar{g}_{Ks}$ is low and rises as ACh is decreased. For the data presented here $\bar{g}_{Ks}$ ranges between 0 and 1.5 mS/cm^2. Within this range the range of excitability properties targeted by ACh can be fully recreated as shown in Figure 1.1.

1.3 ACh shapes network activity: Type 1 versus Type 2 dynamics

In a network, the I_M mediated switch between Type 1 to Type 2 excitability together with effects of SFA have a profound influence on resulting network dynamics. Numerical investigations have shown how transitioning neurons from Type 1 to Type 2 excitability impact the patterns of neural activity in networks with different connection topologies. Much of this modeling work has used the Ks neuron model of cholinergic modulation [22].

As opposed to detailed recreation of specific biological neural circuits, this previous

work instead turned to the tools of network theory to allow us to create a range of networks that have the same quantifiable features of neural circuits by varying a small set of parameters by using the Watts-Strogatz small world network model [23]. Small world networks are defined as networks that maximize physical clustering (the probability that cells connected to a common neuron are also connected to each other) while minimizing the mean path length (the average number of connections between each pair of neurons in the network). Many studies of neural functional and structural connectivity have shown experimental similarity to the features of small world networks [24]. In these network models, neurons are arrayed on a ring lattice and the varied network parameters are the radius of connectivity (r; the distance across the lattice each neuron sends local outputs to) and the rewiring probability (P; the probability that a local output is exchanged for an output to a random target). The resulting networks have: 1) all local connections, 2) mostly local with a few random, long range connections, or 3) completely random connectivity depending on the value of P.

When ACh is high, neurons in the network are Type 1, and the f/I curve is continuous with a steep slope variance in the effects of synaptic input currents between neurons. This will result in a wider distribution of firing rates across the network. The features of this firing rate distribution are reflective of how the circuit connectivity structure interacts with a specific pattern of inputs from outside the network and is stable through time, due to the decreased SFA in high ACh conditions. During low ACh conditions, when Type 2 excitability dominates, variations in input across the network create less variance in firing rate in neurons. As the firing rate is more uniform, oscillatory firing paired with the increased synchronizability demonstrated by the shape of the PRC leads to synchronized bursting, with variations in input being

now reflected by relative phases of interacting neurons, rather than their frequency variations. Through the changes in neural excitability controlled by I_M, circuits can be shifted between these two, distinct functional regimes.

When networks of Type 1 excitatory neurons (without any inhibitory neurons) are coupled, the circuit structure, as defined by r and P, create a diversity of spike firing patterns [25]. In Type 1 excitatory networks, only networks with high connectivity radii and random structure support synchronous bursting. Networks composed of Type 2 neurons, on the other hand, are much less dependent on the interaction between r and P in the formation of bursting dynamics. As long as r is greater than 2%, networks generate highly synchronized bursting dynamics. Varying synaptic weights and neuron depolarization has a similar effect, Type 1 networks are more variable while Type 2 networks are generally synchronous [26]. Hence, modulation of the f/I curve plays an important role in shifting between network and cellular mechanisms of pattern formation. When gain is high (the f/I curve is steep) variations in synaptic input will drastically modify the firing rate of a neuron and interrupt internal mechanisms for synchronous firing among cells, while a shallow f/I merely causes slight shifts in an internal driven period. Also an important distinction between Type 1 and Type 2 neurons that applies to these results, is the integrator versus resonator mode of activity [15, 19].

The distribution of mAChRs has been shown to vary across cortical layers, cell types, and brain regions [27]. In addition to variations in ACh sensitivity, heterogeneities in neuronal morphology and ion channel expression can lead to networks of mixed populations of Type 1 and Type 2 neurons. Early on we have shown that injection of few Type 2 neurons into a Type 1 network can lead to synchrony [25]. In excitatory networks containing a 50/50 mix of Type 1 and Type 2 cells, removal

of synapses connecting the populations drastically affects the nature of bursting dynamics [28]. The ability of Type 2 neurons to synchronize a mixed population is also seen when these cells are network hubs (i.e. cells that have a high number of random, not local outputs). In such networks, synchrony during bursting is greatly increased and more robust to changes in the distributions of P used to generate a network structure than in Type 1 networks [29].

ACh release plays a central role in learning and memory [30]. Most of the work to date has focused on how ACh shapes circuit oscillations and in gating synaptic plasticity. To understand how the spiking dynamics that are associated with Type 1 and Type 2 excitability interact with fixed synaptic plasticity rules to modulate synaptic strengths within networks, we added spike timing-dependent plasticity to the Ks network model [31]. The general result of this work is that Type 1 network dynamics will potentiate synapses leading to a unimodal distribution of synaptic weights skewed toward saturation. Type 2 networks, due to the synchronized bursting dynamics that are characteristic of these networks, generate bimodal synaptic weight distributions where synapses are either silenced or saturated.

Both the PRC and frequency gain as a function of the input current describe how neurons change their dynamics of spiking in response to synaptic input. Our previous work extensively studied how these cellular changes affected network wide spatio-temporal pattern formation. Now, we are further proposing that these changes in spiking patterns may underlie even more profound changes in the network. We argue that biophysical features controlled by I_M activation are responsible for how network firing patterns interact with external input and characteristics of the physical structure of the network. This, in turn, leads to a dramatic switch in the coding strategy within the same network.

1.4 Network models

Much of the data presented here (Chapters II & III) employs another network connectivity scheme often encountered in the brain [32] and having strong dependence on Type 1 and Type 2 cellular dynamics, the lateral inhibition network. This network employs two lattices, one for excitatory neurons and one for inhibitory neurons. Lateral inhibition requires that inhibitory neurons send their outputs farther than excitatory neurons do. Here, I take the extreme of this condition and have globally connected inhibitory neurons and locally connected excitatory neurons. This connectivity scheme yields a spatially localized bump of firing that sustains itself through recurrent excitation between active excitatory cells, while the inhibitory cells in the bump are inhibiting the network equally. The competition between local excitation and global inhibition is at the center of how firing patterns in this network emerge. This network model is based on connectivity features in many cortical areas and is commonly used to model working memory [32, 33].

The lateral inhibition (or mexican hat) model diverges from the Watts-Strogatz in two primary ways: 1) the spatial extent of excitation and inhibition are different and 2) the connectivity is regular without any variation between neurons. This model was chosen because it provides a clear advantage when considering information representation, the center of the bump can be a read out of information. Stimulating an arbitrary location on the lattice will pin the bump to that location providing a clear indication of external input to the network. However, the results from this model are quite robust to varying network structure and will be shown in the following chapters.

1.5 Outline

In this dissertation, the aim is to provide a mechanistic understanding for how ACh controls spatiotemporal spike pattern formation and information processing in cortical networks. Much of this work builds upon previous modeling work using the Ks model [26, 31, 28, 29]. The first two chapters focus on how changes in the level of ACh expressed in a network control transitions in firing dynamics and memory recall. The last chapter will focus on the low ACh state and how neuronal properties in this state facilitate information storage and provide for the transduction between rate coded information and phase coded information.

In Chapter II the Ks model is used to detail how the balance between excitatory and inhibitory input, combined with cholinergic control of SFA shape spatiotemporal dynamics in the lateral inhibition network structure. I show that during high ACh conditions low SFA leads to a stationary bump of activity that drifts slowly across the network space. The size of this bump (i.e. the number of neurons that are active in the pattern) is governed by the strength of inhibition. Reducing the modeled level of ACh leads to the bump traveling across the lattice in a periodic manner by controlling how long a neuron can spike before adaptation silences it. Finally, because the length of a firing burst is the result of competition between excitatory (depolarizing) input and the hyperpolarizing I_m, enhancing recurrent excitation is a subregion of the network will act as a spatial attractor for the bump of activity. This work was published in PLoS Computational Biology [34].

The role of attractors formed by regions of recurrent excitation is expanded upon in Chapter III. Here I show that SFA, through its competition with excitatory input, allows for selective control of memory recall in neural networks. Using the

Ks model and a simpler Hopfield network I demonstrate that when a memory (a prefered bump location or pattern of firing across the network) is stored with stronger synaptic weights a stronger adaptation current is needed to move the network out of that memory. This work shows that the high ACh state is suited for the recall of memories that most closely match the input to a network, even if they are stored very weakly. Moderate reductions in ACh will destabilize weak memories and lead to the expression of stronger ones. Finally minimal levels of ACh, like during Non-REM (NREM), lead to SFA so strong that stable recall of any memory is impossible. This work was published in Physical Review E [35].

Lastly, in Chapter IV the role of neuronal resonance, which is characteristic of cortical neurons in low ACh conditions, provides for an input dependent organization of network spiking around a common oscillatory input. I show that when networks are presented a pattern of external current inputs and brought in resonance with an oscillation neurons with higher inputs will fire spikes at earlier phases of the oscillation. This input dependent patterning paired with learning through synaptic plasticity allows for the faithful storage of inputs into the synaptic weights of the network. Additionally, this model reproduces many features of theta phase precession and replay in the hippocampal place cell system. This work was published in the Proceeding of the National Academy of Science [36].

CHAPTER II

Formation and dynamics of waves in a cortical model of cholinergic modulation

Here I introduce a model of cholinergic modulation in cortical networks and describe the role of acetylcholine in the spatiotemporal patterning of spiking activity in these networks. This chapter was published in PLoS Computational Biology in 2015 (Vol. 11, Pg. e1004449).

2.1 Abstract

Acetylcholine (ACh) is a regulator of neural excitability and one of the neurochemical substrates of sleep. Amongst the cellular effects induced by cholinergic modulation are a reduction in Spike-Frequency Adaptation (SFA) and a shift in the Phase Response Curve (PRC). I demonstrate in a biophysical model how changes in neural excitability and network structure interact to create three distinct functional regimes: localized asynchronous, traveling asynchronous, and traveling synchronous. These results qualitatively match those observed experimentally. Cortical activity during Slow Wave Sleep (SWS) differs from that during Rapid Eye Movement (REM) sleep or waking states. During SWS there are traveling patterns of activity in the cortex; in other states stationary patterns occur. The model is a network composed of Hodgkin-Huxley type neurons with the Muscarinic Current (I_M) regulated by

ACh. Regulation of ACh level can account for dynamical changes between functional regimes. Reduction of the magnitude of this current recreates the reduction in SFA the shift from a Type 2 to a Type 1 PRC observed in the presence of ACh. When SFA is minimal (in waking or REM sleep state, high ACh) patterns of activity are localized and easily pinned by network inhomogeneities. When SFA is present (decreasing ACh), traveling waves of activity naturally arise. A further decrease in ACh leads to a high degree of synchrony within traveling waves. We also show that the level of ACh determines how sensitive network activity is to synaptic heterogeneity. These regimes may have a profound functional significance as stationary patterns may play a role in the proper encoding of external input as memory and traveling waves could lead to synaptic regularization, giving unique insights into the role and significance of ACh in determining patterns of cortical activity and functional differences arising from the patterns.

2.2 Introduction

The difference between cortical activity patterns during waking, REM, and SWS is striking. During waking and REM sleep low amplitude, high frequency Electroencephologram (EEG) and Local Field Potential (LFP) recordings suggest that cortical population dynamics are localized. Conversely, in SWS, the dynamics enter a slow ($\sim$ 1 Hz) oscillation state where individual neurons oscillate between a high frequency (up) state and periods of quiescence (down state) [37, 38]. The functional role of high frequency local activation (i.e. waking or REM state) has been linked to attention and working memory [39, 40, 41], while traits of SWS have been related to synaptic homeostasis and sleep pressure [42, 43, 44, 38]. Both of these dynamic patterns can be thought of as upstates, but with differing lengths.

ACh is a neurotransmitter that governs the cortical dynamics associated with arousal and sleep state. Levels of ACh rise during the transition from Non-REM (NREM) sleep to waking or REM sleep. ACh acts through two pathways, the nicotinic receptor and the muscarinic receptor. The nicotinic receptor directly depolarizes cells while the muscarinic suppresses voltage-gated potassium channels. Inactivation of these channels, and the current associated with them (the I_M), changes the intrinsic excitability of neurons. Experiments have shown that ACh modulates neural excitability in two ways: (1) ACh reduces SFA mediated by the I_M and increases the slope of the neural spike frequency-current (f-I) curve [45, 20], and (2) it induces changes in the synchronization properties of neurons via the PRC [19, 26]. ACh induces a shift from a biphasic type 2 PRC to monophasic type 1 PRC (Fig 2.1C). It has been previously shown that networks of type 1 neurons are asynchronous while those of type 2 neurons are highly synchronous [26].

The aim of this paper is to elucidate how cholinergic modulation interacts with network connectivity structure to form various patterns of network activation obtained experimentally. To do so I use simulations of a conductance-based (Hodgkin-Huxley) cortical network model including cholinergic modulation [22] and a mexican hat type of connectivity scheme that was experimentally observed in various cortical areas [46, 47] .

We demonstrate how regulation of SFA in conjunction with the balance between excitation and inhibition leads to various network dynamics. We show that ACh driven reduction of SFA in model networks with lateral inhibition is responsible for the transition from moving to stationary dynamics and E/I balance is responsible for switching between highly local and global dynamics. We then study the properties of the two states and their transition. Functionally, the high ACh state is far more

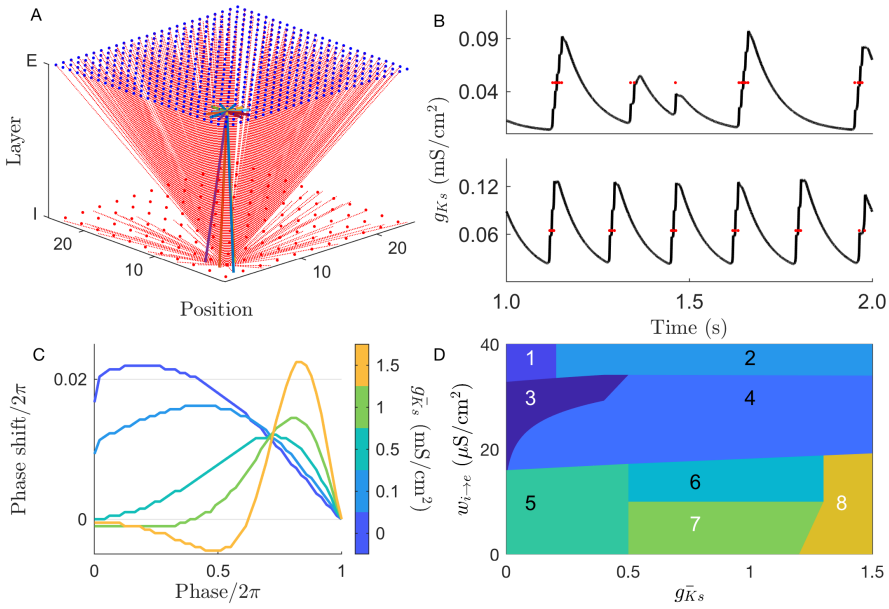

Figure 2.1: **Cortical network model of cholinergic modulation**. (*A.*) The network model consists of a square lattice split into an excitatory and an inhibitory layer. A connectivity scheme balancing short-range excitation and global inhibition was used to mimic the lateral inhibition motif seen in many areas of the cerebral cortex. (*B.*) Examples of SFA induced by the slow potassium conductance are shown for $g_{\bar{K}s} = 0.75$ mS/cm^2 (top) and $g_{\bar{K}s} = 1.5$ mS/cm^2 (bottom). The red dots indicate the spike times of the neuron in question and illustrate the the offset of an upstate corresponds to the maximal level of $g_{\bar{K}s}$. (*C.*) The phase response curve of individual neurons shifts from type 1 to type 2 as $g_{\bar{K}s}$ increases. (*D.*) An illustration of the dynamics sampled by scanning inhibitory strength,$(w_{i\to e})$, and $g_{\bar{K}s}$. In a general sense, the spatial scope of activity is determined by the excitatory/ inhibitory balance and the temporal scope of activity is determined by the strength of SFA. Key: (1) quiescent (2) mixed dynamics, (3) stationary bump (4) traveling bump (5) global high frequency activity (6) multiple interacting bumps (7) planar wave (8) global burst.

sensitive to heterogeneities in network structure than the traveling wave state. In this neuron model, SFA and PRC effects occur over different ranges of ACh, which leads to three distinct functional regimes. Further, I show that both SFA and E/I balance shape network activity by setting the spatial (E/I balance) and temporal (SFA) extent of network upstates.

2.3 Models

2.3.1 Neuron model

I use a conductance-based model of cholinergic modulation in pyramidal cells using Hodgkin-Huxley type gating dynamics for active conductances [22]. The membrane voltage dynamics are described by:

$$\begin{aligned} c_m \frac{dV}{dt} = &-m_\infty{}^3 h \bar{g_{Na}}(V - E_{Na}) - n^4(V)\bar{g_{K_{dir}}}(V - E_K) \\ &-s\bar{g_{Ks}}(V - E_K) - \bar{g}_l(V - E_l) + I^{tune} - I^{syn} \end{aligned} \tag{2.1}$$

The gating variables m, h, n, and s represent the sodium conductance, the effective blockage of sodium current and potassium conductances respectively. In the case of h, n, and s dynamics of the form:

$$dx/dt = \frac{(x_\infty(V)) - x}{\tau_x(V)}.$$

The function $x_\infty(V) = 1/(1+\exp((\alpha_x - V)/\beta_x)$ represents the steady state gating for each conductance and gating time constant, τ_x, is constant for s, $\tau_s = 75$, is governed by $\tau_x = 0.37 + D_x/(1 + \exp((\gamma_x + V)/\varepsilon_x))$ for h and n. The s variable corresponds to the slow potassium current which is ultimately responsible for the shift in neural excitability mediated by ACh. Adjusting the magnitude of this current (i.e. varying the parameter $\bar{g_{Ks}}$) changes neuronal excitability characterized by the level of SFA. For low $\bar{g_{Ks}}$ values neurons have a minimal level of SFA. As $\bar{g_{Ks}}$ increases the neurons display high levels of SFA.

The direct input current, I^{tune}, was adjusted so that all cells fired at 10 Hz in the absence of any synaptic input, independent of $\bar{g_{Ks}}$. The synaptic input to ith neuron is given by:

$$I_i^{syn} = \sum_{j=1}^{n} A_{i,j} w_{j\to i} K(e^{\frac{-(\tilde{t}-\tau_D)}{\tau_S}} - e^{\frac{-(\tilde{t}-\tau_D)}{\tau_F}})(V_i - E_{syn}), \tag{2.2}$$

where $A_{i,j}$ is the network adjacency matrix, $\tilde{t}_j$ is the time of the last spike of neuron j, τ_F and τ_S are synaptic time costants and τ_D is the synaptic delay. The parameter $w_{j\to i}$ is the synaptic coupling between neurons i and j based on the respective species of each. K is a normalization constant such that the range of each synaptic pulse is $\in [0, w_{j\to i}]$. Values of the neural parameters were adopted from [26] and are listed in 2.1. The equations were solved for 5 seconds at 0.05 ms time steps using the 4th order Runge-Kutta algorithm.

2.3.2 Network model and measurements of dynamics

I considered networks composed of 625 excitatory and 121 inhibitory neurons evenly distributed over a two-layer lattice of sides $L = 25$ (Fig 2.1A) with periodic boundaries. The fraction of inhibitory cells, 16%, was close to the 20% seen in the cortex [48] and the dynamics were robust to shifts in inhibitory fraction between 13% to 22% (Supplemental 2.6.4 to 2.6.4). To evenly distribute the inhibitory cells with respect to the excitatory layer the spacing of inhibitory cells , $Grain_i$, was 2.87 lattice units while excitatory cells were spaced $Grain_e$, at 1 unit. We used a center-surround (or lateral inhibition) type network scheme which balances short-range excitation and global inhibition. This is an established model for cortical connectivity [49]. All excitatory neurons were connected to all cells within a radius defined by:

$$R_{xx} = \sqrt{\frac{L^2 k_{xx}}{\pi N}} \tag{2.3}$$

where $k_{ee} = 16$ and $k_{ei} = 4$. This leads to 20 connections to excitatory and 4 to inhibitory nearest neighbors. Inhibitory neurons were globally connected. Unless

otherwise stated the maximum synaptic strengths were 20 μS/cm^2 for all synapses.

As seen (Fig 2.1D) the dynamics which result vary qualitatively depending on the values of the parameters introduced above. It includes cases where spiking is spatially confined ('stationary bump'), where the activity moves ('moving bump'), plane waves of activity, global bursting, etc. To illustrate the character of the dynamics on raster plots cells were sorted by a spatial coordinate given by $S_i = y_i + x_i/L$ where x_i and y_i are the coordinates of the cell in the lattice.

The speed of moving bumps of activity was calculated by dividing the simulation time into 10 ms bins in which the frequency of all excitatory cells were calculated. For each time bin the center of activity was calculated in a manner similar to a center-of-mass calculation using an algorithm previously described in [50], which accounts for the periodic boundaries of the network. The wave speed was averaged over the final 2.5 s of the simulation run. When averaging wave speed the following cases were excluded because they were not appropriate for the speed measure: where no excitatory cells were active, where more than 300 cells were active within any 10 ms time bin, where the standard deviation of active cells was greater than the mean number of active cells within 10 ms time bins, when more than one bump of activity was stable, or when the network was highly synchronized.

To measure synchronization we used the bursting measure:

$$B = \frac{1}{\sqrt{N}}\left(\frac{\sqrt{\langle \tau^2 \rangle - \langle \tau \rangle^2}}{\langle \tau \rangle} - 1\right) \tag{2.4}$$

where τ is the series of inter-spike intervals of all spikes regardless of cell identity and N is the total number of spikes [26]. This measure approaches 1 as network activity approaches perfect synchrony. We consider a network to be synchronized when $B > 0.7$ as this value bisects the bimodal distribution of B (Fig 2.7).

Heterogeneities were added to the network by multiplying the strength of excitatory to excitatory connections beginning and terminating within a 8 x 8 region of the network by a constant value ranging from 1.005 to 2.5 (i.e., increasing recurrent excitation between 0.5% to 150%). Neurons within the heterogeneity also received an additional 0.5 μA/cm^2 of direct current during the first 0.5 s of the simulation.

Preference for the heterogeneous region is described by the normalized measure $\phi = (f_{in} - f_{out})/(f_{in} + f_{out})$ where f_{in} and f_{out} are the average frequency of excitatory neurons inside and outside the heterogeneity respectively. ϕ ranges between 1, when the only activity is within the heterogeneity, and -1, when all network activity is outside. When measuring network preference for the synaptic heterogeneity ϕ was calculated for the last half of the simulation run.

2.4 Results

I used the above model to elucidate how ACh modulation together with the network connectivity properties regulates spatio-temporal dynamics in a system. The level of $g_{\bar{K}s}$ sets the amount of SFA in each neuron and shortens the length of an upstate both in time and in the number of spikes fired (Fig 2.1B). Sampling the parameter space defined by $g_{\bar{K}s}$ and $w_{i\to e}$ allows for multiple dynamical regimes to emerge. These range from complete quiescence for excitatory cells at one extreme to globalized network bursts at another (Fig 2.1D and Fig 2.7).

Simulations under a variety of network structures and network sizes yielded qualitatively similar results provided that the radius of inhibitory connections was larger than that of excitatory connections. Reducing R_{ie} from global to smaller values leads to multiple independent bumps. Note that these dynamics are different from the multiple interacting bumps described in Fig 2.1D. Implementing a heteroge-

neous network lattice where neurons are placed at irregular intervals, the degree distribution of neurons is nonuniform, and connections are rewired based on the Watts-Strogatz formalism [51] did not change the the results qualitatively. Removing periodic boundary conditions leads to traveling waves in a circular as opposed to periodic direction (2.6.4).

Moderate levels of inhibition ($w_{i\to e}$ = 20 μS/cm^2) generated two distinct classes of dynamics as the level of SFA was changed. When g_{Ks}^- levels are low (which corresponds to a high ACh state) network activity is localized to a restricted area with minimal drift, the stationary bump regime (Fig 2.2C top). Increasing g_{Ks}^- (or decreasing ACh) leads to a localized traveling wave of activation (a bump) that traverses the entire network space (Fig 2.2C bottom). Local dynamics are characterized by high frequency, asynchronous spiking. Spike dynamics in the global state are also asynchronous, but oscillate between a high frequency upstate and a low frequency down state. While the level of SFA in the system controls the amount of time that activity remains in any single location, the level of inhibition (E/I balance) defines the size of the portion of the network that is in an upstate at any given time. For low levels of inhibition ($w_{i\to e}$ = 10 μS/cm^2), depending on SFA level, either the whole network is active with quiescent regions emerging periodically (low levels of SFA; g_{Ks}^- = 0 mS/cm^2; Fig 2.2B top) or two distinct interacting bumps are stable (high levels of SFA; g_{Ks}^- = 1 mS/cm^2; Fig 2.2B bottom). High levels of inhibition ($w_{i\to e}$ = 30 μS/cm^2), however, reduce the spatial extent of activity at any given time (Fig 2.2D).

The interplay between SFA and inhibitory strength ($w_{i\to e}$) is shown in Fig 2.2A. The SFA level (i.e. the magnitude of g_{Ks}^-) is the primary factor in determining the transition between the localized and global activation state. For any given level

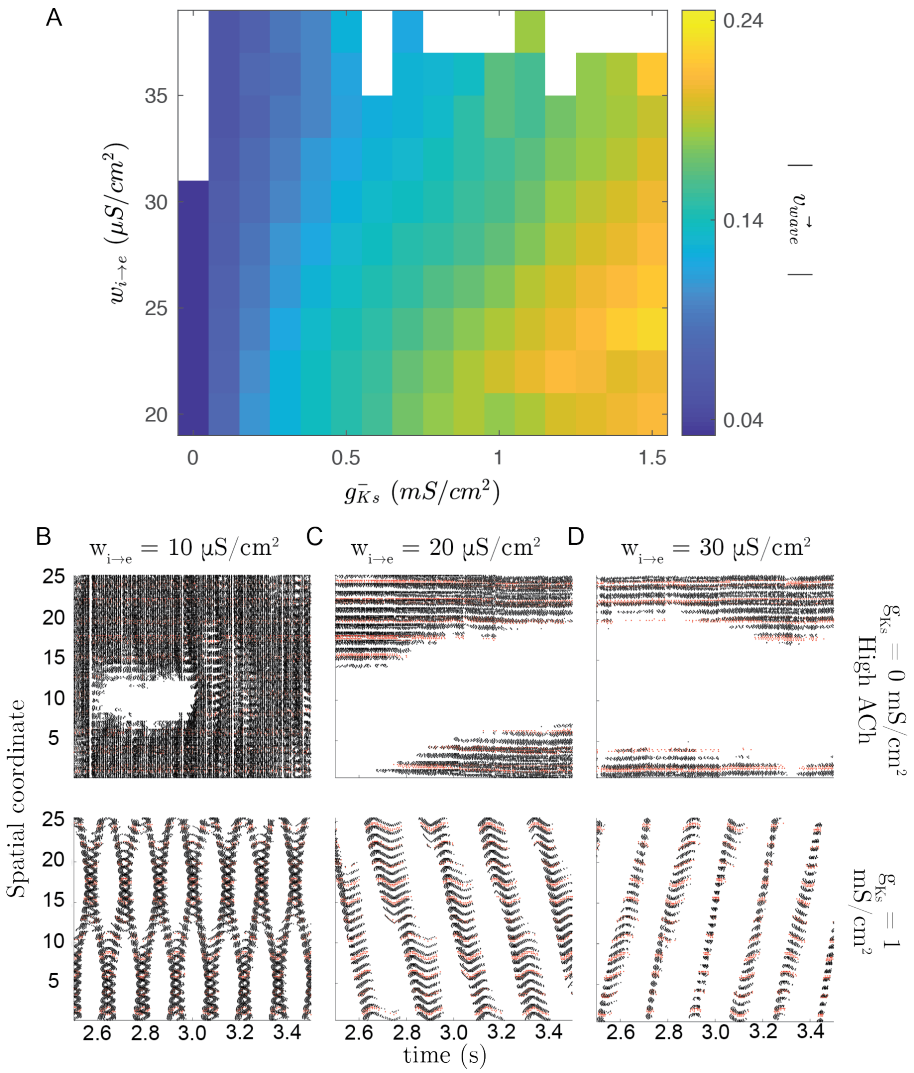

Figure 2.2: **Both E/I balance and SFA level affect the spatio-temporal properties of cortical activities**. (*A.*) Within the single bump the levels of $g_{\bar{K}s}$ and $w_{i\to e}$ determine the speed of propagation . However, SFA does have a much larger effect on wave speed than E/I balance. Panels B, C, and D show example raster plots for $w_{i\to e} = 10$, 20, and 30 μS/cm^2 respectively with $g_{\bar{K}s} = 0$ mS/cm^{2}on top and $g_{\bar{K}s} = 1$ mS/cm^2 on bottom. In each, black markers represent spikes from excitatory cells and red markers represent those from inhibitory cells. Cells are sorted by spatial coordinate, a measure described in the methods section.

of inhibition, the transition between stationary and traveling frequency dynamics occurs over a narrow range of $g_{\bar{K}s}$. The effect of inhibition becomes clearer in the traveling wave regime, where the speed of the wave propagation is slowed by increased inhibitory strength. For strong values of inhibition waves are arrested. The empty squares of Fig 2.2A indicate parameter values that yield networks where excitatory

cells are completely quiescent or involved in network-wide synchronous bursting.

From the single cell perspective, the level of SFA has the largest effect on the length of an upstate. Scanning g_{Ks}^{-} between 0.1 and 1.5 mS/cm^2 results in a reduction of the number of spikes per upstate. This reduction of spike number corresponds to an increase of both the length and variability of inter-spike intervals (Inter-Spike Interval (ISI)s) within an upstate (Fig 2.3A). Increasing inhibitory strength has a less dramatic effect on the length of an upstate. For a given value of g_{Ks}^{-} increasing inhibition reduces the average number of spikes per upstate in a linear fashion, independent of g_{Ks}^{-} (Fig 2.3B). While SFA level and E/I balance define the character of neuron upstates, PRC modulation regulates synchrony within the upstate independently (Fig 2.4). For g_{Ks}^{-} values large enough to yield traveling waves, but too low to shift the PRC to type 2 ($g_{Ks}^{-} = 0.1$ mS/cm^2 in the figure), spike synchrony between cells with overlapping upstates is low and comparable to levels of synchrony during stationary bump dynamics. In both these cases the ISI interval is approximately uniform $\in [-\pi, \pi]$ (Fig 2.4A; left panels). Increasing g_{Ks}^{-} to the point where the PRC shifts from type 1 to type 2 leads to high synchrony within the upstates as indicated by an increased observation of ISIs close to 0 or 2π and a corresponding decrease at $\pm\pi$ (Fig 2.4A; right panels).

It is known from other studies that in a stationary bump regime, dynamics can be pinned to a specific region by enhanced recurrent excitation [32, 52]. We used this effect to map the transition between local and global dynamics (Fig 2.5A). We defined ϕ (see methods section), as a proxy for the network tendency to localize the dynamics. Increasing g_{Ks}^{-} from zero rapidly decreases localization with a 50% decrease in ϕ occurring within a range of 0.25 mS/cm^2.

An important function of neural networks is the ability to recognize and respond

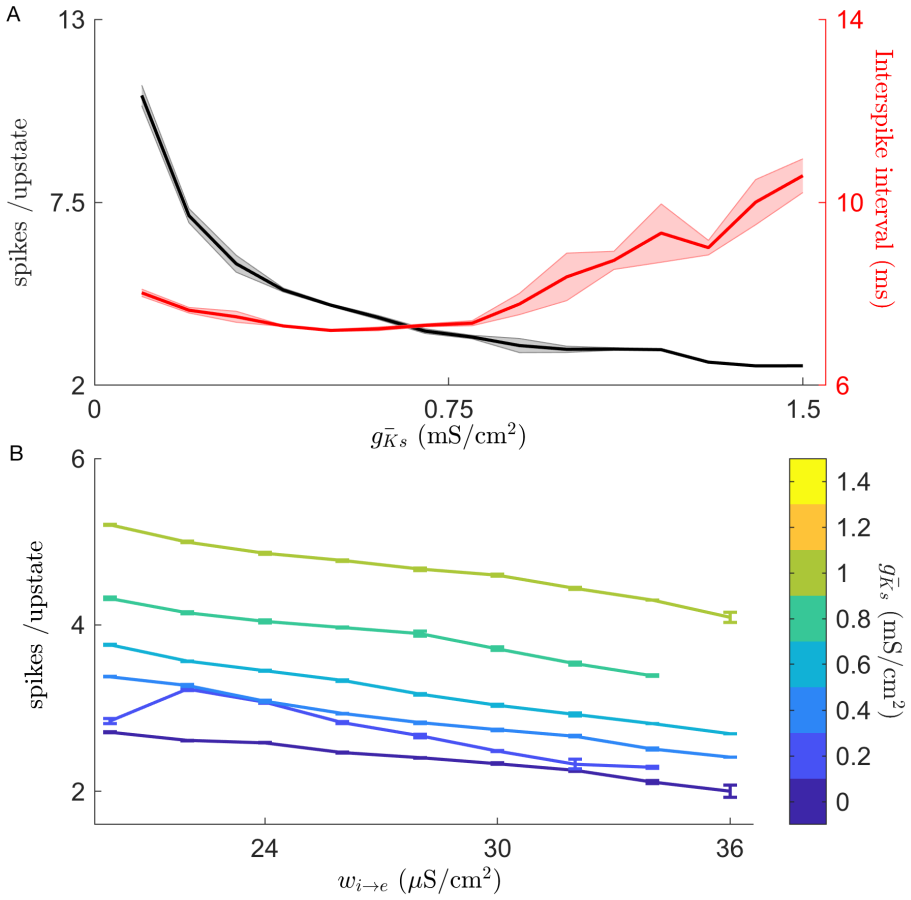

Figure 2.3: **Slow potassium conductance shapes upstate dynamics of individual neurons**. (*A.*) For very low levels of $g_{\bar{K}s}$ individual upstates of neurons last for a longer and more variable number of spikes (*black data series*). The adaptive effect of the slow potassium conductance is shown by the large variation in ISI for $g_{\bar{K}s}$ values above 0.75 (*Red data series*). Increasing $g_{\bar{K}s}$ reduced the number of spikes per upstate to about 3. Data is shown for $w_{ie} = 24\ \mu S/cm^2$ and error bars represent standard deviation. (*B.*) Increasing inhibitory strength, while decreasing wave speed maintains a stable number of spikes per upstate, with average number not changing by more than one (data are mean $\pm$ s.e.m).

to structural features such as information encoded in synaptic weights. To explore this idea, we compared how changes in the SFA level affect preferential activation of a region with enhanced recurrent excitation. This effect has been previously shown to localize stationary bump dynamics in spiking networks [32, 52]. Networks with low levels of SFA were highly sensitive to synaptic heterogeneity, with as little as a 5% increase in synaptic strength being sufficient to localized the activation to the

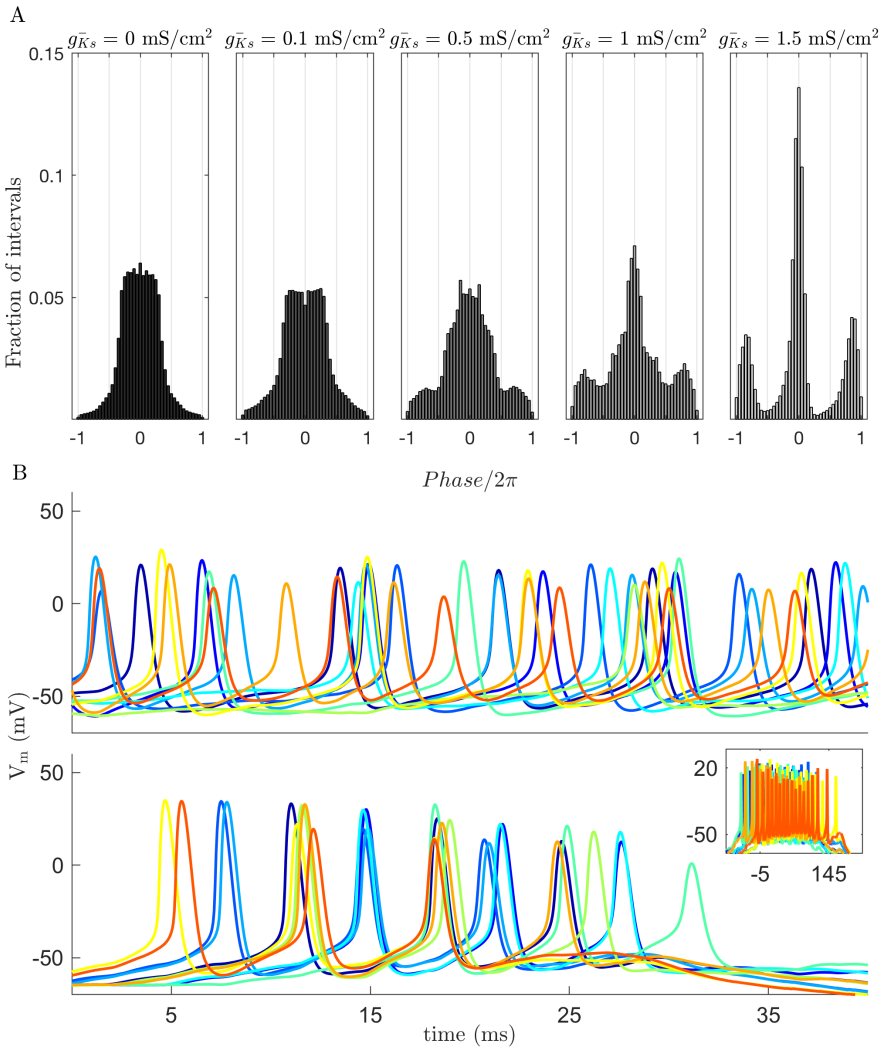

Figure 2.4: **Slow potassium current regulates synchrony through PRC modulation**. (*A.*) An increase in spike synchrony within upstates corresponds to the shift from a type 1 to type 2 PRC which occurs at high levels of $g_{\bar{K}s}$ as indicated by the distribution of inter-spike intervals. Time is shown as normalized phase based on the average period of firing during an upstate and the colors of the bar graphs corresponds to the PRCs shown in Fig 2.1. (*B.*) Characteristic voltage traces for 10 neighboring cells during an upstate for $g_{\bar{K}s}$ = 0.1 mS/cm^2 *top* and $g_{\bar{K}s}$ = 1.5 mS/cm^2 *bottom*. Each cell is represented by a different color. For both conditions are shown on a 40 ms time scale and the inset shows the entire upstate for the $g_{\bar{K}s}$ = 0.1 mS/cm^2. Data shown here is for $w_{i\to e}$ = 24 μS/cm^2.

heterogeneity (Fig 2.5B). Sensitivity to heterogeneity decreases as SFA increases as networks allow wave dynamics, but persists for strong heterogeneities well into the wave regime. For low levels of SFA this effect is driven by upstates lasting significantly longer within the heterogeneous area than outside (Fig 2.5C). This increase in

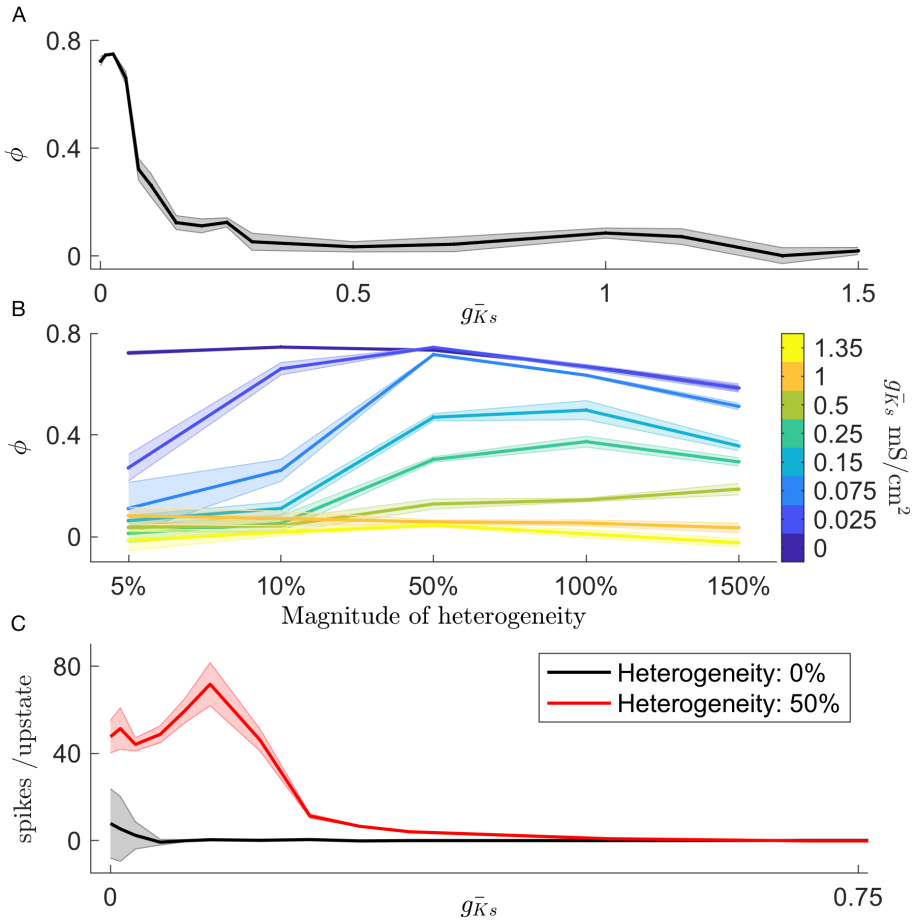

Figure 2.5: **Reducing slow potassium conductance increases network sensitivity to heterogeneities in synaptic coupling**. (*A.*) The transition from stationary to moving bump dynamics is demonstrated by ϕ, normalized preference for heterogeneity. Increasing $g_{\bar{K}s}$ rapidly reduces the preference for an area with a 10% increase in strength of recurrent excitatory connections. (*B.*) Significantly enhanced heterogeneities are able to act as an attractor of network activity even for networks with high levels of SFA with a significant preference apparent up to $g_{\bar{K}s} = 0.75$ mS/cm^2. (*C.*) Network preference manifests as longer upstates within the heterogeneous zone than outside it. (data are mean $\pm$ s.e.m).

upstate length falls off quickly, even for levels of $g_{\bar{K}s}$ where ϕ displays a preference. This difference stems from ϕ being calculated on a longer time scale.

2.5 Discussion

These results have shown that changes in SFA level and E/I balance drive the transitions from stationary to traveling (SFA) and local to global (E/I Balance) behavior. These states arise from an interaction between neural excitability and the

network-wide strength of lateral inhibition. The magnitude of SFA is a determining factor in whether or not network activity can be pinned by structural heterogeneities such as recurrent excitation. The results indicate that large scale spatio-temporal dynamics can be induced by ACh mediated SFA and that neural networks composed of highly excitable cells will be more responsive to synaptic heterogeneities. Additionally, ACh induced changes in SFA level and PRC shape occur over differing values of $g_{\bar{K}s}$.

In the model I used the changes induced by ACh resemble the dynamical cycles seen in the cortex during sleep. Experiments have shown that *in vivo* stimulation of cholinergic neurons can induce the transition from SWS to REM like sleep activity [53, 54]. The low ACh state in this model creates traveling waves of high frequency upstates and quiescent down states, reminiscent of what occurs during SWS. Analysis of EEG data in sleeping humans has identified the slow wave in SWS as a traveling wave originating in the frontal cortex and propagating to the posterior [55]. An interesting and relevant feature of the traveling slow wave is that the origins are stable within individuals. Traveling waves in the conductance based model are sensitive to strong heterogeneities for intermediate values of $g_{\bar{K}s}$. Experiments have shown that inducing local synaptic potential via transcranial magnetic stimulation can define the orgin of traveling slow waves [42, 43]. These results dovetail nicely with our mechanism of recurrent excitation and SFA modulation highlighting regions with strengthened synaptic connectivity.

This model replicates two cellular effects of cholinergic modulation; a reduction of SFA and the shift from a type 1 to a type 2 PRC. The network level consequences of these cellular effect occur over distinct ranges of $g_{\bar{K}s}$. Previous modeling studies have shown that networks composed of type 1 neural oscillators are generally asynchronous

while type 2 networks are highly synchronous [26]. Here I show that neurons with a type 2 PRC are able to synchronize over the short time scale of a single upstate (Fig 2.4). It is remarkable that type 2 neurons show much higher synchrony than type 1 cells which have much longer to entrain. Type 2 neural oscillators transfer information, measured through spike train correlation, on a much shorter time scale than type 1 oscillators which could explain the difference upstate synchrony [56]. It has been shown previously that network models that learn via spike timing dependent plasticity (SDTP) will strengthen synapses when composed of type 1 neurons, while weakening occurs when component neurons are of type 2 [31].

SWS is critical for memory consolidation, particularly during early stages [57, 58, 59]. The changes in both SFA level and in the PRC shape are both likely to play a role in the changes in synaptic strength during SWS, but whether they interact synergistically is unclear and will be the topic of further study. Another important implication of these results is to show how stationary versus traveling dynamics fit into the frameworks proposed by the synaptic homeostasis hypothesis (SHY) [60], which proposes synaptic renormalization during sleep, and the synaptic embossing hypothesis (SEH) [61], in which select circuits are strengthened by synchronous firing during REM in addition to renormalization during SWS. It may be that localized asynchronous activity during REM sleep can further strengthen regions specified by enhanced synaptic strength during waking, while traveling, but synchronous, activity within a globally traveling wave can cause global depotentiation of synapses. This would lead to a large increase in synaptic signal to noise ratio as proposed by SHY [60] while employing a REM dependent dynamical mechanism proposed by SEH [61]. Recent *in vitro* and *in silico* studies have demonstrated the importance of REM sleep on experience dependent plasticity [62, 63]. The differing g_{Ks}^{-} ranges for SFA induced

local to global and the PRC induced asynchronous to synchronous transitions may account for the importance of SWS to REM transitions in synaptic restructuring recently reported [63]. The interaction between ACh level and inhibitory strength in our model could be functionally significant. The administration of GABAergic drugs (which correspond to higher $w_{i\to e}$ values in out model) increases the time spent in SWS and the power in the delta ($\sim$ 1 Hz) range, but does not measurably increase memory consolidation [64]. This may be due to the interaction of the two aforementioned mechanisms, but also to the increased GABA levels changing features of the traveling waves during SWS. It would be interesting to see whether GABA agonists decrease the propagation speed of SWS waves in LFP measurements.

To demonstrate the extent that the spatial properties of upstates are set by E/I balance we sampled parameters that fall outside of normal physiological conditions and only values that fall within the reduced range that yield single bumps produce dynamics representative of sleeping or waking states. During SWS, increased activity of GABAergic projections from the basal forebrain increase both phasic and tonic inhibition within the cortex [65]. Pharmacologically enhancing phasic inhibition, which would skew E/I balance toward inhibition in our model, decreases power in the delta band [66]. Increasing inhibition caused a decrease in the average number of spikes per upstate and narrowed the spatial extent of an upstate, both of which would lead to a decrease in LFP power. On the other hand, increasing tonic inhibition leads to an increase of delta power [66]. This model does not include a representation of tonic inhibition and adding this feature would be a valuable extension of these results. During high ACh conditions a more complicated inhibition conditions exist. While state dependent GABA input from the basal forebrain is reduced, muscarinic agonists increase the amplitude and frequencies of spontaneous inhibitory postsy-

naptic currents [67]. This enhanced inhibition on its own would increase localization and sensitivity of stationary dynamics. Cholinergic drugs decrease the magnitude of evoked inhibitory input, however [68]. Whether or not these effects lead to a net E/I balance shift is not clear.

When the network is in the stationary state (when $g_{\bar{K}s}$ is low and SFA is minimal; the high ACh state) the excited region generates large levels of distal inhibition that reduces the likelihood that neurons outside this region will fire. Reducing the strength of inhibition causes a corresponding increase in the likelihood that far away cells will fire, eventually leading to a global high frequency state (Fig 2.1C). As SFA is increased (when $g_{\bar{K}s}$ is increased or ACh levels fall) the length of an individual neuron's upstate becomes limited. As excited cells enter a period of quiescence, neighboring neurons are able to enter an upstate due to a relaxation of distal inhibition. This relaxation increases the spatial extent of cells that are in an upstate at the same time. These two factors affect the character of spatio-temporal dynamics by effectively setting the two components of wave speed, dx/dt (Fig 2.6). The strength of inhibition sets dx, with lower levels increasing its magnitude (and thus total wave speed as well). A large amount of SFA shortens dt which drives large increases in wave speed. This notion also explains how synaptic heterogeneity (i.e. enhanced recurrent excitation) acts to pin activity. When the excited region passes over areas with increased excitatory coupling the recurrent excitation is able to reduce the effects of SFA on neurons causing an increase in dt when activity is within this area decreasing the propagation of excitation.

Stationary bump dynamics have long been used as a model of working memory [69, 70, 71]. In this model, the location of excitation preserves the location of a transient input and synaptic heterogeneities stabilize bump location [32, 52]. Recent

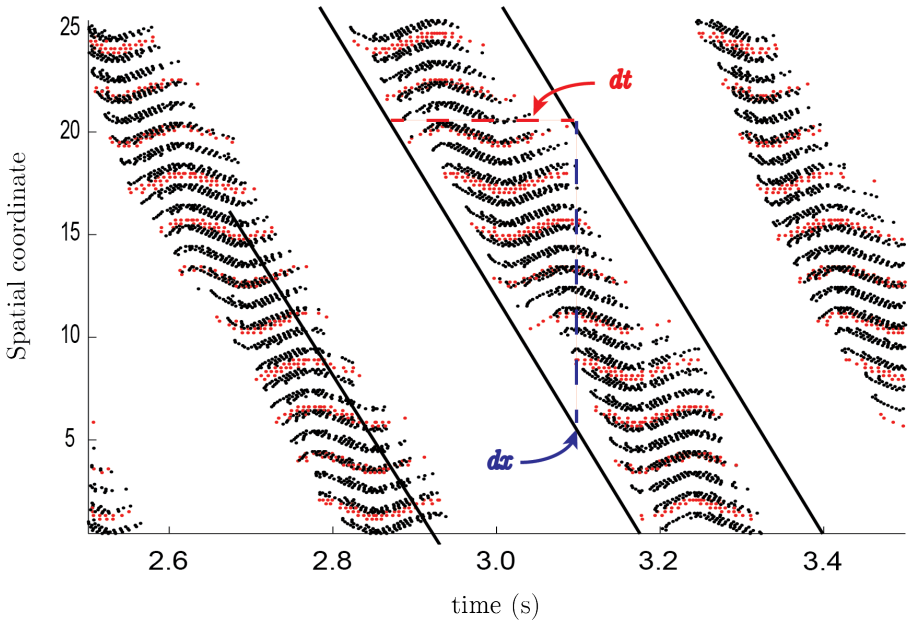

Figure 2.6: **Slow potassium conductance and E/I balance work in concert to shape upstate traveling bump dynamics**. The strength of inhibition determines the spatial scope of an active zone, or the space a traveling bump will traverse in a given time (the dx shown in blue above). The length of an upstate at any given point in space is governed by the strength of the slow potassium conductance $g_{\bar{K}s}$ (illustrated by the red dt above). These two features form the rough approximation of wavespeed dx/dt. As in Fig 2.2., black markers represent spikes from excitatory cells, red markers represent those from inhibitory cells and cells are sorted along the y-axis by spatial coordinate.

experimental results have demonstrated both the importance of stationary bumps in attention tasks [41] and the importance of the muscarinic system in this state [39]. These results suggest that cholinergic modulation of SFA primes a network to focus on incoming information, providing a mechanism for ACh's role in attention [72].

In neural field models, the conditions that lead to the formation of stationary bumps and traveling waves have been well documented [73, 74]. Lateral inhibition is necessary for the formation of stationary bumps and traveling waves [49, 75], and is critical for these results. While my results hold when the range of inhibition is reduced from global, I do need the radius of inhibitory connections to be larger than that of excitation. In fact, I do not believe that traveling waves can form unless the

inhibitory range is larger than that of excitatory connections. While my scheme is supported by some experimental evidence [46, 47], other results have failed to find lateral inhibition as a model for cortical connectivity [76, 77]. While it is possible that the range of synaptic coupling for inhibitory interneurons is shorter than that of excitatory cells, electrical synapses (i.e. gap junctions) could broaden the scope of inhibition. Furthermore, dynamic regulation of gap junctions could allow for network topology to vary according to the requirements of a particular activity regime [78].

In addition to lateral inhibition, SFA also induces traveling waves in both neural field models and in other more complex spiking networks [79, 80]. In other models, SFA causes linearization of the f-I curve in a similar manner as $g_{\bar{K}s}$ [81, 82] and the mechanism we describe here is likely a general phenomenon in the formation of waves in adapting networks. Analytical results from neural fields have related higher thresholds (the level of input required to generate action potentials) to decreased propagation speed of traveling waves [79, 74]. This may disagree with our results, which are that threshold and wave speed increase with $g_{\bar{K}s}$. The threshold in neural field models may relate more to E/I balance in our system than to the threshold for spiking of individual neurons. It is important to note that the model we use does not address other important facets of muscarinic neuromodulation such as resting potential and leak conductances [83], synaptic strength [84], and both Ca^{2+} and Na^{+} dependent K^{+} currents [80, 40], all of which likely play a role in the formation of spatiotemporal dynamics.

That SFA and PRC modulation take place over different ranges of $g_{\bar{K}s}$ allows for three general regimes within networks of this type: localized asynchronous, traveling asynchronous, and traveling synchronous. It is clear from our results that these regimes differ in sensitivity to synaptic heterogeneity (decreasing from localized asyn-

chronous to traveling synchronous) but whether they represent distinct functional states, especially regarding processes such as memory and synaptic homeostasis, need further experimental and computation work.

2.6 Supporting Information

2.6.1 Supporting Figures

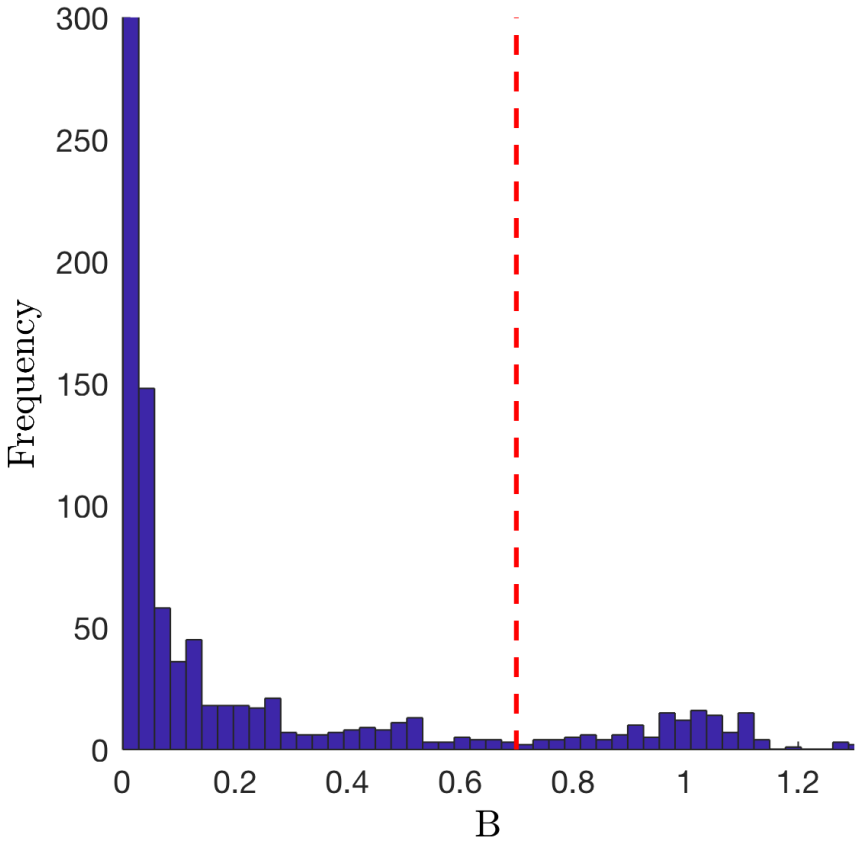

Figure 2.7: **Distribution of bursting values.**
High values of the bursting measure, B, indicate highly synchronous firing. The distribution of B is bimodal and a value of 0.7 (red line) was chosen to exclude highly synchronous dynamics because it divides the distribution.

2.6.2 Fig S2

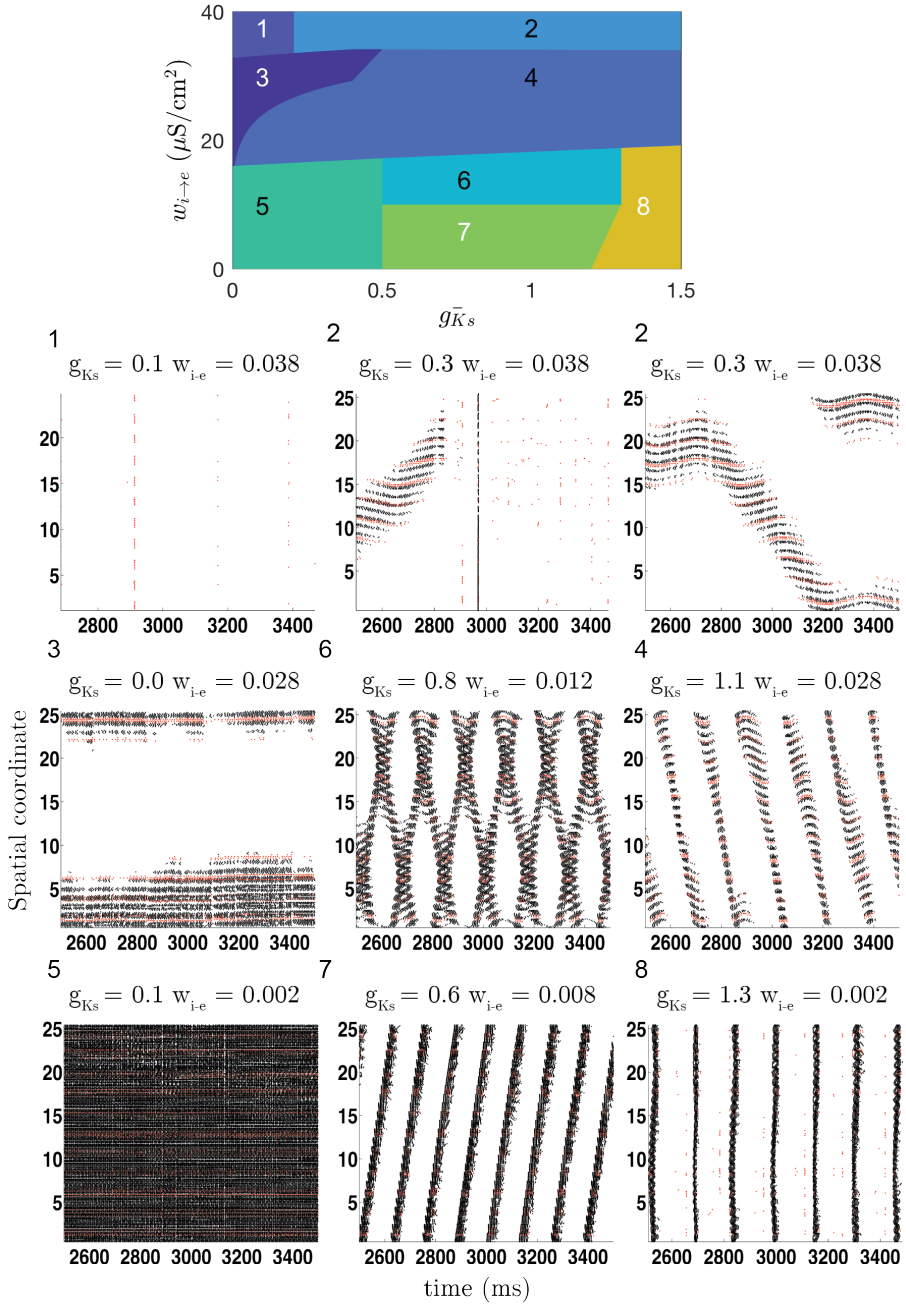

Figure 2.8: **Examples of observed dynamics.**
A broad array of dynamics were observed. The phase cartoon from Fig 2.1D is included with raster plots displaying dynamics. Numbers indicate the following: (1) quiescent (2) mixed dynamics, (3) stationary bump (4) traveling bump (5) global high frequency activity (6) multiple interacting bumps (7) planar wave (8) global burst. Note two examples of mixed dynamics (2) were included to show that traveling waves, stationary bumps, highly synchronized bursts, and quiescence arise during the course of a simulation.

2.6.3 Support Table

Table 2.1: **Table of parameters.**

Neural parameters			
c_m	1.0 $\mu F/cm^2$	$g_{\bar{K}s}$	0-1.5 mS/cm^2
$g_{\bar{N}a}$	24.0 mS/cm^2	g_L	0.02 mS/cm^2
$g_{\bar{K}dir}$	3.0 mS/cm^2	E_{Na}	55.0 mV
E_K	-90.0 mV	E_L	-60.0 mV
α_m	-30 mV	α_h	53 mV
α_n	- 30 mV	α_s	-39 mV
β_m	9.5 mV	β_h	7 mV
β_n	10 mV	β_s	5 mV
γ_h	40.5 mV	γ_n	27 mV
ε_h	6 mV	ε_n	15 mV
D_h	2.78	D_n	1.85
$V_{threshold}$	-20 mV		
Synapse parameters			
τ_F	0.3 ms	τ_S	3 ms
E_e	0 mV	E_i	-75 mV
τ_D	-75 mV		
Network parameters			
$w_{e\to e}$	20 $\mu S/cm^2$	$w_{i\to e}$	0-38 $\mu S/cm^2$
$w_{e\to i}$	20 $\mu S/cm^2$	$w_{i\to i}$	20 $\mu S/cm^2$
L	25 $units$	$Grain_e$	1 $unit$
$Grain_i$	2.27 $units$	k_{ee}	16
k_{ei}	4		

Values of the neural parameters were adopted from [26].

2.6.4 Supporting Videos

Video 2.1: **Network dynamics for inhibitory fraction of 13% and** $g_{\bar{K}s} = 0\text{mS/cm}^2$

Video 2.2: **Network dynamics for inhibitory fraction of 13% and** $g_{\bar{K}s} = 1.5\mathrm{mS/cm}^2$

Video 2.3: **Network dynamics for inhibitory fraction of 22% and** $g_{\bar{K}s} = 0\mathrm{mS/cm}^2$

Video 2.4: **Network dynamics for inhibitory fraction of 22% and** $g_{\bar{K}s} = 1.5\mathrm{mS/cm}^2$

Video 2.5: **Network dynamics for no periodic boundaries and** $g_{\bar{K}s} = 1.5\mathrm{mS/cm}^2$

CHAPTER III

Memory Recall and Spike Frequency Adaptation

. Here I describe a mechanism for the organization of neuronal spiking around oscillatory input and how this organization facilitates network level learning. This chapter was published in the Physical Review E in 2016 (Vol. 93, Pg. 052307).

3.1 Abstract

The brain can reproduce memories from partial data; this ability is critical for memory recall. The process of memory recall has been studied using auto-associative networks such as the Hopfield model. This kind of model reliably converges to stored patterns which contain the memory. However, it is unclear how the behavior is controlled by the brain so that after convergence to one configuration, it can proceed with recognition of another one. In the Hopfield model this happens only through unrealistic changes of an effective global temperature that destabilizes all stored configurations. Here I show that Spike-Frequency Adaptation (SFA), a common mechanism affecting neuron activation in the brain, can provide state dependent control of pattern retrieval. I demonstrate this in a Hopfield network modified to include SFA, and also in a model network of biophysical neurons. In both cases SFA allows for selective stabilization of attractors with different basins of attraction, and also for temporal dynamics of attractor switching that is not possible in standard

auto-associative schemes. The dynamics of our models give a plausible account of different sorts of memory retrieval.

3.2 Introduction

The brain stores memories as patterns of synaptic strengths in the network of neurons. It can store multiple memories and retrieve them in a reliable way, and can change from one to another as attention wanders. However, there is no agreement in the neuroscience community of how this occurs. This paper offers a partial solution to understanding the mechanism for retrieval and switching based on a known physiological effect, SFA.

Decades of work on understanding storage and retrieval have focussed on versions of the Hopfield model (a special form of the Ising model) [85, 86, 87]. Hopfield networks have many attractive features: they are auto-associative: that is, memories are recalled from a fragment of their data because the memories are stored in *attractors*, i.e. metastable states.

However, as in any statistical model at zero temperature there is no mechanism for escaping an attractor: a single memory pattern would exist for all time. To overcome this problem an artificial 'temperature' is introduced in Hopfield models to allow switching. This 'temperature' (i.e fast random noise in synaptic current) has no obvious biological origin. Thus, despite the elegance of the model, and its utility in computer science, its application to the brain is problematic. Previous efforts to over come this limitation have used feedback input [88], synaptic depression [89], and adaptive mechanisms [90]. As we will see, SFA allows escape from attractors, and, in some cases acts in the same way as increased temperature level. In addition, it can destabilize specific memories that were active over prolonged period of time rather

than globally destabilizing the network, as temperature does.

SFA is an activity induced reduction in neural firing rate induced by a hyperpolarizing current that increases as a neuron fires (i.e. when a neuron fires a lot, it tends to stop firing). SFA is a natural mechanism to turn off activity. Further, SFA can be controlled by neuromodulators such as Acetylcholine (ACh), an important regulator of neural excitability. ACh causes a reduction in SFA and provides for its dynamic regulation [45, 21]. In Chapter II I have presented a network model of Hodgkin-Huxley (HH) neurons with SFA and 'Mexican Hat' coupling which reproduces many features of cortical activity as ACh levels change between sleep and waking states. In the present Chapter I use this model to concentrate on memory retrieval. However, we claim that the essentials of our results are quite robust and independent of the details of the neuron model. To show this, we first consider a version of the Hopfield model [85, 86, 87] which has SFA.

3.3 Methods

3.3.1 Hopfield Model

We consider networks composed of N=1000 spins, $S = \{s_i\}$ where $s_i = \pm 1$. The network is fully connected with weights $\sigma_{i,j}$. As usual, spin up corresponds to a neuron that fires, and spin down to a silent one. Each spin gets an input:

$$h_i(t) = \sum_{j=1}^{N} \sigma_{i,j} s_j - \theta_i(t), \tag{3.1}$$

where $\theta_i(t)$ is a local offset field at site i which changes slowly in time. The first term is the usual Hopfield-Ising term and the second represents SFA.

The dynamics of the spins are as follows: at each time step a random spin is flipped with probability:

$$P_h(s_i) = \frac{1}{1 + e^{-2 s_i h_i / T}}, \tag{3.2}$$

where T is the noise. In much of what follows we take T to be very small so that P_h is essentially a step function.

The dynamics of θ_i is:

$$\theta_i(s_i) = \frac{A}{1 + e^{-s_i(\hat{t}-\tau_1)/\tau_2}}. \tag{3.3}$$

Here, $\hat{t}$ is the time since the last state change of the spin, and $\tau_{1,2}$ are time constants which govern the dynamics of attractors. The field θ increases to A for up spins and decreases to zero for down spins. The time constant τ_1 is the time to the half-maximum value of θ_i. We take $\tau_1 = 5$ (timesteps/N), except for the data in Figure 3.1 where $\tau_1 = 1.5$ (timesteps/N). The rate at which SFA activates/ deactivates is controlled by τ_2 which is set to 0.2, except for the data in Figure 3.4 where $\tau_2 = 0.6$ (timesteps/N). This implementations of adaptation is different than others in the hopfield model [90]. because it integrates over a longer time (i.e. considers more than the activity at the previous time step). This more closely resembles adaptation in biophysical models.

In the Hopfield scheme memories are stored as attractors, i.e. metastable configurations, $\Xi^\mu = \{\xi_i^\mu\}$. We encode attractors using a modified Hebbs rule [85]:

$$\sigma_{i,j} = \frac{1}{NW} \sum_{\mu}^{p} w_\mu \xi_i^\mu \xi_j^\mu. \tag{3.4}$$

Each attractor is given a weight, w_μ and $W = \sum_\mu^p w_\mu$. Thus $\sigma_{i,j} = 1$ for two spins with correlated activity across all attractors, Ξ^μ, and -1 for spins with anti-correlated activity. We set $w_1 : w_{p-1} = 0.5$ and $w_p = 1$, except for the data reported in Figure 3.4D where all the weights $w_i = 1.0$. The saturation is defined as $\alpha = p/N$. Attractors encoded with lower w_μ are weaker attractors.

In order to determine if the dynamics has settled into the various Ξ^μ we measure the Mattis magnetization, which is the overlap between the stored memory and the

current state:

$$m_\mu = \frac{1}{N}\sum_i^N s_i \xi_i^\mu, \tag{3.5}$$

which is ± 1 when $S = \pm\Xi$ and 0 when $S \perp \Xi$. In each simulation S was always initialized to a random weak attractor, Ξ_{weak}.

3.3.2 Biophysical Model

We use a spiking network model introduced previously which considers $N_E = 1225$ excitatory and $N_I = 324$ inhibitory HH neurons arrayed on two square lattices of size $L_{E/I}$. The coupling was of lateral inhibition (Mexican Hat) type where short range excitation is balanced with global inhibition. All excitatory neurons were connected to neighbors within radius $R_{xx} = \sqrt{L_{E/I}^2 k_{xx}/\pi N_{E/I}}$ where $k_{ei} = 16$ is the degree of excitatory to excitatory connections, $k_{ei} = 4$ is the degree of excitatory to inhibitory connections. Neural dynamics were modeled by the current balance equation [22]:

$$\begin{aligned} c_m \frac{dV_i}{dt} &= -g_{Na} m_\infty^3 h(V_i - E_{Na}) - g_{Kdir} n^4 (V_i - E_K) \\ &\quad - g_{\bar{K}s} s(V_i - E_K) - g_L(V_i - E_L) - I_{syn,i} + I_{ext} \end{aligned} \tag{3.6}$$

In this equation, as we will see, $g_{\bar{K}s}$ sets the magnitude of the SFA; it corresponds to A in the model above.

The dynamics of the gating variables h, n and s is of the form $dx/dt = (x_\infty(V) - x)/\tau_x(V)$ with additional specific evolution of the two voltage dependent parameters x_∞ and τ_x. The slow potassium current conductance, $g_{\bar{K}s}$ controls the level of SFA (i.e. lower values of $g_{\bar{K}s}$ correspond to low SFA). The level of ACh modulates $g_{\bar{K}s}$: the maximum ($g_{Ks} = 1.5$ mS/cm^2) and minimum ($g_{Ks} = 0$) correspond to the absence or maximum of ACh, respectively. For more details see [34].

The synaptic current to neuron i is $I_{syn,i} = g_E(t)(V_i - E_E) + g_I(t)(V_i - E_I)$ and the dynamics of $g_{E/I}(t)$ is:

$$g_{E/I}(t) = K \sum_{j}^{\in E/I} \sigma_{i,j}(e^{\frac{-(\tilde{t}_j - \tau_D)}{\tau_S}} - e^{\frac{-(\tilde{t}_j - \tau_D)}{\tau_F}}) \tag{3.7}$$

where $\sigma_{i,j}$ is the synaptic weight between neuron i and neuron j, and $\tau_{S,F}$ are time constants equal to 3.0 and 0.3 ms respectively. $\sigma_{i,j}$ is set to 0.02 mS/cm^2 unless otherwise stated, $\tilde{t}_j$ is the time since the last spike of neuron j, and K is a normalization constant. I_{ext} set so that all neurons fire at 10 Hz in the absence of synaptic input and for any $\bar{g_{Ks}}$. The equations were integrated using the 4th order Runge-Kutta method at a 0.05 ms time step to 20 s. Data points are averages of 20 sets of initial conditions.

3.4 Results

I first investigated recall dynamics of the Hopfield network as a function of SFA amplitude. In the usual Hopfield model the preference for local, global, or no attractors changes as the noise, T, increases [85, 91]. This transition depends on the saturation α [85]. I find analogous network behavior as we increase the magnitude of SFA, i.e. A. To show this I compare the standard T versus α plot with a plot of A versus α in Figure 3.1. The right panel shows how T and α interact to affect the stability of the strong and weak attractors and, eventually, to destabilize all attractors. For small T the dynamics keeps the system in a weak attractor (blue on the colormap); for larger T the system enters a regime of stability of stronger attractors (yellow). For large T no attractors are stable (green).

SFA has analogous effect in terms of overall destabilization of attractors of particular strength; see Figure 3.1, left. To see how this comes about, I investigate the stability of an attractor of a given weight by mean field theory [92, 91, 93]. The

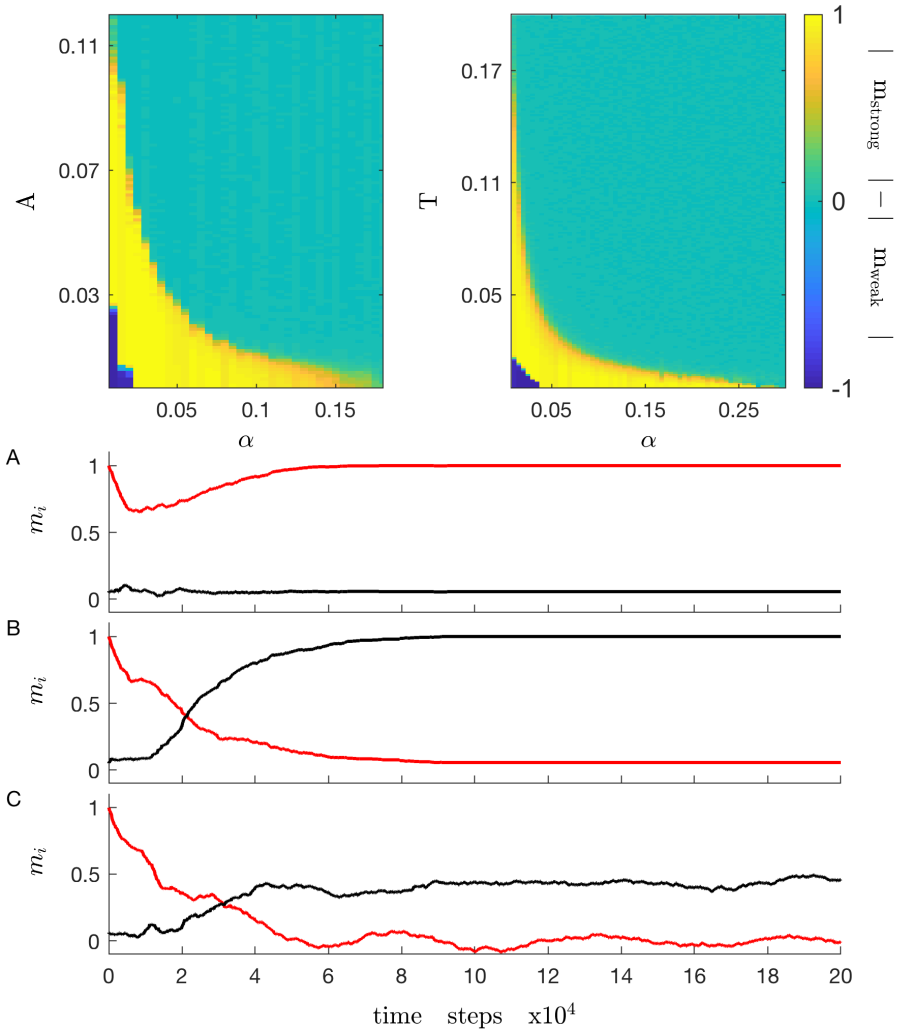

Figure 3.1: **SFA and T control attractor stability in Hopfield networks.** With noise Hopfield networks have three functional states: stability of local attractors, stability of subset of strong attractors, and stability of no attractor. These changes of stability is shown by the ability of the attractor to move from a weak attractor to a strong one, which is quantified by the difference of the m_μ of the strong attractor and the weak attractor in which the system was initialized. (*Top*)The saturation of memories (α), noise (T), and adaptation (A) affect stability in a similar manner. For low levels of noise local (weak) attractors are stable (blue). For a given α either increasing A (left) or T (right) leads to a strong attractors being stable (yellow). Further increase destabilizes all attractors (green). (*Bottom*) Example dynamics of memory overlap, m_i, for strongly (black) and weakly (red) weighted memories. In each case $\alpha = 0.01$; adaptation levels are (A) A = 0.01 (B) A = 0.05 (C) A = 0.3.

mean field equations for the system are:

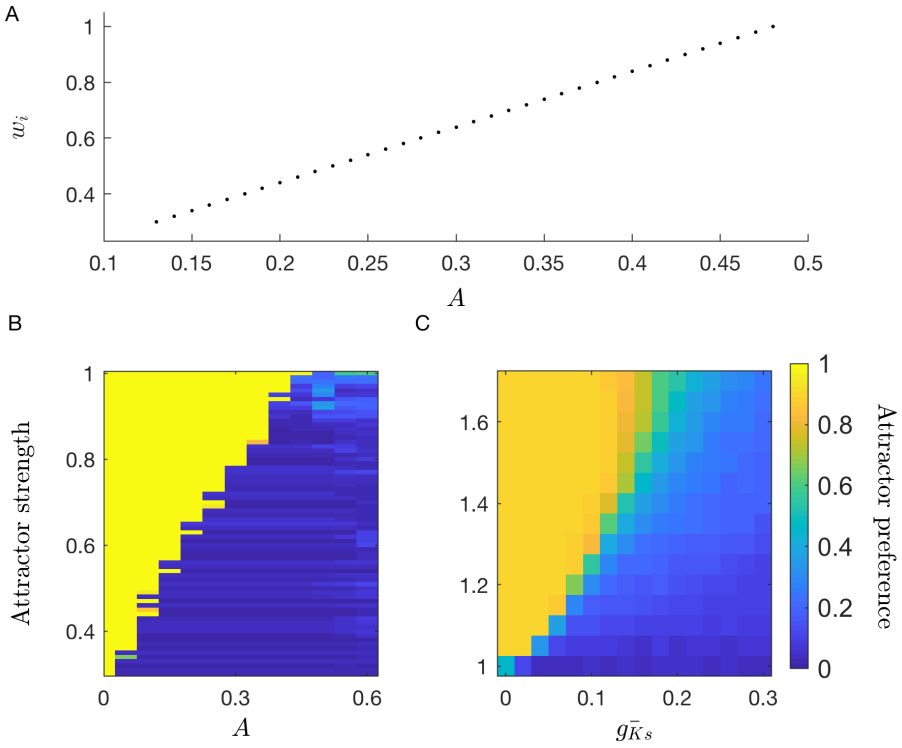

Figure 3.2: **Attractor stability varies as a function of** A. For SFA to induce the network to leave a attractor it must be large enough to overcome the energy barrier of that attractor. Mean field calculations predict a linear relationship between the strength of an attractor and the amount of adaptation, A, to destabilize it (A).This is best seen in the Hopfield model (B). The threshold value of A increases linearly as the attractor strength, w_μ increases. A similar effect is seen in the spiking network model (C).

$$\langle s_i \rangle = \tanh(\frac{\beta}{NW} \sum_{j,\mu} w_\mu \xi_i^\mu \xi_j^\mu \langle s_j \rangle - 2\theta_i), \tag{3.8}$$

where $\beta = 1/T$. By exploiting the fact that $\langle s_i \rangle = m\xi_i^\upsilon$ the mean field equations can be rewritten as:

$$m\xi_i^\upsilon = \tanh(\frac{\beta}{NW} \sum_{j,\mu} w_\mu \xi_i^\mu \xi_j^\mu m\xi_i^\upsilon - 2\theta_i). \tag{3.9}$$

If $p \ll N$ any overlap between memories is negligible so the mean field equation and the system is in memory υ for a time $\gg \tau_1$ becomes:

$$m\xi_i^\upsilon = \tanh(\beta w_\upsilon m\xi_i^\upsilon - \frac{1}{T}2A), \tag{3.10}$$

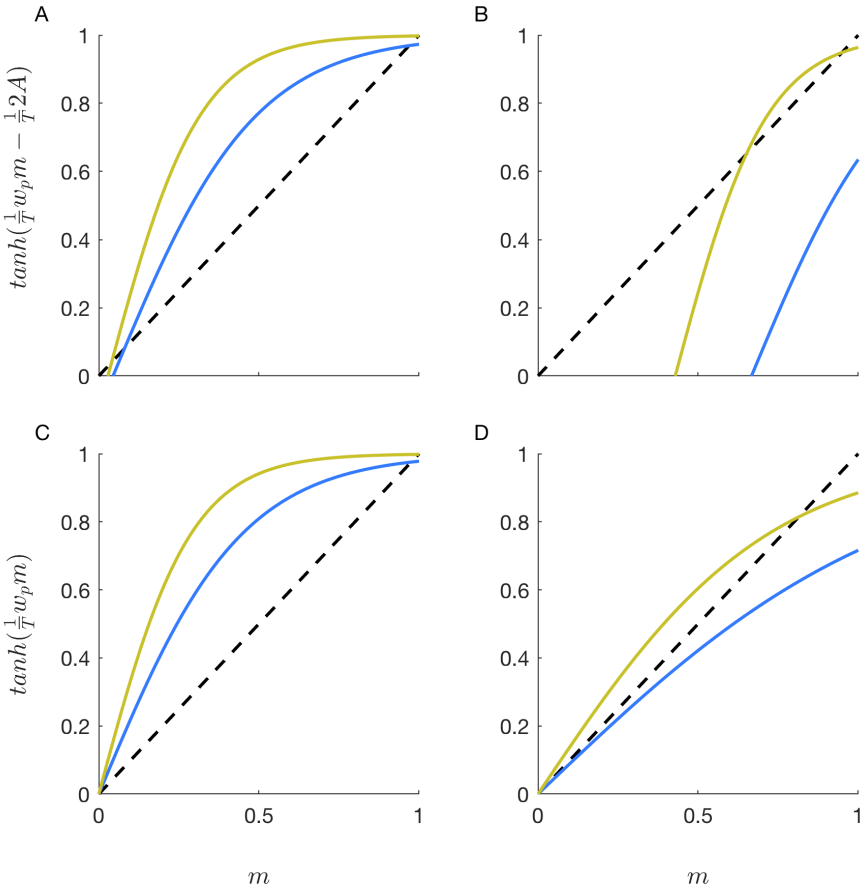

Figure 3.3: **SFA and T destabilize attractors of different strengths in Hopfield networks.** Solutions to mean field equations illustrate how adaptation and temperature destabilize weak attractors. When A is low all memories are stabile (panel A; A=0.1). Increasing A destabilizes weak memories while preserving strong memories (panel B; A=0.25). When adaptation is absent temperature has a similar effect where all memories are stable for low T (panel C; $T = 0.2$), while only strong memories are stable for high T (panel D; $T = 0.5$). The dashed line shows $m = m$; the solid blue line shows the mean field equation for $w_\upsilon = 0.45$; the solid gold line shows the mean field equation for $w_\upsilon = 0.75$.

which be simplified to $m = \tanh(\beta w_\upsilon m - \beta 2A)$. When this equation has solutions beyond $m = 0$ a memory with strength w_υ is stable for a given T or A. Figure 3.3 shows mean field solutions for memories with strengths $w_\upsilon = 0.45$ (blue line) and $w_\upsilon = 0.75$ (gold line). As in the numerical results adaptation (Fig 3.3 top panels) and temperature (bottom panels) have similar effects on the stability of memories. For low levels ($A = 0.1$, $T = 0.2$; left panels) both strong and weak memories are

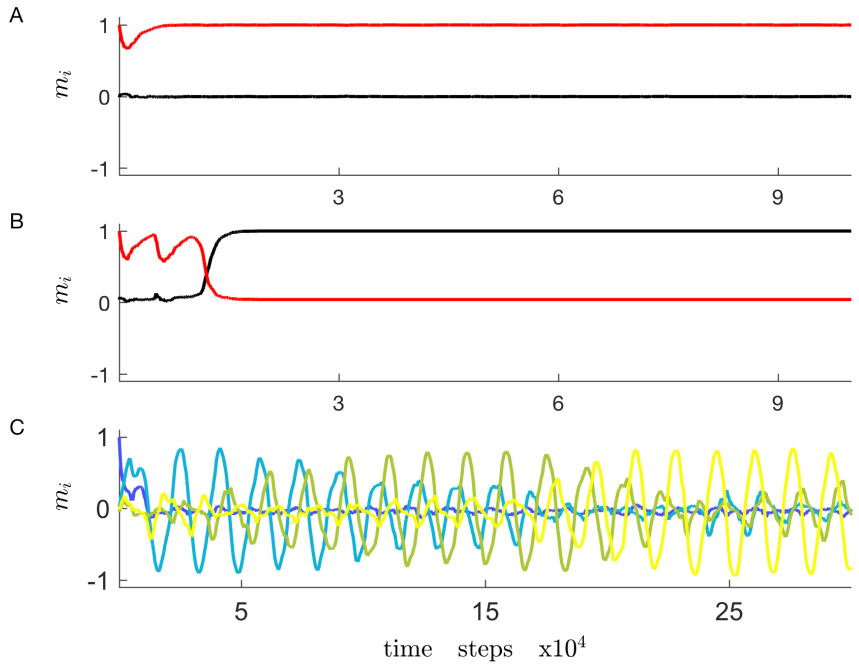

Figure 3.4: **Examples of network dynamics in the modified Hopfield model.** For small A even a weak attractor is stable (panel A; A = 0.01). A moderate increase leads to the strong attractor becoming stable (B, A = 0.1). For larger A damped oscillations with period $\sim 4\tau_1$ emerge: C, A = 0.4. In panels A and B the red line corresponds to a weak attractor and the black corresponds to a strong one. In panel C, the dark blue is the weakest attractor. All other lines are strong attractors of equal weight.

stable (i.e. both have solutions beyond $m = 0$), but moderate increases in A or T destabilize weaker memories ($A = .25$, $T = 0.5$; right panels)

Thus, changes in the strength of SFA can play the same role as changes in T by destabilizing attractors of varying strength as A increases. Interesting time-dependent effects occur for intermediate values of A when the τ's are not too large. Because θ_i is a function of t we can generate chains of attractor preferences, as opposed to stability in a deep attractor or a random walk (as in the standard Hopfield model for large T). These results are shown in Figure 3.4. For small A local, weak attractors are stable. A moderate increase leads to strong attractors being stable (Figure 3.4 A, B). Further increase of A leads to oscillations of period $\sim 4\tau_1$; Figure 3.4 C. This is similar to the latching dynamics found in [90].

To demonstrate the robustness and biological relevance of these results I now turn to the biophysical model. I have shown [34] that the nature of the dynamics is that for small $g_{\bar{K}s}$ (large concentrations of ACh) there is a stationary, localized region (a 'bump') of spiking activity. For larger $g_{\bar{K}s}$ the bump travels through the lattice.

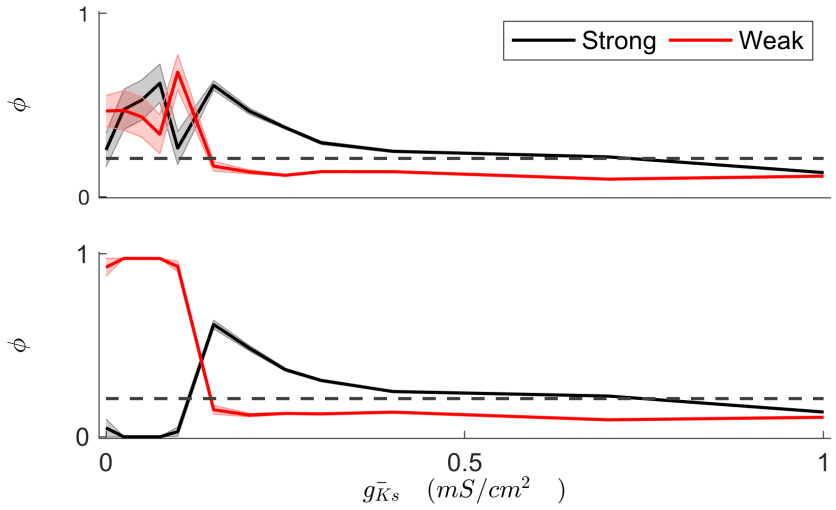

Figure 3.5: **Attractor preference and $g_{\bar{K}s}$.** The quantity ϕ is the fraction of time that activity is located within an attractor. Gray dashed line, control value. (Top) For initial locations outside any attractor no clear preference emerges for small $g_{\bar{K}s}$. For moderate $g_{\bar{K}s}$ there is clear preference for the strong attractor. (Bottom) For initial conditions within the weak attractor activity never leaves for small $g_{\bar{K}s}$. There is significant preference for the strong attractor for moderate $g_{\bar{K}s}$. Errorbars = $\pm$ s.e.m.

To consider memory we introduce spatial attractors by increasing synaptic strength in certain locations of the network [32, 34]. These attractors fix the location of the bump when the dynamics is in the stationary regime. For a single attractor, preference for the attractor falls as $g_{\bar{K}s}$ increases [34]. This model is quite different from the one discussed above: the excitatory coupling is short-ranged in contrast to the Hopfield σ's which are long-ranged, and thus the attractors here are defined by local geometry. Nevertheless, SFA gives common results for the two cases.

To consider multiple attractors of variable strength we increased synaptic strength in two network regions at opposite ends of the lattice. The strong attractor had

100% stronger excitatory connections and the weak attractor had a 50% increase. To examine how network preference changed as a function of g_{Ks}^{-} in multi-attractor networks we did simulations where activity was initialized by injecting a 0.25 μA/cm^2 current to a region outside either of the attractors for the first 0.5 s of the simulation. Preference for a given attractor was quantified by the measure ϕ which is the fraction of time that the center of the bump, calculated according to [50], is located within the attractor. For low levels of SFA there is no clear preference indicating that activity localizes to attractors randomly; Figure 3.5, top. Increasing g_{Ks}^{-} leads to a clear preference for the strong attractor. The preference for any attractor disappears for large g_{Ks}^{-} as the network enters the regime of traveling bump dynamics.

To further test the stability of the two attractors I initiate network dynamics by activating the weak attractor. For small g_{Ks}^{-} activity remained localized there: Figure 3.5, bottom. For larger g_{Ks}^{-} activity moved to the stronger attractor. This confirms that the strength of SFA can control the stability of attractors having different depths.

I also considered how the relative stability of the attractors depends on the ratio of inhibitory to excitatory coupling, $w_{e/i}$). Figure 3.6 is a phase plot of final attractor preference for different $w_{e/i}$) and g_{Ks}^{-}. The relative preference for the two attractors was measured by $\phi_{strong} - \phi_{weak}$, which ranges between 1 (preference for the strong attractor) and -1 (preference for the weak). Interestingly, weakening inhibition abolishes any preference for the strong attractor at intermediate levels of g_{Ks}^{-}.

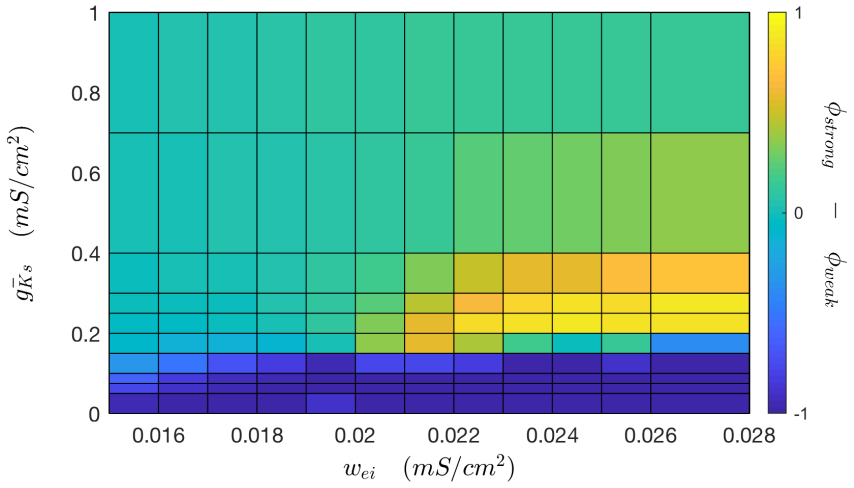

Figure 3.6: **Strong attractor preference is controlled by inhibition strength in spiking networks.** We measure the differential attractor preference for the two attractors by $(\phi_{strong} - \phi_{weak})$, which is 1 when all activity is located within the strong attractor and -1 when all activity is within the weak. The preference for the strong attractor at moderate SFA disappears when inhibition is decreased.

3.5 Discussion

We have shown for both, biophysical and Hopfield models SFA can selectively destabilize attractors effectively controlling attractor preference. With SFA we can have long-term preferential activation of attractors of different strengths and also non-trivial time dependence of attractor sequences. This provides a biologically plausible mechanism for switching between encoded patterns [91, 94].

In the biophysical model SFA depends on ACh [22, 21, 20]. Our results imply that ACh controls memory retrieval dynamics. Note the relevance of our results to context dependent release of ACh and its role in attention [95]. During tasks requiring a high degree of focus, low SFA allows the brain to fix on the memory that closely fits the current sensory input. On the other hand, with high ACh the attractor can be reinforced by synaptic plasticity. As attention requirements are relaxed, and ACh levels fall, moderate levels of SFA allow for sampling of the memory space, see

[96].

The largest variation in cortical ACh levels occurs between sleep/ wake states. In this case the highest levels occur during Rapid Eye Movement (REM) sleep and the lowest during slow wave sleep [97]. We argue that intermediate levels of ACh during wake states allow for memory recall when externally driven network states are allowed to wander to find the optimal state. REM sleep is thought to be important for memory consolidation, where retrieval of weakly stored attractors of previous experience is essential to their consolidation. Non-REM (NREM) sleep associated with low ACh levels is characterized by slow waves and may play a role in synaptic rescaling [60].

CHAPTER IV

Resonance with subthreshold oscillatory drive organizes activity and optimizes learning in neural networks.

Here I describe a mechanism for the organization of neuronal spiking around oscillatory input and how this organization facilitates network level learning. I would like to thank Nicolette Ognjanovski and Sara Aton for performing the neuronal recordings from the hippocampus. This chapter was published in the Proceedings of the National Academy of Sciences in 2018 (Vol. 115, Pg. E3017).

4.1 Abstract

Network oscillations across and within brain areas are critical for learning and performance of memory tasks. While a large amount of work has focused on the generation of neural oscillations, their effect on neuronal populations' spiking activity and information encoding is less known. Here, I use computational modeling to demonstrate that a shift in resonance responses can interact with oscillating input to ensure that networks of neurons properly encode new information represented in external inputs to the weights of recurrent synaptic connections. Using a neuronal network model, I find that due to an input-current dependent shift in their resonance response, individual neurons in a network will arrange their phases of firing to represent varying strengths of their respective inputs. As networks encode infor-

mation, neurons fire more synchronously, and this effect limits the extent to which further "learning" (in the form of changes in synaptic strength) can occur. I also demonstrate that sequential patterns of neuronal firing can be accurately stored in the network; these sequences are later reproduced without external input (in the context of subthreshold oscillations) in both the forward and reverse directions (as has been observed following learning in vivo). To test whether a similar mechanism could act in vivo, I show that periodic stimulation of hippocampal neurons coordinates network activity and functional connectivity in a frequency-dependent manner. I conclude that resonance with subthreshold oscillations provides a plausible network-level mechanism to accurately encode and retrieve information without over-strengthening connections between neurons.

4.2 Introduction

Oscillations in Local Field Potential (LFP) largely reflect coherent post-synaptic potentials among neurons [98]. These rhythms are behaviorally relevant, and their features are highly predictive of cognitive processes, and plasticity, in underlying neural networks [99, 98, 100, 101, 102]. Network oscillations have long been thought to promote plasticity by precisely timing firing between pairs of neurons (i.e., driving Spike Timing-Dependent Plasticity (STDP)] [11, 103]. However, it is still unclear whether specific network rhythms are critical for specific neural computations, and if so, why this is the case.

Neurons display complex behavior in response to oscillatory input. Many neuronal subtypes show enhanced membrane voltage responses to periodic subthreshold inputs within narrow frequency bands [104, 105, 106]. Critically, the frequency at which neurons resonate can shift in response to depolarizing or hyperpolarizing inputs

[107, 108, 109]. Thus in addition to simply integrating inputs to generate an action potential, neurons are biophysically suited to perform time-dependent computations, including input filtration, based on their periodicity.

The theta (4-10 Hz) rhythm is a prominent oscillation present in mammalian brain networks [100]. Within the hippocampus, theta plays a central role in the function of place cells, which encode spatial and contextual information [110, 111]. Place cells show several interesting features associated with theta-resonant firing. First, their firing phase varies over time, relative to hippocampal theta - a phenomenon called phase precession, which occurs as animals move though their environment [112, 11, 113]. Second, sequences of place cell activation occurring during spatial exploration are replayed during subsequent theta oscillations, and surprisingly, these replay events can occur in either the forward or reverse direction [114, 115, 116, 117]. While the idea that theta (and other hippocampal oscillations) plays a role in hippocampal function is widely accepted, the underlying mechanisms for phase precession, forward replay, and reverse replay - and the link of these features to memory formation - are still largely unknown.

Networks of neurons that display resonance shifts (i.e. the firing response to subthreshold oscillating input changes as a neuron is depolarized) show enhanced pattern formation and separation when rhythmic inputs are present [118, 119]. Here I show that resonating networks have a firing pattern that is highly beneficial for both encoding and retrieving patterns of external inputs. Using conductance-based model neurons which display resonance with subthreshold oscillatory input, I show that networks will organize the firing of neurons around an oscillation in a manner that represents an external input. When synapses are able to evolve via a STDP rule, an input will be reliably encoded within the synaptic weights of a network. This leads

to the subsequent reproduction of the input-induced firing pattern in the absence of the external pattern, for both static and temporally dynamic inputs. I also show that resonance with subthreshold oscillations provides a network-level mechanism both for theta phase precession and for forward and reverse replay, that reliably happens across any resonant frequency. Finally, I find that subthreshold periodic input induces stable, highly organized functional connectivity over the theta band, in both simulated and in vivo networks. This work demonstrates that resonance with subthreshold oscillations organizes neuronal firing phase with respect to network rhythms, and thereby facilitates the encoding and retrieval of information.

4.3 Methods

4.3.1 Neuronal network model

I use a network model that is composed of $N = 300$ (or $N = 1000$ for the data in Figures 4.6 and 4.7) excitatory neurons. Neuronal dynamics were based on a conductance-based model (Ks model) and governed by the current balance equation:

$$c_m \frac{dV_i}{dt} = -g_{Na} m_\infty(V) h(V)(V - E_{Na}) - g_{Kdir} n(V)(V - E_K) - g_{\bar{K}s} s(V)(V - E_K) - g_L(V - E_L) - I_{syn_i} - I_{ext_i} \tag{4.1}$$

The gating variables h, n, and s were of the form $dx/dt = (x_\infty(V) - x)/\tau_x(V)$. The slow potassium conductance, whose maximum value is g_{Ks}, is largely responsible for the resonance displayed by this neuron model and its value was set to 1.5 mS/cm^2. Additional details of the neuronal dynamics can be found in [22]. Ks model neurons display a depolarization dependent spiking resonance to subthreshold inputs in the 4 - 20 Hz range.

Additionally, I used a second conductance based neuronal model using the Hodgkin-Huxley [1] model and parameters (Hodgkin-Huxley (HH) model) which resonated between 40-90 Hz to produce the data in Figure 4.3. Membrane potential dynamics were governed by the current balance equation:

$$c_m \frac{dV_i}{dt} = -g_{Na} m(V) h(V)(V - E_{Na}) - g_K n(V)(V - E_K) - I_{syn_i} - I_{ext_i} \tag{4.2}$$

The gating variables m,h, and n evolved according to $dx/dt = \alpha_x(V)(1-x) - \beta_x(V)x$, where α_x, β_x, and other parameters are taken from [1].

For both neuronal models, I_{ext_i} was split into two components. The first is $I_{osc} = A_{osc} cos(2\pi f_{osc} t)$ (except for Figure 4.12; see SI), which is identical for each neuron in the network. Cosine was chosen so the when f_{osc} was set to zero (i.e. no oscillation), all neurons would receive the same peak current as Direct Current (DC). The second component was either I_{DC_i}, which is a unique for each neuron, or in the case of data in Figures 4.6 and 4.7 $I_{act,g}$ which is a slowly varying activation current defined by the modified Gaussian function:

$$I_{act,g}(t) = \frac{2e^{\frac{-(t-\mu_g)^2}{2\sigma^2}}}{\sqrt{2\pi\sigma^2}(1 + e^{\frac{-1.702\lambda(t-\mu_g)}{\sigma}})}. \tag{4.3}$$

where g is the group to which a neuron is assigned (one of five groups), μ_g is the time of maximum activation of that group, $\sigma = 4000$ ms the width of the activation function, and $\lambda = 8.0$ is the skewness parameter. This leads to an activation time course that slowly grows to 227 nA/cm^2 then rapidly decays to zero (Fig 4.6A).

Synaptic input was modeled as a double exponential conductance pulse with the dynamics:

$$g_{syn,i}(t) = M_{syn} \sum_{j}^{N} \sigma_{i,j}(exp(\frac{-(\hat{t}_j - \tau_D)}{\tau_S}) - exp(\frac{-(\hat{t}_j - \tau_D)}{\tau_F})). \tag{4.4}$$

The decay constants, τ_S and τ_F, were set to 250.0 and 0.3 ms respectively. The synaptic delay constant, τ_D, was set to 0.08 ms and $\hat{t}_j = t - t_j$ where t_j is the time of the last spike of the presynaptic neuron j. M_{syn} is a synaptic multiple used to account for differences in the input resistance of the two neuronal models; it is set to 1.0 for the Ks model and 10.0 for the data in Figure 4.3. The behavior of the HH model is robust to a range of M_{syn} values (Fig 4.15). Total synaptic current to a neuron was defined as $I_{syn,i} = g_{syn,i}(V_i - E_{syn})$ where E_{syn} is 0 mV. Networks had a ring lattice structure and a connectivity rate of 6%. The connectivity scheme was small world and achieved through the Watts-Strogatz method with a rewiring probability of 0.2 [23].

Synapses evolved according to an additive STDP rule, where the weight change of a synapse between a presynaptic neuron i and a postsynaptic neuron j is defined by:

$$\Delta\sigma_{i,j} = \begin{cases} A_L e^{\frac{-|\Delta t|}{\tau_{STDP}}}, & \Delta t > \quad \hat{\tau}_{STDP} \\ -A_L e^{\frac{-|\Delta t|}{\tau_{STDP}}}, & \Delta t < -\hat{\tau}_{STDP}. \end{cases} \tag{4.5}$$

Here $\Delta t = \hat{t}_j - \hat{t}_i$, where $\hat{t}$ is the time of the last spike fired by a given neuron. τ_{STDP} is the time constant the the effect of a spike decays and is set to 10 ms. $\hat{\tau}_{STDP}$ is a symmetrical region around $\Delta t = 0$ for which there is no synaptic change and is set to 1.5 ms. A_L was the learning rate and was set to 20 nS for all simulations except in Figure 4.4. Synapses were bounded in the region $\in [0, \infty)$ and initialized at 0.2 nS.

All numerical simulations were performed at a time step of 0.05 ms for the Ks model and 0.01 ms for the HH model using a fourth order Runge-Kutta algorithm. All summary data takes data from 5 realizations of the model, except for data in Figure 4.3D, which showed average ± s.e.m. firing phase over 10 periods in one simulation.

4.3.2 Stimulation and recording of hippocampal networks

All procedures were approved by the University of Michigan Institutional Animal Care and Use Committee and performed by Nicolette Ognjanovski under the supervision of Sara Aton. Pvalb-IRES-CRE mice ((B6;129P2-Pvalbtm1(cre)Arbr/J; Jackson) were crossed to B6;129S-Gt(ROSA)26Sortm32(CAG-OP4*H134R/EYFP)Hze/J mice (Jackson) to generate PV::ChR2 mice, which expressed channelrhodopsin (ChR2) in PV-expressing (PV+) interneurons. By rhythmically activating these neurons in the hippocampus with 473 nm light, principle cells within the network were received subthreshold periodic inhibitory stimulation. For all recordings, PV::ChR2 mice ages 2-5 months (n = 4)were anesthetized with isoflurane and chlorprothixene (1 mg/kg IP). Mice were head-fixed and a 1 mm x 1 mm matrix multielectrode (250 μm electrode spacing; Frederick Haer Co. (FHC), Bowdoin, ME) was slowly advanced into CA1 until stable recordings (with consistent spike waveforms continuously present for at least 30 - min before baseline recording) were obtained. An optical fiber was placed adjacent to the recording array for delivery of 473 nm laser light (Crysta-Laser). Power output at the fiber tip was estimated at 3 - 10 mW for all experiments. CA1 neurons were recorded over a 15 - min baseline period, after which PV+ interneurons were stimulated over multiple successive 15 - min periods with a range of frequencies (2 - 18 Hz, 40 ms pulses). The various stimulation frequencies were presented in a random interleaved manner, during which neuronal activity continued

to be recorded. Only those neurons recorded throughout the entire experiment were included in analyses of optogenetically induced spike-field coherence and network stability changes. For in vivo data, 80 and 68 neurons, respectively, met inclusion criteria for coherence and stability analysis. This data set also appeared in [120].

4.3.3 Functional network structure

Functional network structure was calculated for both simulated and recorded networks in a similar manner. The first measure was spike wave coherence which was calculated as the range of the spike-triggered average of the LFP over a window of $\pm$ 50 ms normalized by the peak amplitude of the LFP. In simulated networks the LFP was the sum of all synaptic currents. This value ranges between 0, when spikes occur randomly in the LFP oscillation, and 1, when spikes always occur at the same time.

The second measure of functional network structure was the stability of functional connections though time [121, 120]. The basis of functional connectivity was the average temporal proximity of spikes between neurons and given by $AMD_{ij} = \frac{1}{N}\sum \Delta t^i_{kk}$ for the i-th to j-th neurons. Here Δt^i_k is the time difference between the k-th spike fired by neuron j and the nearest spike fired by neuron i. To determine whether neurons i and j are functional connected AMD_{ij} is compared to the null value given the firing rate of neuron j and random firing of neuron i by the Z-score $FC_{ij} = \sqrt{N_i}\frac{\mu_j - AMD_{ij}}{\sigma_j}$. The null distribution of MD is dependent on the Inter-Spike Interval (ISI) of neuron j. For an ISI of length L, the first two moments of MD are $\mu^L =< MD^L >= L/4$ and $< (MD^L)^2 >= L^2/12$. We will find an ISI of length L within a spike train of length T with a probability of $p_L = L/T$. Thus all the intervals in the spike train of neuron j the expected value is $\mu_j =< MD_j >= \sum_L p_L \mu^L = \frac{1}{T}\sum_L \frac{L^2}{4}$. The expected standard devia-

tion is $\sigma_j^2 =< (MD_j)^2 > - < MD_j >^2$ where $< (MD_j)^2 >= \frac{1}{T}\sum_L \frac{L^3}{12}$. To measure the stability of inferred functional connections spiking data were separated by into non-overlapping time windows for which FC_{ij} values were aggregated into matrices FC_t. Between adjacent time windows cosine similarity, defined by $C_{t,t+1} = \frac{<FC_t, FC_{t+1}>}{\sqrt{<FC_t, FC_t> \times <FC_{t+1}, FC_{t+1}>}}$, was used to quantify the change in functional network structure as a value between 0 (randomized) and 1 (no change). The stability of the functional network was quantified as the average similarity between adjacent time windows. Time windows were 2s for simulated data and 1 minute for recorded data.

4.4 Results

I investigated how resonance with subthreshold oscillations affects pattern and sequence learning, using modeled networks of neurons that receive three types of input (Fig 4.1A). First, each neuron in the network receives a unique level of external, DC indicated by the color map. Second, the entire network receives uniform oscillating input (with modifiable frequency and magnitude). Third, individual neurons receive the summed presynaptic input from other neurons in the network. The weights of individual synapses evolve via STDP across the learning phase of simulations.

4.4.1 Input dependent resonance shift allows for selective activation of subsets of neurons

The neurons in the model display input-dependent resonance shifts (Fig 4.1B). A neuron will respond to a wider range of oscillation frequencies if it receives a larger DC input. There are two main regimes apparent in the resonance profile: 1) a 1:1 regime where the neuron fires one spike per cycle at low frequencies, and 2) a 1:2 regime where the neuron fires every other cycle at high input frequencies. For an

oscillation of 0 Hz (i.e. in the absence of any oscillation), an additional DC current is added to the DC input so that neurons receive the same total input magnitude as when an oscillation is present. This case does not lead to neuronal spiking.

The broadening of the resonance response occurs within networks as well (Fig 4.1C). To show this we formed three clusters within a network with varying intra-cluster coupling (0.2, 1.0, and 1.4 mS/cm2), while keeping inter-cluster coupling constant. This leads to groups with high (green), moderate (light blue), and low (dark blue) synaptic input. The raster plots in Figure 4.1D-F show network activity at 12, 14, and 16 Hz and demonstrate how increasing the frequency of the oscillation provides for selective activation of clusters with stronger coupling.

4.4.2 Networks learn patterns of external input and reproduce the reverse

To investigate the basis of learning through synaptic plasticity in this model, I had networks encode a pattern of external input (a set of DC inputs with varied magnitude across the network) to connections (Fig 4.2). I monitored the phase at which neurons fired relative to the oscillations, as a function of their input magnitude. The simulations were split into five phases: prior to the input pattern (red in Fig 4.2B), during patterned input (yellow), after pattern learning has saturated (green), and two subsequent replay periods (replay periods one and two; with and without prior patterned DC input). During the period prior to the input pattern and the replay periods all neurons received the same moderate DC input and STDP was disabled. The first replay period shows the effect of learning the input pattern and the second shows the effect of playing the stored pattern back (i.e no input pattern is present) with active STDP.

The raster plots in Figure 4.2A show the evolution of firing phase across each period of the simulation. The color indicates the magnitude of input current a neuron

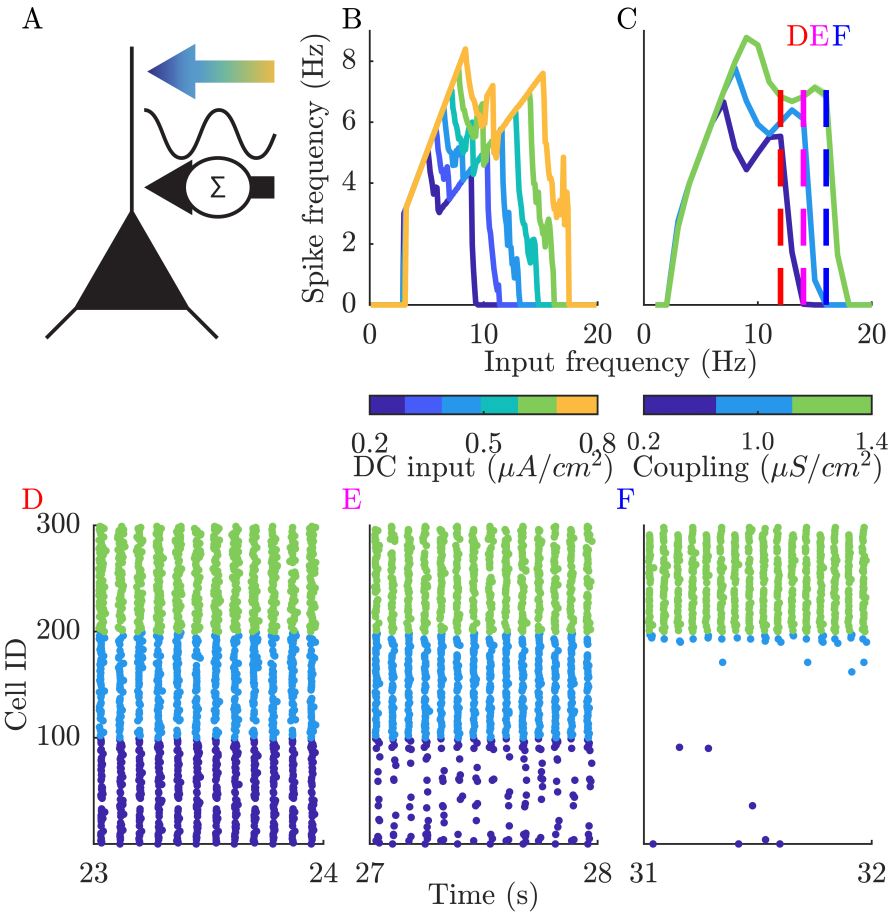

Figure 4.1: **Input-dependent resonance shift allows for selectively activating subsets of neurons.** (A) Model neurons receive 3 types of input. External input is DC which varies in magnitude with neuron identity, represented by the color mapped arrow. All neurons receive an identical oscillating input, represented by the sine wave. Additionally neurons receive the synaptic inputs from neighboring neurons according to network connectivity and synaptic weights. (B) The input-dependent resonance shift manifests as a broadening of the resonance curve with increasing excitation of the neurons. (C) Broadening of the resonance curve also occurs for changes in synaptic weights which provides for selective activation of subsets of neurons based on synaptic coupling. Dashed lines show the frequencies corresponding to the raster plots in panels D,E,F, which show the divergent activation for frequencies between 12 and 16 Hz. Error bars = ± s.e.m.

receives and neurons are sorted by this value with highly activated neurons having a higher input rank. Before any input, neurons fire randomly over a narrow band of phases (Fig 4.2A far left). The input pattern leads to organized firing with highly activated neurons firing at earlier phases (Fig 4.2A inner left),with the neurons receiving larger current firing earlier on the oscillatory cycle and neurons that receive smaller DC input following, with the range of firing phases being determined by the spread of activating input (Fig 4.10). This variable phase locking is a well-known phenomenon observed during synchronization of weakly-forced oscillators where there is a small detuning of mutual frequencies of the drive and the oscillator. For example, see [122]. The neurons in resonance behave as oscillators, and their specific frequency depends on the properties (height and width) of their resonance curve, which shape is in turn contingent on the magnitude of DC input (Fig 4.1B).

As the pattern is learned, the overall phase shifts, but neurons return to firing at a uniform phase, independent of their DC input (Fig 4.2A center). This convergence is due to the universal learning rule which mimics STDP [123], where the synapse is being strengthened (or weakened) when the presynaptic neuron fires within a narrow window before (or after) the postsynaptic neuron. As long as the neuronal pair fires in an ordered sequence, the corresponding synapse gets systematically potentiated or (weakened), leading to increased synaptic input to the neuron having lower DC input. When synaptic input offsets the difference in DC input between the two neurons, the neurons fire simultaneously - resulting in the termination of synaptic potentiation (depression). For this process to be effective, the time-length of the EPSP has to be on the order of $1/f$, where f is the oscillation frequency. For theta frequencies this constitute a time constant of 100-300 ms, roughly corresponding to activation time constant of NMDA receptors [124]. However, if the reactivation happens at higher

resonant frequencies, as shown in next section, this activation time constant can be significantly smaller.

When learning is suspended and the external input pattern is removed, and all neurons receive the same intermediate DC input, the network shows the reverse pattern of activation (Fig 4.2A inner right), as now the relative patterns of cellular input are dominated by synaptic currents. After a second period of learning (but with a uniform external input) the network returns to firing at a uniform phase, effectively erasing the stored pattern (Fig 4.2A far right). The above relationships are summarized in Figure 4.2B as we plot relative phase of neuronal spiking as a function of their DC input magnitude for each phase described above (red: before input pattern; gold: input pattern; green: after learning saturates, blue: replay of stored pattern; violet: replay after erasure). Figure 4.2C depicts the time-course of the evolution of firing phase for 11 neurons having different DC input values. The bars below indicate timeline when input and learning are present (white -input but no learning; black - learning and input, gray - no input and no learning).

The precise firing phase versus input relationship does dependent on total input to neurons being subthreshold; superthreshold input disrupts this relationship and impedes subsequent learning (Fig 4.11). One the other hand, the sign of the current in oscillatory drive does not affect the observed results. Namely, if an oscillation is purely hyperpolarizing the same pattern of phase organization is observed (Fig 4.12). The critical components to this learning and replay mechanism are resonance at the single neuron level and the presence of a subthreshold oscillation (Table 4.1). The LFP is a complex oscillation with a waveform that superimposes multiple frequencies. For example sharpe-wave ripples are composed of a high frequency ripple riding on top of lower frequency sharp wave [125]. We tested the robustness of this

input learning mechanism to a complicated waveform combining 6 Hz and 120 Hz oscillations (Fig 4.13A). The input versus phase relationship and pattern reversal after learning were both reproduced with this waveform.

4.4.3 Stored patterns can be replayed for any resonant frequency

To demonstrate the generality of the pattern storage and replay mechanism we introduce a second conductance based neuronal model based on classic Hodgkin-Huxley dynamics [1]. This model neuron displays spiking resonance in response to sub-threshold oscillating input in the gamma band between 40 and 90 Hz (Fig 4.14, which is well above the resonance band of the previous model. For ease the neuronal models will be referred to as Ks for the neuron which resonates in the theta band and HH for the gamma-resonating neuron. In Figure 4.3 we show that patterns stored during resonance at one frequency (theta band in our case) will be replayed at a higher frequency (gamma band) in a similar reverse firing order. Here, synaptic weights (and corresponding adjacency matrix) taken from a network of Ks neurons after a pattern was learned, are used to connect a network of HH neurons (after adjustment for differences in excitability, see Fig. 4.15). HH networks replay a pattern on a similar phase range as a Ks network, though with higher variability for late firing neurons. This result further indicates that the described resonance mechanism is very robust to frequency modulation that may occur, for example, during cycles between active behavior and rest.

4.4.4 Pattern learning saturates naturally in resonating networks

The results described above indicate that neuronal firing phases rapidly converge during learning, and that this process minimizes the firing phase difference between neurons. This behavior should result in two interesting phenomena: 1) synaptic

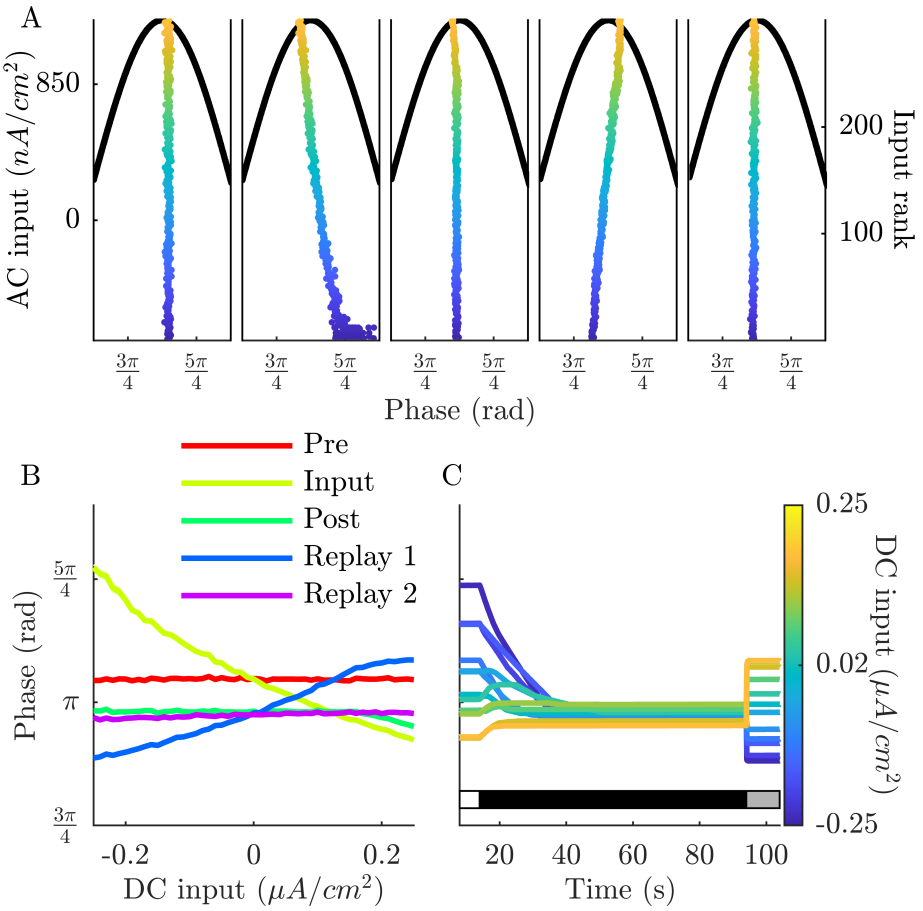

Figure 4.2: **Resonating networks learn by mapping input patterns to synaptic weights.** (A) Raster plots show the relationship between the phase of firing and the external input to the neuron. Black lines show the trace of the oscillating input and the color of the rasters shows the DC input to the given neuron. neurons are sorted by their input rank. Sub-panels in A correspond to before DC input distribution is applied (Pre), with DC input distribution (Input), after learning has saturated (Post), after learning/ no DC distribution (Replay 1), and after a second period of learning with no DC distribution (Replay 2). (B) The relationship between firing phase and DC input varies between negatively, positively, and not correlated for different epochs of the simulation. Data are averaged over 10 cycles of the oscillation. Error bars = ± s.e.m. (C) Transitioning from the input-pattern depending firing phases to synchronous firing is gradual. Lines trace the firing phase of 12 neurons with varying input magnitudes across time. The horizontal bars above indicate when the external input and learning are present (white -input but no learning; black - learning and input, gray - no input and no learning).

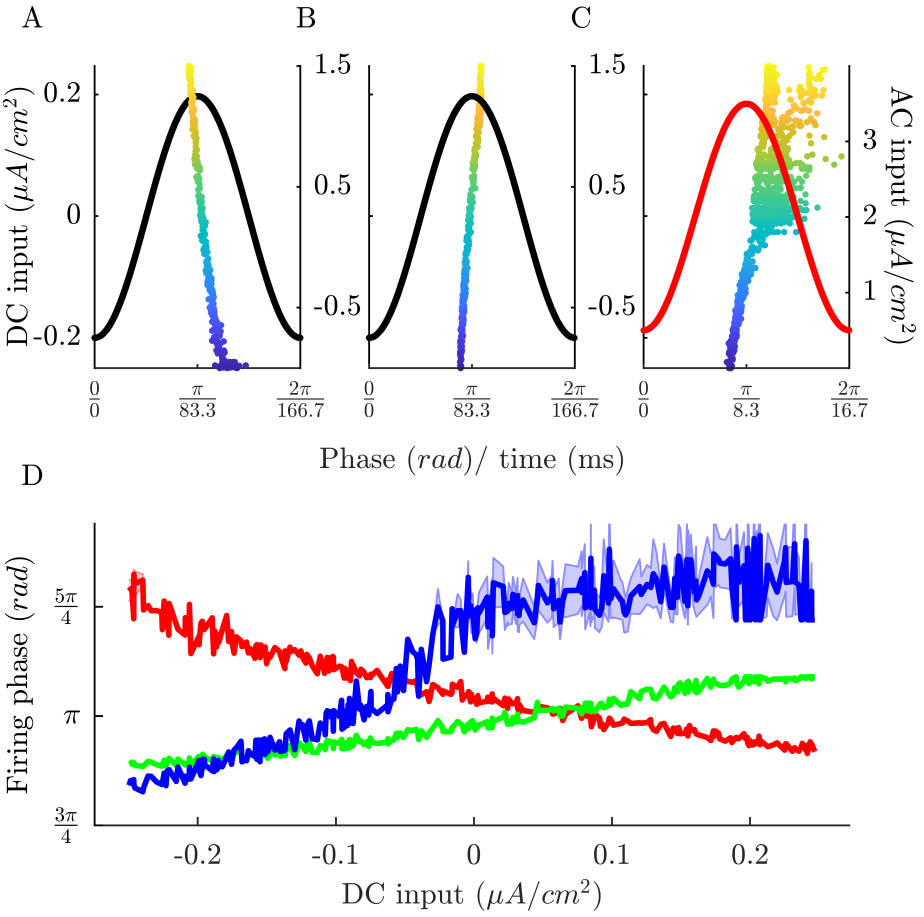

Figure 4.3: **Replay of stored pattern occurs independent of neuronal model and frequency band.** (A) Input induced pattern of firing phase for a network of Ks neurons driven with a 6 Hz oscillation. (B) Reversal of pattern during replay after learning for a network of Ks neurons driven by a 6 Hz oscillation. (C) Reversed pattern replayed by a network of HH neurons at 60 Hz. All raster plots include spike from 10 cycles of the oscillation and the color of a neuron's raster indicates the magnitude of DC input it gets in a pattern. (D) Firing phase versus DC input relations for the 3 above cases (red $\rightarrow$ Ks neuron before learning, green $\rightarrow$ Ks neuron replay, blue $\rightarrow$ HH neuron replay. Error bars = $\pm$ s.e.m.

strengths will stop changing when the phases converge, and 2) input differences between neurons will map onto their synaptic weights. To test these effects, we presented an input DC pattern to network for a long time-period and tracked the time course of synaptic change. If the learning rate (the magnitude of synaptic change corresponding to $\Delta t = 0$) allows, both the maximum (Fig 4.4A) and mean (Fig 4.4B) synaptic weight will saturate before the end of the simulation. Regardless of learning rate there is a large increase in synaptic change followed by a gradual decline to no change in synapse strength (Fig 4.4C). The time of peak synaptic change is delayed for slower learning rates. Note that the input pattern is the same for all conditions in Figure 4.4(A,B,C). Both the final mean synapse strength (Fig 4.4D black) and time it takes to saturate (Fig 4.4D red) depend on the range of currents in the external pattern. The time to saturation is the time it takes for the mean change in synaptic strength to fall permanently fall below $5 \times 10^{-6} \quad mS/cm^2$.

Saturation of learning occurs when the input pattern is fully mapped to the synaptic weights in the network, a phenomenon quantified in Figure 4.5. The mapping of the input pattern is reversed in the synaptic weights. Highly activated neurons, which fire at an earlier phase, strengthen outward connections (black trace) while weakening inputs (red trace). Neurons given lower external inputs do the opposite, strengthening inputs and weakening outputs. This leads to the external input pattern and the synaptic input pattern being complimentary, leading to all neurons receiving the same net input.

Overall, neurons with the lowest DC current within the input pattern strengthen inputs more than the rest of the network, while highly-activated neurons do the opposite. The new pattern of synaptic connectivity is complementary to the input pattern, which leads to all neurons firing at the same phase. Synchronous firing ter-

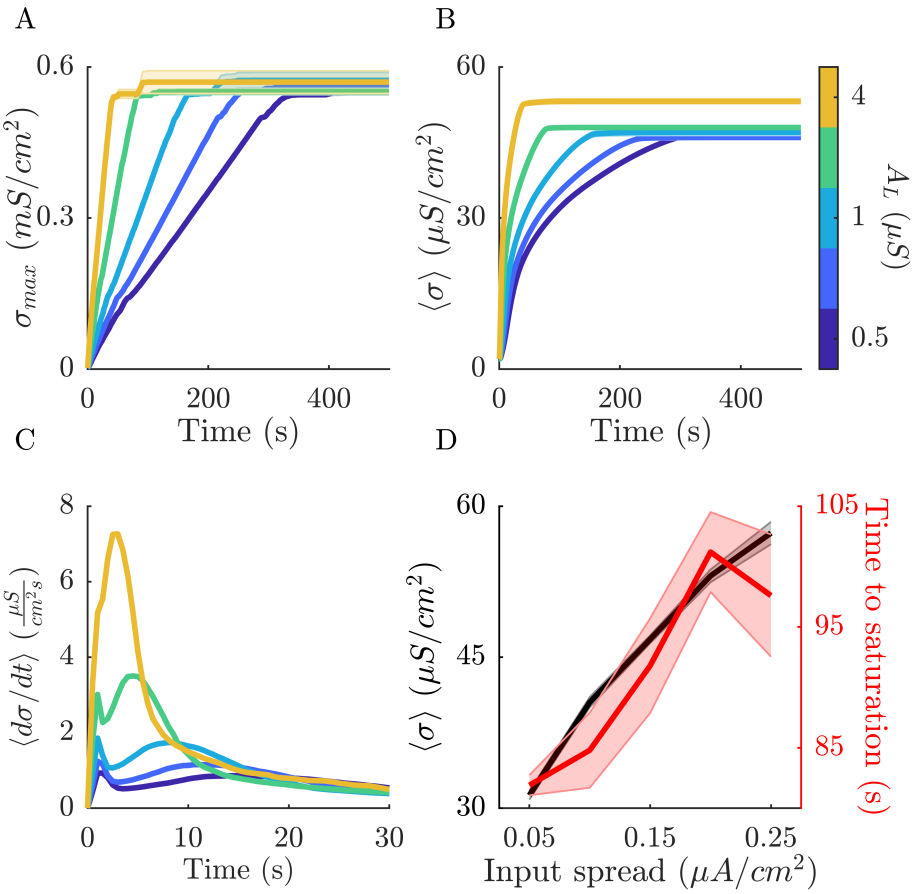

Figure 4.4: **Learning saturates naturally after input pattern is completely mapped to synapses.** Saturation of learning reliably occurs given that the learning rate is high enough for the given time. Both maximum (A) and mean (B) synaptic weight saturate. Line color indicates network learning rate. (C) The majority of synaptic change occurs early during the learning period then gradually decreases to zeros. (D) Final mean synapse strength and time until learning saturates depends on the spread of the input distribution. Error bars = ± s.e.m.

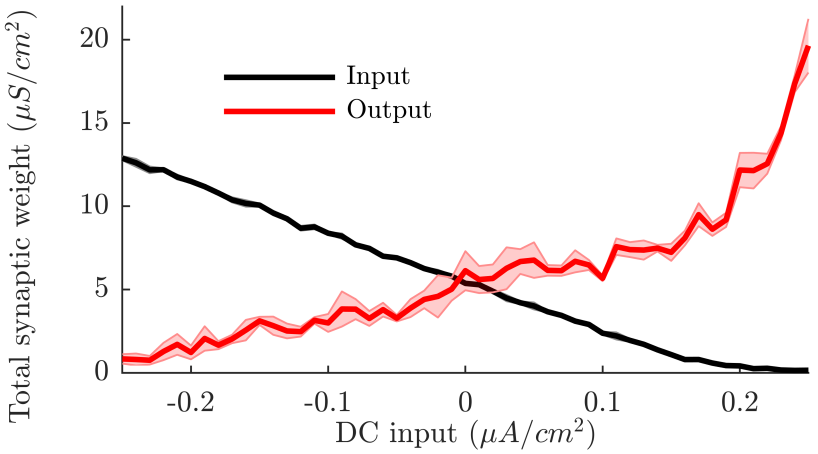

Figure 4.5: **Input pattern maps to both synaptic inputs and outputs.** After learning, input strength (black) is anti-correlated with input magnitude of a neuron in the pattern and output strength (red) is correlated. Error bars = ± s.e.m.

minates learning, because as spike-time differences between neurons approach zero, there is no net synaptic change (simplified in our model as zero synaptic change for $\Delta t < 1.5$ ms). When the external input is removed, the complementary synaptic input distribution lead to a reversal in firing order from the input pattern (see Figure 4.2A in previous section).

4.4.5 Resonance with subthreshold oscillations facilitates sequence learning and replay

Next I investigated whether we can use the observed resonance shifts to store sequential neuronal activation to model the phenomenon of sequential replay following experience [110]. Sequences were generated by delivering a slowly varying current to sequentially activate subsets of neurons (Fig 4.6A; solid lines), with each group resonating with the oscillating current in turn. This current is to model the preferential activation of subpopulations of place cells as an animal traverses a series of spatial locations. The asymmetry in its shape is to model the forward approach of the animal to a given location. It also provides temporal input relationships between neurons, to strengthen connections between neurons activated in a prior location and

those activated in the current location. During the course of sequence presentation, groups of neurons display dynamic phase relationships (Fig 4.6B & C), where neurons that are highly activated fire earlier. For a single group, during the rising phase of activation, the firing phase will move earlier for each cycle of the oscillation (i.e. firing phase precession is observed). Between groups, those which are at peak activation will fire at earlier phases than less-activated groups. These phenomena result from the relationship between activation and firing phase (Fig 4.6D) and the result of the input dependent resonance shift (Fig 4.1A). The activation sequences were presented to the network 10 times, during which synapses were allowed to evolve using the same STDP-based learning rule as before.

After this learning phase, the sequence can be reproduced in both the forward (Fig 4.7B) and reverse directions (Fig 4.7A). Both types of replay occur under different dynamical conditions. Reverse replay occurs when the whole network is depolarized to resonate with the oscillating input, but all neurons are activated to the same extent (i.e., each neuron receives the same D.C. input). This is due to the fact that neuronal groups in the end of the sequence receive larger overall input than groups activated at the beginning due to asymmetry in connection strengths. This results in an earlier phase of activation when the network resonates with the oscillatory current. In contrast, forward sequential replay occurs when the network is driven by external noise, in the absence of an oscillation. The neurons which fire early in the sequence subsequently depolarize neurons at the adjacent location, making them more prone to fire. Summary data is shown in Figure 4.7C for reverse replay firing phase among the 5 groups. During reverse replay, groups activated earlier in the sequence reliably fire at a later phase of the oscillation (red trace). Without any learning (i.e., without STDP), groups generally fire at the same phase of the oscillation (black trace).

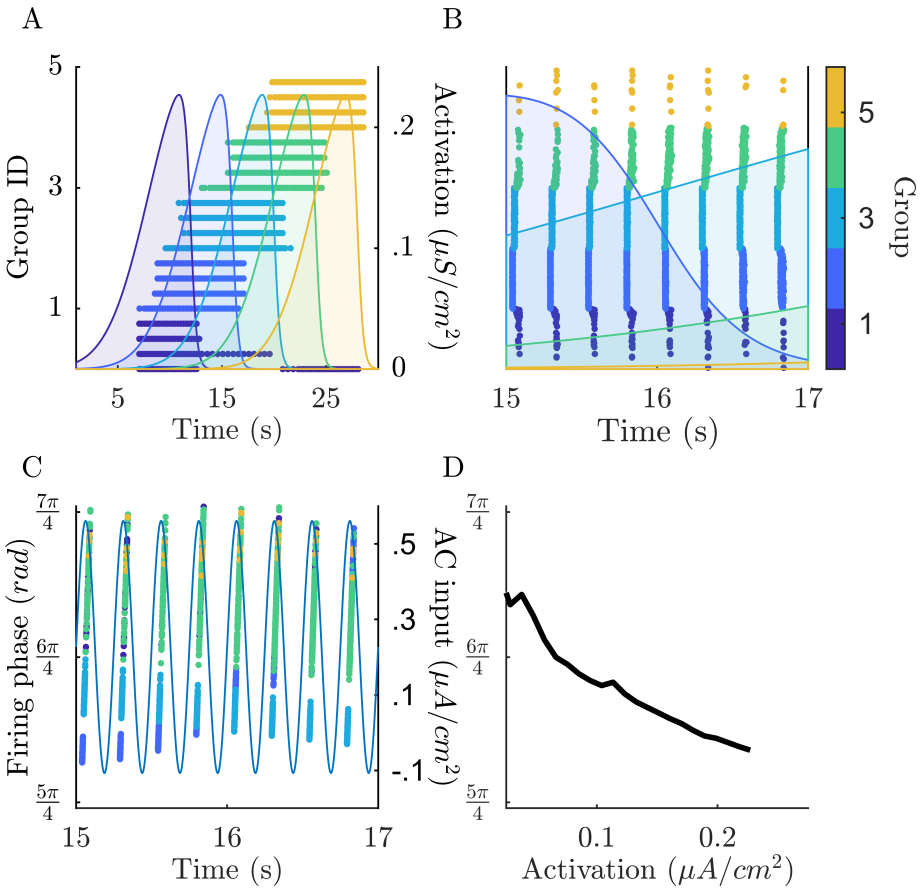

Figure 4.6: **Sequential activation of network subgroups leads to phase precession though time.** (A) Networks were sequentially activated by a slowly varying depolarizing current delivered to subsets of neurons (solid lines; color indicates group). Spiking activity of each group is represented by the raster plots of different colors. Neurons are sorted on the y-axis based on their lattice location, such that neurons closer on the y-axis are more likely to be connected. (B & C) At the transition between the activation of two groups phase order changes so that the neurons receiving the highest activation always fire at an earlier phase, leading to a phase precession though time. This is shown in relation to the (B) activation of the groups and (C) with reference to the oscillation. (D) The activation versus phase relationship shows that neurons fire earlier and with less variability with more depolarizing input. Error bars = ± s.e.m.

During forward replay, the feed-forwardness of the intergroup connections dominate. The original firing order of the groups is reproduced, and early groups fire before late groups (Fig 4.7D; red trace).

Sequential learning leads to connections being strengthened in the same direction of the sequence (feedforward) and weakens connections in the reverse (feedback). Mean synaptic weights between groups show strengthened connections in the direction of the sequence and weakened connections in reverse (Fig 4.7E). This is quantified for the entire network by the direction index which is

$$\sum_{i=0}^{G-1} w_{i,i+1} - w_{i+1,i} / \sum_{i=0}^{G-1} w_{i,i+1} + w_{i+1,i}, \tag{4.6}$$

where $w_{i,i+1}$, is the mean synaptic weight of connections between groups (Fig 4.7F). Critically, the feed-forwardness of the connections varies between groups, and increases with every sequence presentation.

4.4.6 Functional network structure emerges in the theta band

I next sought to compare the behavior of simulated networks with experimentally observed pattern formation in the in vivo networks. Information representation and subsequent encoding using STDP type learning rules, require stable spike time relationships. In the model resonance with periodic input leads to stable spike-timing phase relationships. To quantify this effect I measure functional network connectivity and stability of the observed functional relationships using metrics that were developed and validated [126] and compare it to results of the same analysis on experimental data.

In networks driven by oscillatory input (a 0.3 $\mu A/cm^2$ amplitude sine wave with a 0.3 $\mu A/cm^2$ DC offset) and background noise, oscillatory input leads to highly organized functional network structure between 4 - 10 Hz (Fig 4.8). I quantified

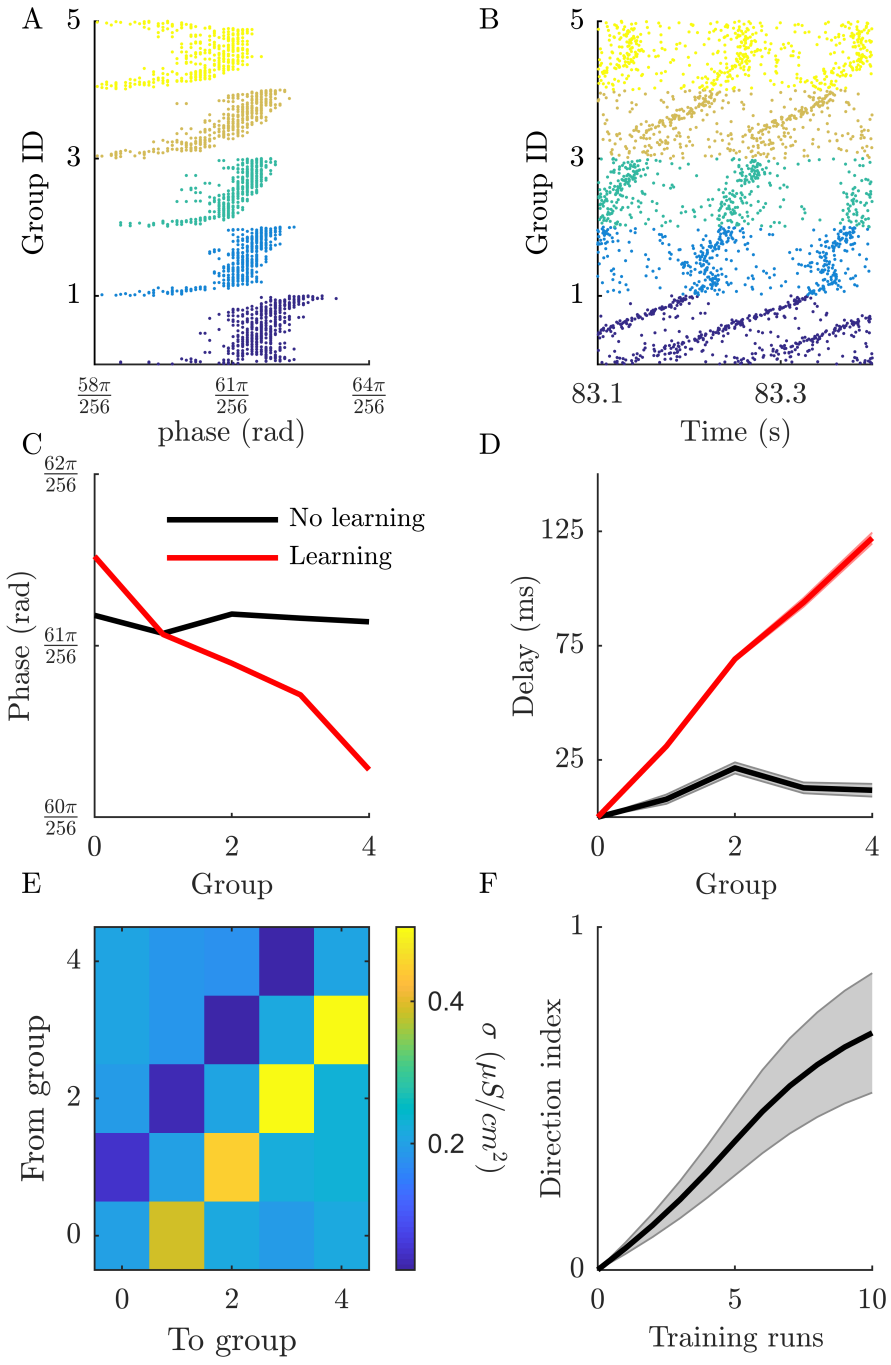

Figure 4.7: **Learned sequences can be replayed in both the forward and reverse directions.** After a sequence is learned, (A) reverse replay occurs when a network is driven by an oscillation and (B) forward when the network is driven by noise. Raster plots follow the same organization as Figure 4.6. (C & D) The firing relationships between between groups is stable across cycles and different from groups without learning. (E) Synaptic connections between groups encode the sequence direction between groups, while weakening the reverse direction. (F) The directionality of intergroup connections emerges gradually after repeated sequence presentations, with increasing variations between groups. Error bars = ± s.e.m.

functional connectivity in three ways: spike-LFP coherence, mean Average Minimum Difference (AMD) z-score, and functional network stability [126]. Spike-LFP coherence, which represents the reliability of the time of spikes within the LFP oscillation across the entire network, shows a noise dependent resonance effect for stimulation between 3 and 13 Hz (Fig 4.8A). AMD z-score and functional network stability are related measures that are based on the pairwise relationships between spike times of neurons across the network. The average significance (z-score) of AMD measures between neurons shows a narrow resonance effect between 4 and 10 Hz with a peak effect at 6 Hz which depends on the level of background noise (Fig 4.8B). Functional network stability, which captures how similar AMD z-scores are across time and reports the stability of spike-time relationships across pairs of neurons, displays a similarly narrow resonance effect between 4 - 10 Hz, but maintains a near maximal value throughout this band (Fig 4.8C). I compare these results to the ones obtained during optogenetic stimulation in vivo hippocampal networks [120]. Rhythmic stimulation of parvalbumin-expressing (PV+) interneurons in PV::ChR2 transgenic mice was used to ensure that principle cells within the network were received subthreshold periodic inhibitory stimulation. Rhythmic optogenetic stimulation of PV+ interneurons leads to significant increases in both spike-LFP coherence and functional network stability for frequencies between 4-10 Hz among the principle cells within the network (Fig 4.8D). This suggests that in vivo CA1 hippocampal network stably organizes its firing activity within resonant frequency band of principal cells, while such organization is not observed when oscillatory drive is outside of this range.

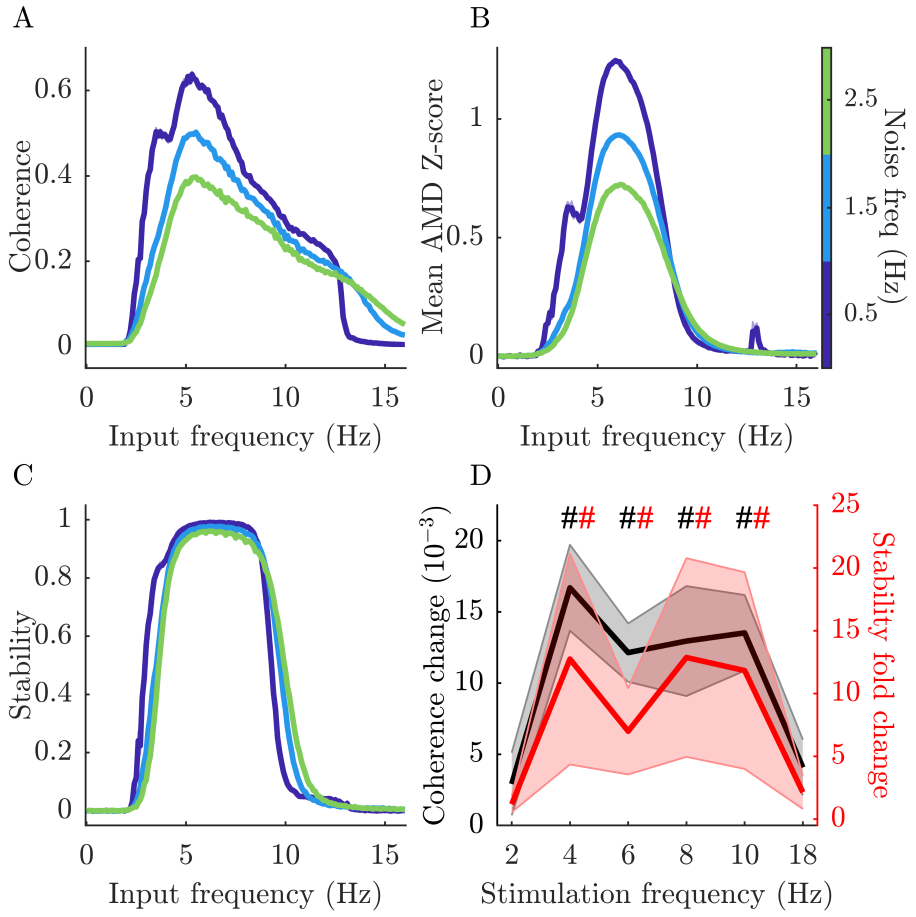

Figure 4.8: **Resonating networks have organized functional structure over a narrow frequency band.** Theta band resonance leads to highly organized functional network structure. In simulated networks spike-LFP coherence (A), mean AMD z-score (B), and functional network stability (C) all dramatically increase between 4-10 Hz. This effect is robust to noise, which is indicate by line color. (D) In vivo optogenetic stimulation of hippocampal PV+ neurons lead to similar increases in spike-LFP coherence and functional network stability at these frequencies. Error bars = ± s.e.m.

4.5 Discussion

I demonstrated in a biophysical model that shifting resonances facilitate learning of static and sequential patterns in neural networks. Our model combines subthreshold activation of neurons by stable and oscillating currents which leads to firing in a narrow frequency band. The firing rate resonance of this model neurons displays an input dependent broadening which allows for selective activation of subsets of neurons within a network. The resonance effect also leads to detailed mapping of a firing phase versus input relationship beneficial for the encoding of patterns into synaptic weights, and for the autonomous termination of learning. The resonant effect at the single neuron level leads to the emergence of highly organized spike-time relationships at the theta band which was also shown in vivo experiments.

The input-dependent broadening of the resonance curve in firing rate (Fig 4.1) allows for selective activation of subsets of neurons within a network with increasing input frequency as has been demonstrated in other computational models indicating this is a general property of neural networks with resonance [119]. This provides a mechanism for networks to change representations by shifting the pattern of input strengths, or alternatively, by modulation of the oscillatory input frequency. Such a mechanism would operate similarly for both externally generated (i.e. sensory input) and internal (i.e. stored representations within synapses) inputs.

The mechanism described here can simultaneously promote both forward and reverse replay of recently-learned sequences in neural networks, consistent with prior reports of replayed patterns in both directions, across even short intervals of in vivo recording [127]. The reverse firing phase relationship and learning saturation seen in our external pattern simulations together provide a plausible mechanism for

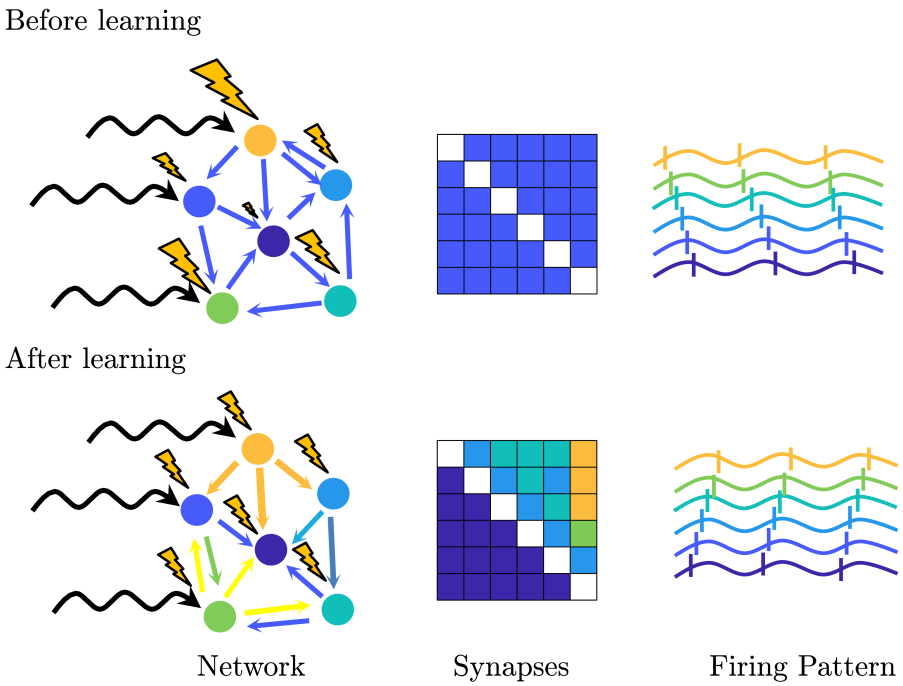

Figure 4.9: **The model proposes a mechanism for the generation of reverse replay.** Reverse replay due to how an input pattern imposes a phase procession of neuron firing due with respect to the oscillation. As the network learns the pattern inputs to weakly excited neurons are strengthened while those to highly excited neurons are weakened. When the pattern is removed inputs from synaptic connections dominate and the reverse mapping of synaptic weights leads to reverse reactivation.

the generation of reverse replay events in vivo (Fig 4.9). This mechanism relies on the fact that neurons with high input fire at early phases of oscillatory drive when in resonance. Before any synaptic change occurs, the firing phase is governed by the distribution of the external inputs the neurons receive. As learning progresses, neurons with the lowest external input strengthen their synaptic inputs more than the rest of the population, while highly activated neurons do the opposite, as shown in Figure 4.5. The emerging pattern of synaptic connectivity is complementary to the input pattern, which leads to all neurons firing at the same phase (i.e., in synchrony). Synchronous firing leads to no net synaptic change and thus terminates learning. As the complimentary input pattern is now represented within synaptic weights, in the absence of external input, neurons fire in the reverse order.

The mechanism for the replay of the reversed pattern is not dependent on the encoding frequency. Figure 4.3 shows that a pattern can be encoded in one frequency band (6 Hz) and replayed at another (60 Hz), provided the neurons within the network can resonate at both frequencies. Such a mechanism could explain why sequential place cell activation during exploration (usually in the context of theta oscillations) can lead to subsequent replay events occurring in the context of higher-frequency oscillations, such a sharp-wave ripples [115]. Here I use separate models to generate spiking responses to inputs of varying frequencies, but a neuron with resonances in both bands would behave in a similar manner. The importance of this frequency generality is that the encoding and replay of patterns in neural firing often occur when different frequencies are dominating the LFP. For example, sequences of place cell activation, an any synaptic encoding, occur when theta is the most dominant frequency band in the LFP, but instances of replay occur during sharp-wave ripples where gamma (40-100 Hz) is most prominent [110, 115].

Learning through STDP requires either saturation or compensatory plasticity mechanisms to counteract the inherent positive feedback effects on firing rate, leading to network instability. Previous implementations of STDP have employed boundaries on synaptic weights, dynamic asymmetries between potentiation and depression, or renormalization of synaptic weights to preserve firing rates (reviewed in [128]). This model proposes an alternative mode for preventing instability (Fig 4.4). As the input pattern is encoded into synaptic weights and the firing phase distribution becomes more uniform, changes in synaptic weights decrease and stop due to features of the STDP curve around $\Delta t = 0$, which is a reasonable fit to experimental data [123]. While many plasticity mechanisms exist both at the cellular and network level, the current mechanism provides an elegant solution to the question of when

neural networks terminate learning of input patterns.

I have shown experimentally that predictions of this model agree with observed, network wide pattern formation in hippocampal networks when channelrhodopsin-expressing PV+ interneurons are rhythmically stimulated [120]. Within the hippocampus, functional network structure emerges and stabilizes during stimulation in the theta band (4-10 Hz), but not outside of it. Using several methods of measuring functional connectivity within networks, I found a robust resonance effect in the formation of stable network structure (Fig 4.8). This effect is due to the organizing the firing of the network around the phase of the oscillatory input. The fact that this effect is reproducible in various neuronal models [118] and also in vivo suggests that it may be a general feature of activity is organized in neural networks, to optimize encoding of input patterns.

The input-dependent organization of network activity facilitated by resonance provides a network-level substrate for sequential learning (Figs 4.6 & 4.7). When subsets of neurons have overlapping activation curves the relationship between input and firing phase creates spike-time differences that are optimized for encoding the sequence order. One requirement for this result is that the activation of neurons needs to be skewed in time - in other words, repolarization occurs more rapidly than depolarization (Fig 4.6A). This ensures that connections strengthened by a balanced STDP regime are feedforward with respect to the sequence order, while feedback connections are weakened. Within the context of hippocampal place cells sequences, there is some evidence for this required skewness in activation [103, 129], though in an experience dependent manner [130]. Replay is the most direct readout of sequential learning. In the hippocampus, replay of place cell sequences occur both in the forward and reverse direction [114, 103, 115, 117]. These replay modes are

represented in different proportions across behavioral states, with forward replay being more prevalent during sleep [131, 117]. In our model, forward replay occurs when a network is driven by noise (i.e. randomly activated) and reverse occurs when the network is reactivated by oscillating input (Fig 4.7C-F).

Hippocampal place cells show a theta phase precession in their firing, as an animal approaches a location neurons which code for a near-by place will fire in the troughs of the theta oscillation while those which code for a far place fire near the peak [11]. This phenomenon has also been shown in the entorhinal cortex [112] and in the ventral striatum [113]. In this model neurons in resonance with an oscillating rhythm they show a similar firing versus phase relationship.

Beyond the context of place cells, this model demonstrates how a network can translate information between the two main modes of neural coding rate [2] and phase [7, 8, 9, 10] coding. Both rate coding, where stimuli are represented by the firing rate of neurons, and phase coding, where information is represented in the time differences between spikes, are observed in nervous systems. Rate coding is simple and reliable, however, it is limited in its capacity for dynamic pattern separation [5]. These results provide a mechanism for the translation between these two coding schemes, and allows for networks to switch through neuromodulation [119]. Whether the mechanism described here mediates information encoding in the brain remains an open question. However, our present data suggest that such a mechanism has explanatory value for many of the observed in vivo phenomena surrounding learning.

4.6 Supporting Information

4.6.1 The phase width of the pattern is determined by the range of inputs

When networks are in resonance with the oscillatory drive, there is a dispersion of firing phases as differing external input is delivered to neurons across the network.

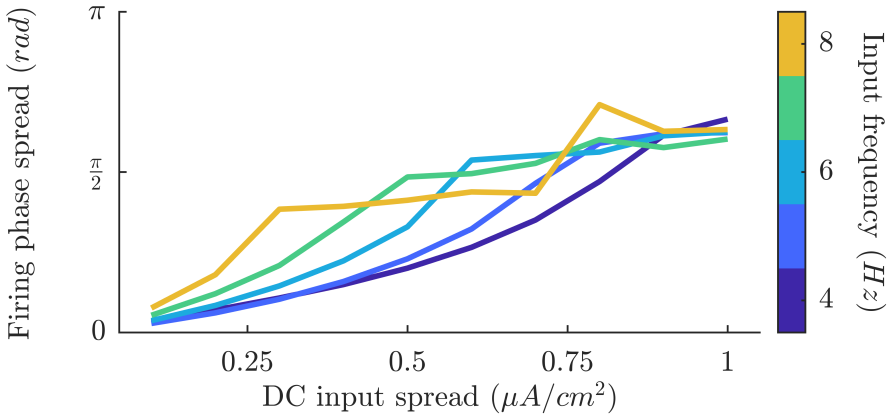

Figure 4.10: **Dispersion of firing phase is dependent on the spread of depolarizing input.**

The depolarization dependent broadening of the resonance curve (Fig 4.1B) is responsible for this phase relationship and the range of phases that the neurons in the network fire depends of the range of DC input distribution (Fig 4.10). I performed simulations to measure the dependence of the phase range on the input range. These simulations were performed without learning ($A_{learn} = 0$) and for a disconnected network ($\sigma_{i,j} = 0$ for all i, j). To maintain a subthreshold regime the minimum boundary for the DC distribution was adjusted so that the maximum input to any cell was never greater than 1.3 $\mu A/cm^2$. Oscillations were 0.4 $\mu A/cm^2$ in amplitude and had frequencies ranging between 4 and 8 Hz. Phases for each neuron were averaged over 10s.

4.6.2 Superthreshold input disrupts firing phase relationship and pattern storage

To establish that neuronal resonance (in response to subthreshold input) is critical for formation of the observed phase relationships, I performed analogous simulation to that shown in Figure 4.2 but for superthreshold input. Superthreshold input disrupts the relationship between depolarization and phase that was seen in response to subthreshold input (Fig 4.11A). When the relationship between depolarization

and the phase is no longer reliable the network is not able to map the input pattern to the synapses, and replay of the reverse pattern is not observed (Fig 4.11B). Superthreshold data was obtained using a 6 Hz, 0.2 $\mu A/cm^2$ amplitude oscillate and DC inputs ranging from 1.3 to 1.8 $\mu A/cm^2$.

To further clarify this point I investigated network response to combinations of 3 parameters: input type (i.e. sub vs superthreshold), presence of oscillatory drive and cell resonant properties (Table 4.1). The resonant properties of the Ks model depend on the parameter g_{Ks} and for the input coding mechanism described here, net input to the neuron must be subthreshold (i.e. the peak input magnitude would not elicit spiking if applied as direct current). As shown in Figure 4.2, a spiking pattern induced by external input to the network is reversed when replayed from synaptic weights, leading to a negative correlation between the firing phase of a neuron in the input pattern and its firing phase during replay ($r_{phase} < 0$). As summarized in Table 4.1, the only condition in the model that will successfully yield a pattern reversal is subthreshold oscillatory input with a $g_{Ks} = 1.5 \quad mS/cm^2$. Regardless of g_{Ks} superthreshold input does not yield a pattern reversal and only leads to phase locking with the oscillatory drive when g_{Ks} is high . $f_{pattern}$ reports the average firing rate of the network before learning, but with an external input pattern. Subthreshold input does not elicit network activity when $g_{Ks} = 0 \quad mS/cm^2$, but only with a oscillatory drive for $g_{Ks} = 1.5 \quad mS/cm^2$. Note that because of the the form of the oscillation, $Acos(2\pi f_{osc}t/1000)$, when f_{osc} is set to zero all neurons receive the same maximal input as though there was an oscillation present. All simulations were performed under the same conditions as for the data in Figure 4.2 with 0.3 $\mu A/cm^2$ oscillation and ranges of DC inputs as listed in Table 4.1. The variation in DC currents is necessitated by changes in input resistance and threshold as g_{Ks} changes.

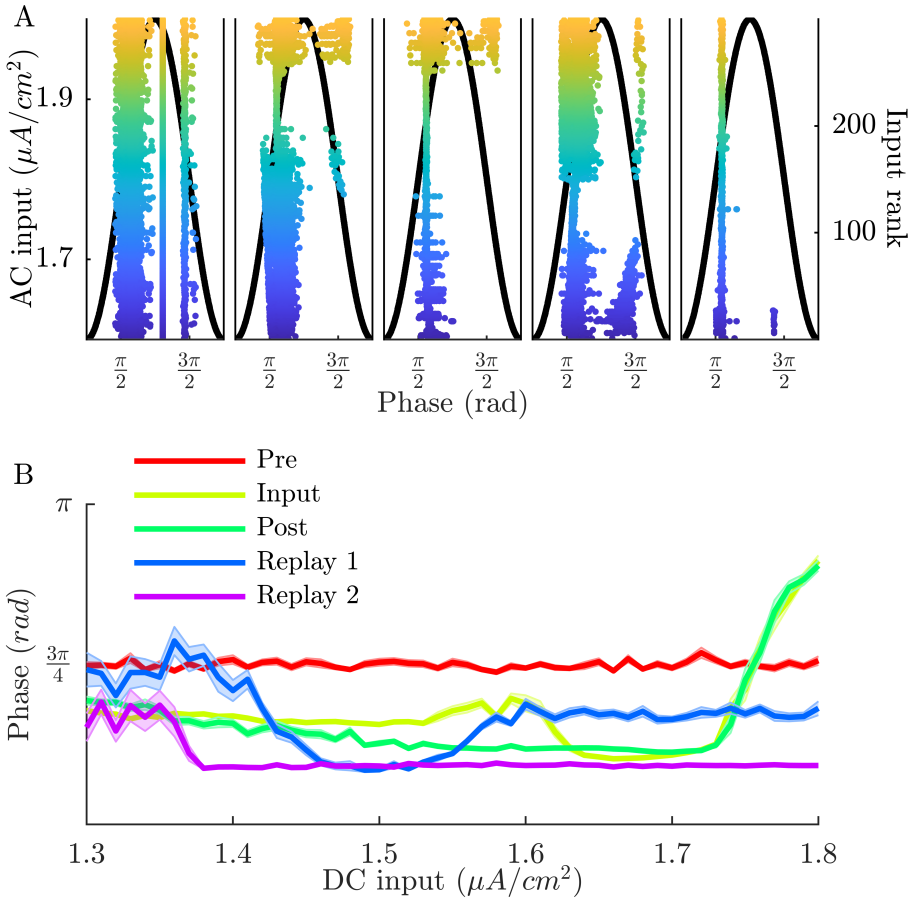

Figure 4.11: **Superthreshold input disrupts firing phase versus input relationship.** (A) Raster plots of the relationship between the phase of firing and the external input to the neuron. Black lines mark the trace of the oscillating input and the color of the rasters shows the DC input to the given cell. Cells are sorted by their input rank. Subpanels in A depict (from the left) neuronal activity: before DC input distribution is applied (Pre), with DC input distribution (Input), after learning has saturated (Post), after learning/ no DC distribution (Replay 1), and after a second period of learning with no DC distribution (Replay 2). (B) The relationship between firing phase and DC input varies but is not correlated for different epochs of the simulation.

Table 4.1: **Learning depends on neuronal resonance and subthreshold input.** Variation of $g_{K}s$, input level, and the presence of an oscillation shows that spiking resonance in response to subthreshold input is critical for proper pattern encoding.

g_{Ks} (mS/cm^2)	Oscillation (Y/N)	Super/ Sub (↑/ ↓)	DC range ($\mu A/cm^2$)	r_{phase} ($\pm s.e.m.$)	$f_{pattern}$, Hz ($\pm s.e.m.$)
1.5	Y	↑	[1.50,1.65]	-0.16 ±0.03	6.52 ±0.03
1.5	N	↑	[1.50, 1.65]	-0.02 ±0.02	12.02 ±0.01
1.5	Y	↓	[0.60, 0.75]	-0.93 $\pm 2.4 \times 10^{-3}$	6.0 ± 0.0
1.5	N	↓	[0.60, 0.75]	N/A	0.0 ± 0.0
0.0	Y	↑	[-0.15, 0.00]	-8.1×10^{-3} ±0.03	13.86 ± 0.10
0.0	N	↑	[-0.15, 0.00]	0.04 ± 0.03	35.61 ± 0.07
0.0	Y	↓	[-0.60, -0.45]	N/A	0.0 ± 0.0
0.0	N	↓	[-0.60, -0.45]	N/A	0.0 ± 0.0

4.6.3 Hyperpolarizing or complex oscillations induce resonance and support pattern learning

To show that periodic stimulation can induce resonant behavior regardless of whether its depolarizing or hyperpolarizing we performed a simulation where a network mapped and replayed an input pattern (similar to the simulation in Figure 4.2), but with an oscillation of the form $A_{osc}(cos(2\pi f_{osc}t) - 1)$. This ensured that the oscillation was always hyperpolarizing. With this oscillatory drive, the network was able to produce a stable phase versus input relationship, store, and replay an input pattern in a similar manner to the normal oscillation (Fig 4.12). The oscillation used here had a frequency of 6 Hz and amplitude of 0.35 $\mu A/cm^2$. The DC inputs ranged between 0.6 and 0.85 $\mu A/cm^2$.

The LFP is a complex waveform containing oscillations across a wide band of frequencies. To test how robust this learning mechanism is to complex oscillatory input I delivered an oscillation of the form $A_{osc,1}cos(2\pi f_{osc,1}t)^2 cos(2\pi f_{osc,2}t) + A_{osc,2}cos(2\pi f_{osc,3}t)$. $A_{osc,1}$ and $A_{osc,2}$ were set to 0.25 and 1 $\mu A/cm^2$ respectively and the frequencies were $f_{osc,1} = 3$, $f_{osc,2} = 120$, and $f_{osc,3} = 6$ Hz. This oscillation yielded a 6 Hz fundamental frequency with a faster 120 Hz oscillation on the peaks (Fig 4.13A). Resonance induced by this oscillation still enabled mapping of the input

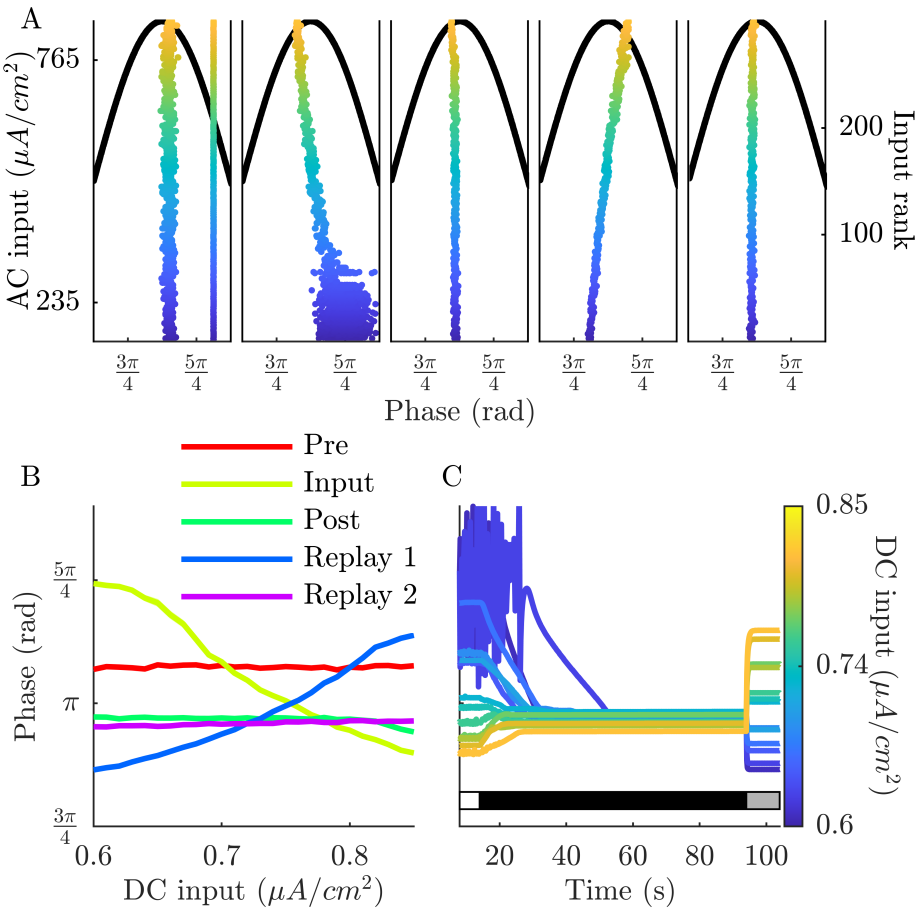

Figure 4.12: **Resonance and phase mapping mechanism can be induced by hyperpolarizing oscillations.** (A) Raster plots show the relationship between the phase of firing and the external input to the neuron. Black lines depict the trace of the oscillating input and the color of the rasters mark the DC input value to the given cell. Cells are sorted by their input rank. Sub-panels in A correspond to the Pre, Input, Post, Replay 1, Replay 2 periods. (B) The relationship between firing phase and DC input varies between negatively, positively, and not correlated for different epochs of the simulation. (C) Transitioning from the input-pattern dependent firing phases to synchronous firing is gradual. Lines trace the firing phase of 12 neurons with varying input magnitudes across time. The horizontal bars above indicate when the external input and learning are present (white -input but no learning; black - learning and input, gray - no input and no learning).

pattern to the synaptic weights leading the the replay of the reversed pattern (Fig 4.13B & C). DC inputs for these simulations ranged between -0.25 and 0.25 $\mu A/cm^2$

4.6.4 Gamma band resonance in the Hodgkin-Huxley model

To show that the mechanism of pattern storage and replay does not depend on the oscillatory drive frequency with which the pattern was encoded, I used the HH model which is resonance in the gamma (40-90 Hz) band. Figure 4.14 shows the spiking resonance curves for a HH neuron receiving a 1.5 $\mu A/cm^2$ oscillation of varying frequencies.

Synaptic weights encoding a pattern in the Ks model at 6 Hz were replayed at 60 Hz using the HH model (Fig 4.3). Due to differences in the input resistance and excitability between the two models a synaptic multiple, M_{syn}, parameter was used to scale all synaptic conductances in the network. Figure 4.15 shows that the relationship between the DC input a neuron received while encoding and its firing phase during replay is reproduced for M_{syn} between 10 and 30.

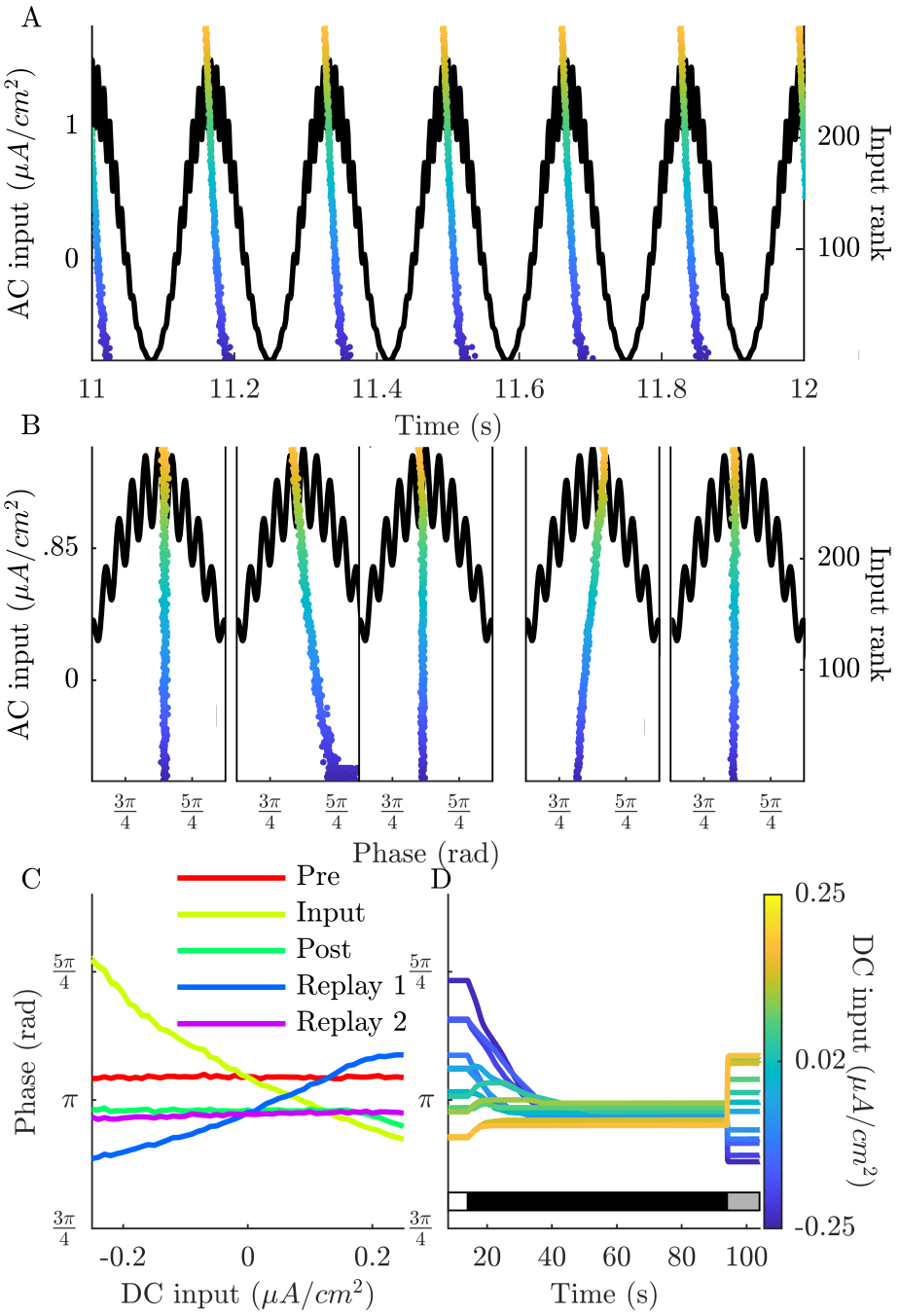

Figure 4.13: **Resonance and phase mapping mechanism are robust to oscillations with complex waveforms.** (A & B) A complex sinusoid composed of 3 Hz, 6 Hz, and 120 Hz oscillations was delivered to the network and induced cyclic firing. The phase order of the cells is determined by their DC input level (shown by color and position on the y-axis). Sub-panels in B correspond to the Pre, Input, Post, Replay 1, Replay 2 periods. (C) The relationship between firing phase and DC input varies between negatively, positively, and not correlated for different epochs of the simulation. (D) Transitioning from the input-pattern dependent firing phases to synchronous firing is gradual. Lines trace the firing phase of 12 neurons with varying input magnitudes across time. The horizontal bars above indicate when the external input and learning are present (white -input but no learning; black - learning and input, gray - no input and no learning).

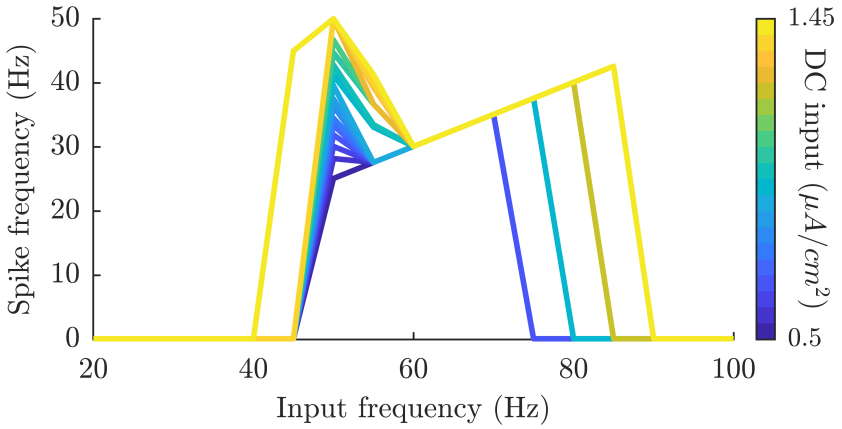

Figure 4.14: **The Hodgkin-Huxley model shows spiking resonance in the gamma range.** The broadness of the resonance curve is modulated by depolarizing input.

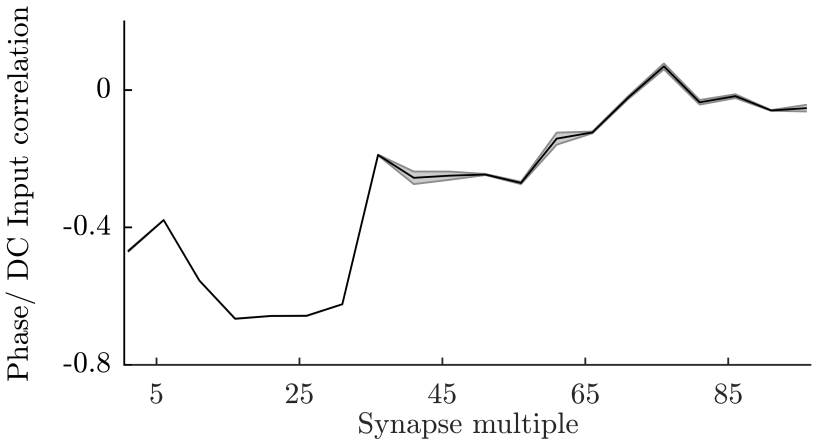

Figure 4.15: **Range synaptic multiples for transferring stored information between HH and Ks models.** Resonance-induced phase versus input relationship is stable over a range of synaptic multiples, M_{syn}, in the HH model.

CHAPTER V

Conclusion

5.1 Summary

Chapters II and III set up a three state model of network dynamics and information representation across the range of Acetylcholine (ACh) (Fig 5.1). Between the highest levels of ACh and moderate levels is a transition between stationary and moving dynamics (Fig 2.5), while synchrony emerges for very low levels of ACh (Fig 2.4). Similarly, destabilization of weak memories occurs as ACh is reduced to moderate levels and destabilization of all memories occurs for the lowest ACh levels (Fig 3.2).

Figure 5.1 lays out these three states and the dynamical predictions the model yields. High ACh (low $\bar{g}_{Ks}$/ waking) produces stable spatially localized firing in the network. Firing within this bump is asynchronous and at a high rate. In this state the location of the bump is highly sensitive to attractors formed by enhanced recurrent excitation as well as external input. This state is likely optimized for forming and strengthening new attractors from external input. Moderate ACh (moderate $\bar{g}_{Ks}$/ Rapid Eye Movement (REM)) the bump location is varied, either forming slow periodic waves or drifting between attractors. In this state only strong attractors are stable for an extended time. At the lowest extreme of ACh levels (high $\bar{g}_{Ks}$/

Non-REM (NREM)) periodic traveling waves of firing characterize the dynamics. In this state there is a high degree of spike synchrony within the bump and no stored memories are stable.

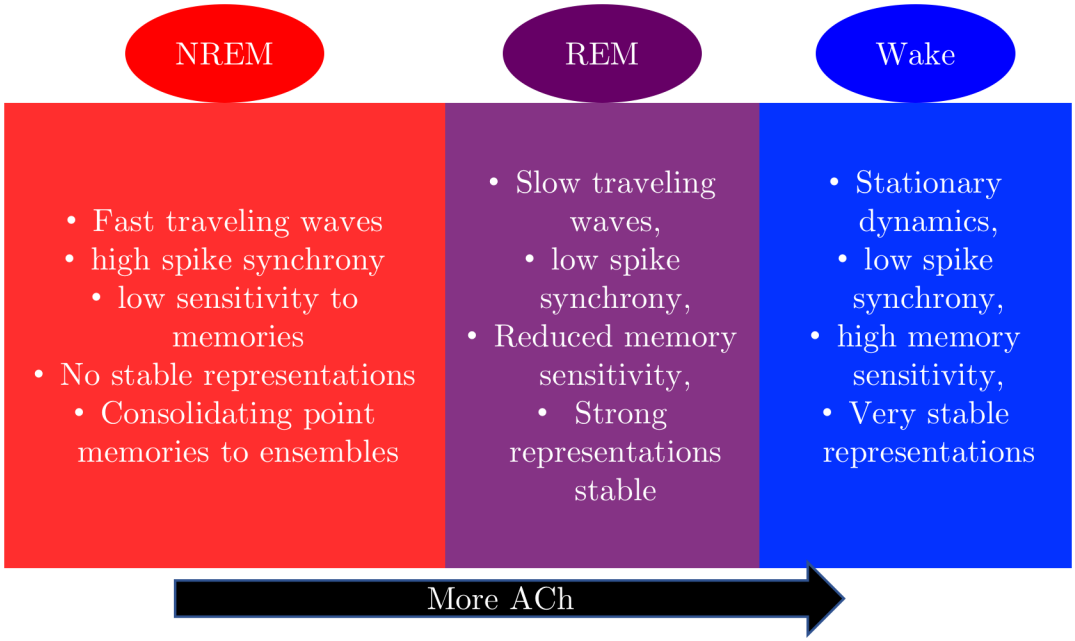

Figure 5.1: **Three functional states resulting from cholinergic modulation.** Summary of ACh modulation results. The model parameter, $\bar{g}_{Ks}$, is inversely proportional to ACh. Dynamical predictions derived from the model are mapped to the behavioral states NREM, REM, and Wake.

In Chapter IV the resonating quality of neurons in the low ACh condition was highlighted as the physical property that allows for proper encoding of an external input pattern and storage of that pattern within the synaptic weights of the network. When a pattern of depolarizing input is applied to the networks, with a subthreshold oscillation, neurons with the highest input fire at earliest phases of the oscillation and the remainder of the network arranges firing phase by input magnitude. This phase versus input relationship allows synapses to store a complimentary pattern

to the synaptic weights. When mapping the pattern to the synapses the dispersion of firing phase slowly disappears, at which point learning terminates naturally. During retrieval of the pattern, the phase relationship imposed by the original pattern is reversed. This model of memory storage reproduces several features of the hippocampal place cell system, such as theta-phase precession and reverse replay.

Importantly, the subthreshold resonance learning model provides an important demonstration of how neural networks can translate rate coded information to phase coded information. Neuronal membranes act as low-pass filters. If an external set of neurons are rate coding information, the inputs they send to our focal network would largely be steady state depolarizing inputs like those employed in the model. Subthreshold resonance provides a mechanism to reliably translate this firing rate information to phase information.

5.2 Future Directions

5.2.1 The role of neuromodulation in the storage and consolidation of network level memory

To extend upon the work Chapters II and III presented on how changing levels of ACh impact information processing at the network level the next step is to add synaptic plasticity so that memories can be encoded, recalled, and then consolidated. It is well known that sleep is critical for the proper function of memory [132]. ACh is dramatically modulated across the sleep-wake cycle; highest during waking, intermediate during REM, and low during NREM [13]. Synaptic plasticity combined with the changes in spatiotemporal spiking patterns can provide insights into how memories are stored as attractors and how cycling between wake, REM, and NREM consolidate memories.

There are two competing hypotheses on the nature of sleep's role in memory. The

synaptic homeostasis hypothesis states that sleep is used to uniformly reduce the synaptic strength in the network [60]. This reduction would offset the strengthening that occurs as experience is stored during the day. This is supported by the reduction in slow wave power that occurs during sleep [38]. The second hypothesis, synaptic embossing hypothesis, builds upon this by suggesting that replay during REM sleep strengthens recent memories while NREM sleep renormalizes synaptic strength [61], though recently it has been suggested that forgetting is equally important during sleep [133].

One complicating factor when considering a model of neuromodulation during sleep is that ACh is not the only neuromodulator that cycles during sleep-wake cycles. Importantly, Norepinepherine (NE) also decreases as an animal enters sleep, though it is equally low during REM and NREM [134]. ACh and NE work in concert to shape learning through synaptic plasticity [135]. As seen in Chapter IV, synaptic plasticity has two sides, Long-Term Potentiation (LTP) and Long-Term Depression (LTD), that act according to the relative spike timing between a pair of connected neurons. In pairs of cortical pyramidal cells the amount of potentiation is controlled by the level of NE in the network, while ACh controls the amount of depression. This leads to an Spike Timing-Dependent Plasticity (STDP) envelope that is unique across wake, REM, and NREM.

I have begun developing a fully plastic model of sleep state dependent ACh/ NE modulation in cortical networks. Paired with the dynamic effects of ACh neuromodulation the magnitude potentiation and depression is changed across the sleep state according to [135] (Fig 5.2). In the waking state STDP is biased to LTP. In NREM, both ACh and NE are low which leads to an equal reduction in both LTP and LTD. In REM however, NE is low and ACh is high which results in STDP biased toward

LTD.

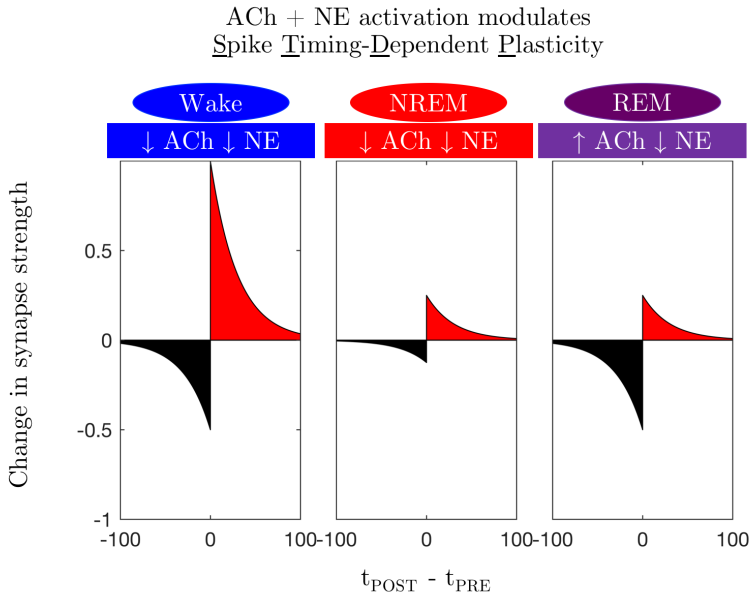

Figure 5.2: **Modulation of the SDTP envelope across the sleep-wake cycle.** During wake the STDP envelope is biased toward LTP (red), during NREM both LTP and LTD are equally reduced as ACh and NE are both low. During REM the learning rule is biased to LTD (black)

For simulations spatial attractors were formed by stimulating an area in the network with a radius of 5 neurons. A total of six points were encoded to the network for 250 ms each under waking conditions (Fig 5.2). This stimulation protocol formed discrete spatial attractors (Fig 5.3). Over the next 75 seconds of simulation time 5 cycles of NREM to REM sleep were simulated (20% of each cycle was spent in REM). After completion of the sleep cycle the set of point memories were consolidated into a path attractor connecting the stored points. The peak synaptic strength is not significantly altered by the sleep cycle, but the spatial pattern of where neurons direct synaptic output to is modified.

Clearly there is significantly more to be done with this model. First the diversity in STDP shape requires a systematic understanding of how bias toward either LTP or LTD affects forming stabile attractors within the network. For a localized bump

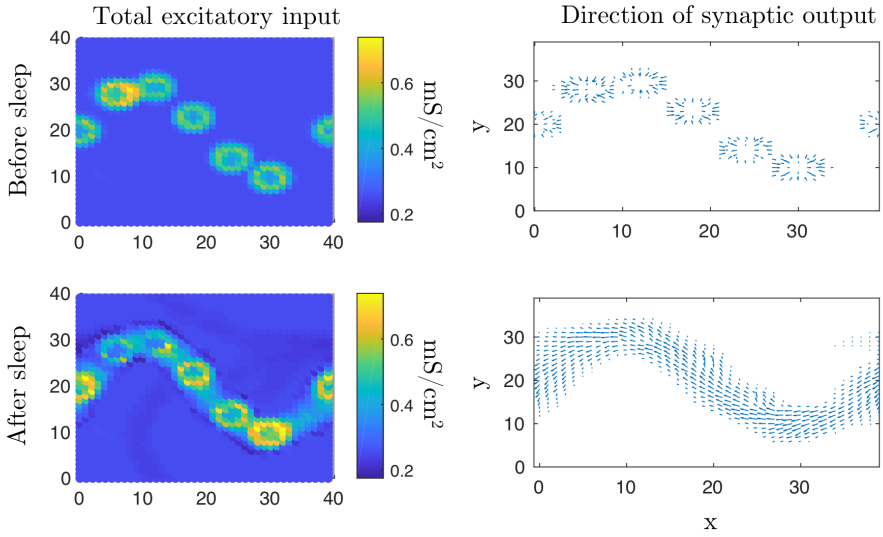

Figure 5.3: **Consolidation of point memories during sleep.** Prior to the sleep simulation six point memories were encoded under waking conditions for 250 ms each. During the sleep simulation the stable point attractors are connected into a path attractor which yields a sequential reactivation of the point memories. Color plots show the total excitatory input conductance for each excitatory neuron in the network. Vector plots show the average direction of synaptic output for each neuron. The size and direction of the vector indicates the direction of that neurons strongest outputs. No arrow indicates outputs are equal in all directions.

of activity to form a stable attractor through synaptic plasticity synapses need to be strengthened toward the fast neurons at the center of bump and weakened toward the low firing neurons at the edge. This will direct synaptic output to the center of the bump and stabilize the memory. The STDP conditions that support this need to be identified and a mechanistic explanation developed. Detailed investigation of how phase of the sleep cycle contribute to consolidating point attractors is still need as well. With these caveats in mind, this model has promise to add information storage roles for each of the three states outlined in Figure 5.1.

5.2.2 Dynamic changes in ACh facilitate switching between rate coding and phase coding

Using the Ks model we have shown that neuromodulation of the Muscarinic Current (I_M) can switch networks from a rate coding regime when ACh is high ($\bar{g}_{Ks}$) to an oscillatory phase coding state when ACh is low ($\bar{g}_{Ks}$ is high). This neuronal model recreates biophysical changes displayed in neurons when the muscarinic system is activated, including gain modulation, Phase Response Curve (PRC) modulation, and Spike-Frequency Adaptation (SFA) modulation (Fig 1.1). As ACh levels are continuously changed, these three properties are inflected over different ranges of the maximal conductance of I_M, $\bar{g}_{Ks}$.

It is important to note that all three of these properties are important for switching from a rate to a phase coding regime. For rate coding in high ACh conditions, high gain is beneficial in widening the firing rate distribution for a given range of synaptic inputs. Low SFA allows neurons to persist in firing to maintain a representation in frequency space and low synchrony from a Type 1 PRC prevents a reduction in frequency variation. For phase coding under low ACh conditions, low gain reduces frequency variation in the network, while a Type 2 PRC and high SFA induce increased periodicity allowing for phase differences to persist.

In dynamical systems theory it is well known that PRC type determines whether coupled oscillators will synchronize and this has been used as one of the dynamical mechanisms to describe the emergence of synchrony in neural networks. The PRC provides an elegant explanation for why networks of Type 2 neurons synchronize, while those with Type 1 neurons do not. Type 1 neurons can only shorten the period in response to synaptic input leading to unstable synchrony if it ever emerges. On the other hand, Type 2 neurons can either elongate or shorten their period which will not

only push networks to synchronize spiking, but also stabilize synchrony to noisy input or perturbations. One limitation of this criteria is that the variance in frequencies be small enough for synaptic mechanisms to lead to the emergence of synchrony. When this criteria is not met, and network connectivity permits, networks will break into synchronized clusters of neurons with similar frequencies [136]. Thus, reductions in ACh level provide two dynamical substrates for phase coding: 1) near uniformity in firing rates across the network, and 2) the ability of neurons to collectively organize into network-wide oscillatory behavior.

This modulation of frequency variance and phase locking by ACh provides a basis for different coding schemes (Fig 5.4). Across multiple network topolgies, high ACh networks have high frequency variance and low phase locking (as measured by Mean Phase Coherence (MPC)). As ACh is reduced ($\bar{g}_{Ks}$ is increased), frequencies become more uniform, and phase locking increases. These two effects on the character of network dynamics provide a substrate for each coding scheme at each pole of cholinergic modulation. High ACh networks are primed for rate coding and low ACh networks are primed for phase coding.

Directly quantifying the dependence of a network firing pattern on a particular network structure for networks of the same connection topology scheme would provide strong evidence that Type 1 networks have rate coding firing patterns that reflect a given pattern of external inputs while Type 2 firing patterns provide oscillatory phase coding dynamics.

That the transition from high rate varience to phase locked firing patterns occurs over the $\bar{g}_{Ks}$ range when the gain of the neuron (f/I curve) is significantly modulated points to the importance of this property for switching coding regimes. When a network of high gain neurons are connected, slight variations in synaptic input will

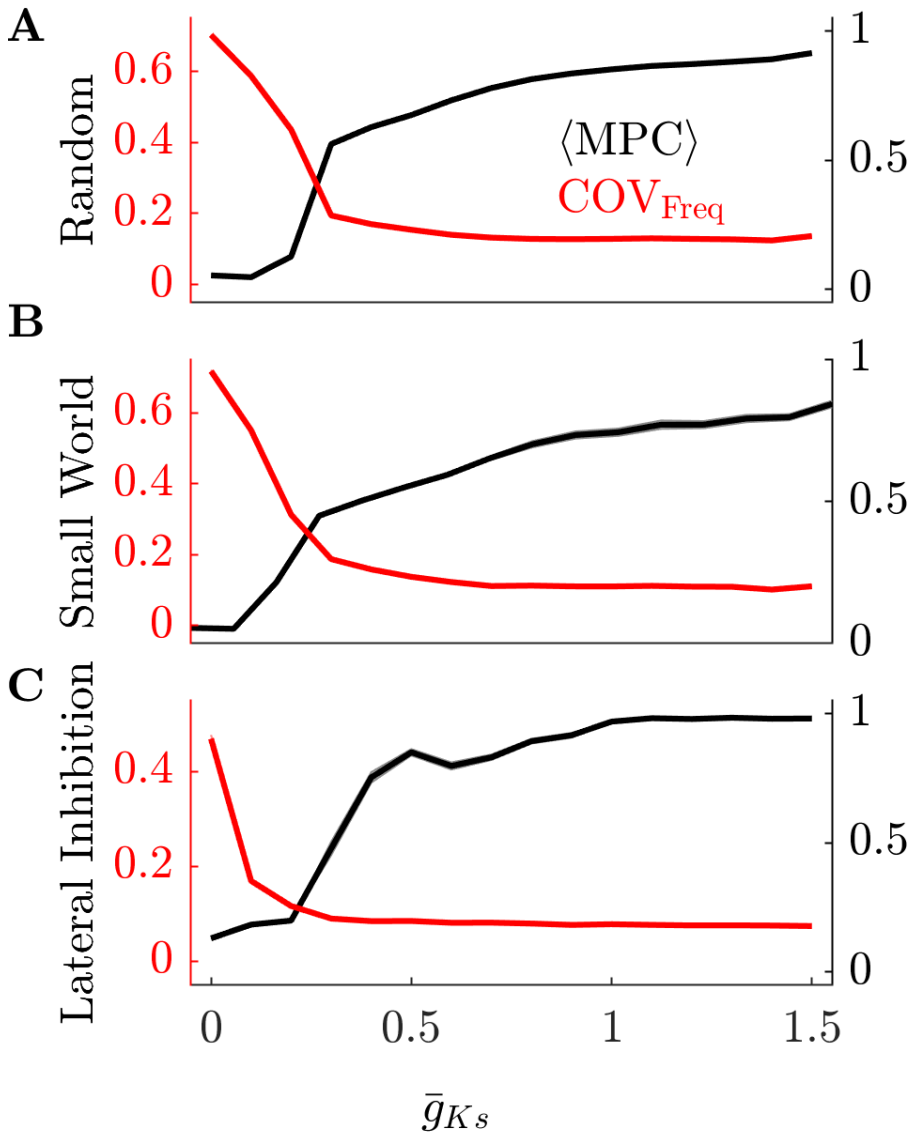

Figure 5.4: **Cholinergic modulation of phase locking and frequency distribution.** The transition from high frequency variance to high phase locking across three network topologies shows how cholinergic modulation can change coding principles. High ACh networks have highly varied firing rates as measured by the coefficient of variation. Firing rates quickly become more uniform as $\bar{g}_{Ks}$ increases. Conversely, MPC (phase locking) is high for low ACh networks. (A) random networks, (B) small world networks, (C) lateral inhibition networks. Error bars indicate s.e.m.

result in higher firing rate differences between neurons. This wide, input dependent, firing rate distribution will drive the network firing rate distribution and be reproducible for a given set of inputs or a given network structure. As gain is reduced, frequency differences between neurons will be reduced allowing neuronal properties

such as SFA and PRC effects to impact network dynamics in a significant way. For example, it is well known that networks of periodic oscillators synchronize easier when the frequency range is reduced and that large variance in frequencies promotes the formation of discrete clusters of synchronization [137, 136, 138].

Spike initiation dynamics and the adaptation mechanics of neurons have been suggested as being substrates for coding through integration or coincidence detection [139, 140]. While both integrative and coincidence coding can exist with wide firing rate distributions, phase coding relies on neurons being close in frequency while high neuronal gain facilitates rate coding [141]. The importance of co-modulation of neuronal gain and excitability type in transitioning a network from rate to phase coding would be a novel and important result.

Gain modulation improves signal recognition in a variety of brain regions [142, 143, 144, 145]. In many cases gain modulation is attributed to fluctuations in synaptic inputs and synaptic plasticity due to gain modulation being stimulus dependent [146, 147, 148]. But changes in ACh tone also change the gain response of neurons [149, 150, 151]. ACh release is increased when an animal is performing an attentional task and its release is correlated with task performance [152, 153, 154]. These results point to cholinergic modulation priming neuronal networks to respond with an appropriate rate code to a given cue by increasing the gain of the neurons. This also indicates that rate coding may be better at facilitating representations of sensory information than phase coding.

The Type 2 dynamics of the low ACh state support robust synchronized bursting required for oscillations in population activity [25, 26, 28]. ACh release is important for the generation of the theta rhythm in the hippocampus [155, 30, 156]. But a temporal analysis of both ACh release and theta band power shows that peaks in

ACh release lag behind increases in theta power [157]. This suggests that ACh release is actually working to disrupt synchrony within the theta oscillation. Further evidence for the role ACh release could play in reducing synchronous firing is seen in its suppression of sharp wave ripples [30].

ACh release is very closely related to the sleep-wake cycle. ACh release is highest during wakefulness and REM sleep and lower during non-REM (NREM) sleep [13]. When the Ks model simulates these levels of ACh it recreates similar changes in spiking dynamics that are seen across these states [34]. Additionally, the effects on synaptic plasticity, namely high ACh leads to increases in average synaptic weights and low ACh decreases them, support the synaptic homeostasis hypothesis [60, 31], but at the same time the proposed shift in the coding schemes paints more complex picture of specific roles of sleep cycles. The widening of neuronal firing rate distributions across sleep-wake states also indicates that gain modulation by ACh is shaping network activity [158]. The role of ACh level in sleep dependent memory consolidation and synaptic homeostasis suggests that phase coding is optimized for the storage of information. This is supported by the role neuronal resonances play in network level pattern storage [36].

ACh is a neuromodulator that is critical for cognitive processes throughout the brain. The biophysical changes in neural excitability that I_M governs lead to significant changes in the spiking and oscillatory processes in the brain. The effects of gain modulation in switching between circuit activity that has high or low dependence on network structure may be central to the role of ACh role in information processing at the network level. Additionally, the dynamic nature of ACh release could allow for a stable network to coordinate information processing functions across various brain states. While ACh has other pathways of neuromodulation, notably through the

nicotinic receptor which directly depolarizes neurons [72], the results presented here show that the muscarinic effects of changing ACh levels can change coding modes to a large degree.

BIBLIOGRAPHY

BIBLIOGRAPHY

[1] Hodgkin AL, Huxley AF (1952) A quantitative description of membrane current and its application to conduction and excitation in nerve. *The Journal of Physiology* 117(4):500–544.

[2] Gray CM, Singer W (1989) Stimulus-specific neuronal oscillations in orientation columns of cat visual cortex. *Proceedings of the National Academy of Sciences* 86(5):1698–1702.

[3] Hubel DH, Wiesel T (1962) Receptive fields, binocular interaction and functional architecture in the cat's visual cortex. *Journal of Physiology* 160:106–154.

[4] Hubel DH, Wiesel T (1959) Receptive fields of single neurones in the cat's striate cortex. *Journal of Physiology* 148:574–591.

[5] Gerstner W, Kreiter AK, Markram H, Herz AV (1997) Neural codes: firing rates and beyond. *Proceedings of the National Academy of Sciences* 94(24):12740–12741.

[6] Olshausen BA, Field DJ (2006) What is the other 85Problems in Systems Neuroscience, eds. van Hemmen JL, Sejnowski TJ. (New York), pp. 182–213.

[7] Ainsworth M, et al. (2012) Rates and rhythms: a synergistic view of frequency and temporal coding in neuronal networks. *Neuron* 75(4):572–583.

[8] Nadasdy Z (2010) Binding by asynchrony: the neuronal phase code. *Frontiers in Neuroscience* 4:1–11.

[9] Theunissen F, Miller JP (1995) Temporal encoding in nervous systems: a rigorous definition. *Journal of Computational Neuroscience* 2(2):149–162.

[10] Von der Malsburg C (1999) The what and why of binding: the modeler's perspective. *Neuron* 24(1):95–104– 111–25.

[11] Skaggs WE, McNaughton BL, Wilson MA, Barnes CA (1996) Theta phase precession in hippocampal neuronal populations and the compression of temporal sequences. *Hippocampus* 6(2):149–172.

[12] Parikh V, Sarter M (2008) Cholinergic Mediation of Attention. *Annals of the New York Academy of Sciences* 1129(1):225–235.

[13] Marrosu F, et al. (1995) Microdialysis measurement of cortical and hippocampal acetylcholine release during sleep-wake cycle in freely moving cats. *Brain research* 671(2):329–332.

[14] Marrion NV (1997) Control of M-current. *Annual review of physiology* 59(1):483–504.

[15] Prescott SA, Sejnowski TJ, Ratte S, De Koninck Y (2008) Pyramidal Neurons Switch From Integrators In Vitro to Resonators Under In Vivo-Like Conditions. *Journal of Neurophysiology* 100(6):3030–3042.

[16] Izhikevich EM (2007) *Dynamical systems in neuroscience*, Geometry of Excitability and Bursting. (MIT press, Cambridge, MA), 1 edition.

[17] Gutkin BS, Ermentrout GB (1998) Dynamics of membrane excitability determine interspike interval variability: a link between spike generation mechanisms and cortical spike train statistics. *Neural Computation* 10(5):1047–1065.

[18] Gutkin B, Pinto D, Ermentrout B (2003) Mathematical neuroscience: from neurons to circuits to systems. *Journal of Physiology-Paris* 97(2-3):209–219.

[19] Stiefel KM, Gutkin BS, Sejnowski TJ (2008) Cholinergic Neuromodulation Changes Phase Response Curve Shape and Type in Cortical Pyramidal Neurons. *PLoS ONE* 3(12):e3947.

[20] Tsuno Y, Schultheiss NW, Hasselmo ME (2013) In vivo cholinergic modulation of the cellular properties of medial entorhinal cortex neurons. *The Journal of Physiology* 591(10):2611–2627.

[21] Tang AC, Bartels AM, Sejnowski TJ (1997) Effects of cholinergic modulation on responses of neocortical neurons to fluctuating input. *Cerebral Cortex* 7(6):502–509.

[22] Stiefel KM, Gutkin BS, Sejnowski TJ (2008) The effects of cholinergic neuromodulation on neuronal phase-response curves of modeled cortical neurons. *Journal of Computational Neuroscience* 26(2):289–301.

[23] Watts DJ, Strogatz SH (1998) Collective dynamics of 'small-world' networks. *Nature* 393(6684):440–442.

[24] Rubinov M, Sporns O (2010) Complex network measures of brain connectivity: Uses and interpretations. *NeuroImage* 52(3):1059–1069.

[25] Bogaard A, Parent J, Zochowski M, Booth V (2009) Interaction of Cellular and Network Mechanisms in Spatiotemporal Pattern Formation in Neuronal Networks. *Journal of Neuroscience* 29(6):1677–1687.

[26] Fink CG, Zochowski M, Booth V (2011) Cellularly-Driven Differences in Network Synchronization Propensity Are Differentially Modulated by Firing Frequency. *PLoS Computational Biology* 7(5):e1002062.

[27] Groleau M, Kang JI, Huppé-Gourgues F, Vaucher E (2015) Distribution and effects of the muscarinic receptor subtypes in the primary visual cortex. *Frontiers in Synaptic Neuroscience* 7:1–9.

[28] Knudstrup S, Zochowski M, Booth V (2016) Network burst dynamics under heterogeneous cholinergic modulation of neural firing properties and heterogeneous synaptic connectivity. *European Journal of Neuroscience* 43(10):1321–1339.

[29] Mofakham S, Fink CG, Booth V, Zochowski M (2016) Interplay between excitability type and distributions of neuronal connectivity determines neuronal network synchronization. *Physical Review E* 94(4):042427.

[30] Hasselmo ME (2006) The role of acetylcholine in learning and memory. *Current opinion in neurobiology* 16(6):710–715.

[31] Fink CG, Murphy GG, Booth V, Zochowski M (2013) A Dynamical Role for Acetylcholine in Synaptic Renormalization. *PLoS Computational Biology* 9(3):e1002939.

[32] Renart A, Song P, Wang XJ (2003) Robust spatial working memory through homeostatic synaptic scaling in heterogeneous cortical networks. *Neuron* 38(3):473–485.

[33] Zhang S, et al. (2014) Long-range and local circuits for top-down modulation of visual cortex processing. *Science* 345(6197):660–665.

[34] Roach JP, Ben-Jacob E, Sander LM, Zochowski M (2015) Formation and Dynamics of Waves in a Cortical Model of Cholinergic Modulation. *PLoS Computational Biology* 11(8):e1004449.

[35] Roach JP, Sander LM, Zochowski M (2016) Memory recall and spike-frequency adaptation. *Physical Review E* 93(5):052307.

[36] Roach JP, et al. (2018) Resonance with subthreshold oscillatory drive organizes activity and optimizes learning in neural networks. *Proceedings of the National Academy of Sciences* 115(13):E3017–E3025.

[37] Steriade M, Timofeev I, Grenier F (2001) Natural waking and sleep states: a view from inside neocortical neurons. *Journal of Neurophysiology* 85(5):1969–1985.

[38] Vyazovskiy VV, et al. (2009) Cortical Firing and Sleep Homeostasis. *Neuron* 63(6):865–878.

[39] Herrero JL, et al. (2008) Acetylcholine contributes through muscarinic receptors to attentional modulation in V1. *Nature* 454(7208):1110–1114.

[40] Hasselmo ME, Sarter M (2010) Modes and Models of Forebrain Cholinergic Neuromodulation of Cognition. *Neuropsychopharmacology* 36(1):52–73.

[41] Wimmer K, Nykamp DQ, Constantinidis C, Compte A (2014) Bump attractor dynamics in prefrontal cortex explains behavioral precision in spatial working memory. *Nature Neuroscience* 17(3):431–439.

[42] Huber R, et al. (2007) TMS-Induced Cortical Potentiation during Wakefulness Locally Increases Slow Wave Activity during Sleep. *PLoS ONE* 2(3):e276.

[43] Massimini M, et al. (2007) Triggering sleep slow waves by transcranial magnetic stimulation. *Proceedings of the National Academy of Sciences* 104(20):8496–8501.

[44] Massimini M, Tononi G, Huber R (2009) Slow waves, synaptic plasticity and information processing: insights from transcranial magnetic stimulation and high-density EEG experiments. *European Journal of Neuroscience* 29(9):1761–1770.

[45] Aiken SP, Lampe BJ, Murphy PA, Brown BS (1995) Reduction of spike frequency adaptation and blockade of M-current in rat CA1 pyramidal neurones by linopirdine (DuP 996), a neurotransmitter release enhancer. *British journal of pharmacology* 115(7):1163–1168.

[46] Douglas RJ, Martin KAC (2004) Neuronal circuits of the neocortex. *Annual Review of Neuroscience* 27:419–451.

[47] Aton SJ, et al. (2013) Visual experience and subsequent sleep induce sequential plastic changes in putative inhibitory and excitatory cortical neurons. *Proceedings of the National Academy of Sciences* 110(8):3101–3106.

[48] Sahara S, Yanagawa Y, O'Leary DDM, Stevens CF (2012) The fraction of cortical GABAergic neurons is constant from near the start of cortical neurogenesis to adulthood. *Journal of Neuroscience* 32(14):4755–4761.

[49] Amari S (1977) Dynamics of pattern formation in lateral-inhibition type neural fields. *Biological cybernetics* 27(2):77–87.

[50] Bai L, Breen D (2008) Calculating Center of Mass in an Unbounded 2D Environment. *Journal of Graphics, GPU, and Game Tools* 13(4):53–60.

[51] Schneider-Mizell CM, Parent JM, Ben-Jacob E, Zochowski M, Sander LM (2010) From network structure to network reorganization: implications for adult neurogenesis. *Physical Biology* 7(4):046008.

[52] Kilpatrick ZP, Ermentrout B, Doiron B (2013) Optimizing Working Memory with Heterogeneity of Recurrent Cortical Excitation. *Journal of neuroscience* 33(48):18999–19011.

[53] Steriade M, Amzica F, Nuñez A (1993) Cholinergic and noradrenergic modulation of the slow (approximately 0.3 Hz) oscillation in neocortical cells. *Journal of Neurophysiology* 70(4):1385–1400.

[54] Baghdoyan HA, Lydic R (1999) M2 muscarinic receptor subtype in the feline medial pontine reticular formation modulates the amount of rapid eye movement sleep. *Sleep* 22(7):835–847.

[55] Massimini M, Huber R, Ferrarelli F, Hill S, Tononi G (2004) The Sleep Slow Oscillation as a Traveling Wave. *Journal of Neuroscience* 24(31):6862–6870.

[56] Barreiro AK, Shea-Brown E, Thilo EL (2010) Time scales of spike-train correlation for neural oscillators with common drive. *Physical Review E*.

[57] Stickgold R, Whidbee D, Schirmer B, Patel V, Hobson JA (2000) Visual discrimination task improvement: A multi-step process occurring during sleep. *Journal of cognitive neuroscience* 12(2):246–254.

[58] Gais S, Mölle M, Helms K, Born J (2002) Learning-dependent increases in sleep spindle density. *Journal of Neuroscience* 22(15):6830–6834.

[59] Marshall L, Helgadóttir H, Mölle M, Born J (2006) Boosting slow oscillations during sleep potentiates memory. *Nature* 444(7119):610–613.

[60] Tononi G, Cirelli C (2003) Sleep and synaptic homeostasis: a hypothesis. *Brain Research Bulletin* 62(2):143–150.

[61] Ribeiro S (2012) Sleep and plasticity. *Pflügers Archiv : European journal of physiology* 463(1):111–120.

[62] Blanco W, et al. (2015) Synaptic Homeostasis and Restructuring across the Sleep-Wake Cycle. *PLoS Computational Biology* 11(5):e1004241–29.

[63] Dumoulin Bridi MC, et al. (2015) Rapid eye movement sleep promotes cortical plasticity in the developing brain. *Science Advances* 1(6):e1500105–e1500105.

[64] Feld GB, et al. (2013) Slow wave sleep induced by GABA agonist tiagabine fails to benefit memory consolidation. *Sleep* 36(9):1317–1326.

[65] Jones BE (2005) From waking to sleeping: neuronal and chemical substrates. *Trends in Pharmacological Sciences* 26(11):578–586.

[66] Winsky-Sommerer R (2009) Role of GABAA receptors in the physiology and pharmacology of sleep. *European Journal of Neuroscience* 29(9):1779–1794.

[67] Pitler TA, Alger BE (1992) Cholinergic excitation of GABAergic interneurons in the rat hippocampal slice. *The Journal of Physiology* 450:127–142.

[68] Haas HL (1982) Cholinergic disinhibition in hippocampal slices of the rat. *Brain research* 233(1):200–204.

[69] Amit DJ (1995) The Hebbian paradigm reintegrated: local reverberations as internal representations. *Behavioral and Brain Sciences* 18:617–657.

[70] Amit DJ, Brunel N (1997) Model of global spontaneous activity and local structured activity during delay periods in the cerebral cortex. *Cerebral Cortex* 7(3):237–252.

[71] Compte A (2000) Synaptic Mechanisms and Network Dynamics Underlying Spatial Working Memory in a Cortical Network Model. *Cerebral Cortex* 10(9):910–923.

[72] Sarter M, Lustig C, Howe WM, Gritton H, Berry AS (2014) Deterministic functions of cortical acetylcholine. *European Journal of Neuroscience* 39(11):1912–1920.

[73] Coombes S (2005) Waves, bumps, and patterns in neural field theories. *Biological cybernetics* 93(2):91–108.

[74] Bressloff PC (2011) Spatiotemporal dynamics of continuum neural fields. *Journal of Physics A: Mathematical and Theoretical* 45(3):033001.

[75] Muir DR, Cook M (2014) Anatomical Constraints on Lateral Competition in Columnar Cortical Architectures. *Neural Computation* 26(8):1624–1666.

[76] Binzegger T, Douglas RJ, Martin KAC (2007) Stereotypical Bouton Clustering of Individual Neurons in Cat Primary Visual Cortex. *Journal of neuroscience* 27(45):12242–12254.

[77] Binzegger T, Douglas RJ, Martin KAC (2009) Topology and dynamics of the canonical circuit of cat V1. *Neural Networks* 22(8):1071–1078.

[78] Pereda AE, et al. (2013) Gap junction-mediated electrical transmission: Regulatory mechanisms and plasticity. *BBA - Biomembranes* 1828(1):134–146.

[79] Pinto DJ, Ermentrout GB (2001) Spatially structured activity in synaptically coupled neuronal networks: I. Traveling fronts and pulses. *SIAM Journal on Applied Mathematics* 62:206–225.

[80] Compte A, Sanchez-Vives MV, McCormick DA, Wang XJ (2003) Cellular and network mechanisms of slow oscillatory activity (¡1 Hz) and wave propagations in a cortical network model. *Journal of Neurophysiology* 89(5):2707–2725.

[81] Ermentrout B (1998) Linearization of FI curves by adaptation. *Neural Computation*.

[82] Higgs MH, Slee SJ, Spain WJ (2006) Diversity of gain modulation by noise in neocortical neurons: regulation by the slow afterhyperpolarization conductance. *Journal of Neuroscience* 26(34):8787–8799.

[83] Glasgow SD, Chapman CA (2013) Muscarinic Depolarization of Layer II Neurons of the Parasubiculum. *PLoS ONE* 8(3):1–14.

[84] Patil MM, Hasselmo ME (1999) Modulation of inhibitory synaptic potentials in the piriform cortex. *Journal of Neurophysiology* 81(5):2103–2118.

[85] Amit DJ, Gutfreund H, Sompolinsky H (1987) Statistical mechanics of neural networks near saturation. *Annals of Physics* 173:30–67.

[86] Hasselmo ME, Anderson BP, Bower JM (1992) Cholinergic modulation of cortical associative memory function. *Journal of Neurophysiology* 67(5):1230–1246.

[87] Hopfield JJ (1982) Neural networks and physical systems with emergent collective computational abilities. *Proceedings of the National Academy of Sciences* 79(8):2554–2558.

[88] Recanatesi S, Katkov M, Romani S, Tsodyks M (2015) Neural Network Model of Memory Retrieval. *Frontiers in computational neuroscience* 9(129):275–11.

[89] Lerner I, Shriki O (2014) Internally- and externally-driven network transitions as a basis for automatic and strategic processes in semantic priming: theory and experimental validation. *Frontiers in psychology* 5:314.

[90] Akrami A, Russo E, Treves A (2012) Lateral thinking, from the Hopfield model to cortical dynamics. *Brain research* 1434(C):4–16.

[91] Lewenstein M, Nowak A (1989) Fully connected neural networks with self-control of noise levels. *Physical Review Letters* 62(2):225–228.

[92] Amit D, Gutfreund H, Sompolinsky H (1985) Spin-glass models of neural networks. *Physical review. A* 32(2):1007–1018.

[93] Agliari E, Barra A, Galluzzi A, Tantari D (2014) A walk in the statistical mechanical formulation of neural networks alternative routes to hebb prescription in *Proceedings of the International Conference on Neural Computation Theory and Applications*, eds. K M, J F, J F. pp. 210–217.

[94] Monasson R, Rosay S (2015) Transitions between Spatial Attractors in Place-Cell Models. *Physical Review Letters* 115(9):098101–5.

[95] Hasselmo ME, Sarter M (2011) Modes and models of forebrain cholinergic neuromodulation of cognition. *Neuropsychopharmacology* 36(1):52–73.

[96] Hopfield JJ (2010) Neurodynamics of mental exploration. *Proceedings of the National Academy of Sciences* 107(4):1648–1653.

[97] Vazquez J, Baghdoyan HA (2001) Basal forebrain acetylcholine release during REM sleep is significantly greater than during waking. *American journal of physiology. Regulatory, integrative and comparative physiology* 280(2):R598–601.

[98] Buzsáki G, Anastassiou CA, Koch C (2012) The origin of extracellular fields and currents–EEG, ECoG, LFP and spikes. *Nature Reviews Neuroscience* 13(6):407–420.

[99] Benchenane K, et al. (2010) Coherent Theta Oscillations and Reorganization of Spike Timing in the Hippocampal- Prefrontal Network upon Learning. *Neuron* 66(6):921–936.

[100] Colgin LL (2013) Mechanisms and Functions of Theta Rhythms. *Annual Review of Neuroscience* 36(1):295–312.

[101] Slezia A, Hangya B, Ulbert I, Acsady L (2011) Phase Advancement and Nucleus-Specific Timing of Thalamocortical Activity during Slow Cortical Oscillation. *Journal of neuroscience* 31(2):607–617.

[102] Puentes-Mestril C, Aton SJ (2017) Linking network activity to synaptic plasticity during sleep: Hypotheses and recent data. *Frontiers in Neural Circuits* 11:61.

[103] Dragoi G, Buzsáki G (2006) Temporal encoding of place sequences by hippocampal cell assemblies. *Neuron* 50(1):145–157.

[104] Hutcheon B, Miura RM, Puil E (1996) Subthreshold membrane resonance in neocortical neurons. *Journal of Neurophysiology* 76(2):683–697.

[105] Leung LS, Yu HW (1998) Theta-frequency resonance in hippocampal CA1 neurons in vitro demonstrated by sinusoidal current injection. *Journal of Neurophysiology* 79(3):1592–1596.

[106] Sanhueza M, Bacigalupo J (2005) Intrinsic subthreshold oscillations of the membrane potential in pyramidal neurons of the olfactory amygdala. *European Journal of Neuroscience* 22(7):1618–1626.

[107] Hu H, Vervaeke K, Storm JF (2004) Two forms of electrical resonance at theta frequencies, generated by M-current, h-current and persistent Na +current in rat hippocampal pyramidal cells. *The Journal of Physiology* 545(3):783–805.

[108] Wang XJ (2010) Neurophysiological and Computational Principles of Cortical Rhythms in Cognition. *Physiological Reviews* 90(3):1195–1268.

[109] Yan ZQ, et al. (2012) Membrane resonance and its ionic mechanisms in rat subthalamic nucleus neurons. *Neuroscience Letters* 506(1):160–165.

[110] O'Keefe J, Recce ML (1993) Phase relationship between hippocampal place units and the EEG theta rhythm. *Hippocampus* 3(3):317–330.

[111] Hasselmo ME, Stern CE (2014) Theta rhythm and the encoding and retrieval of space and time. *NeuroImage* 85(P2):656–666.

[112] Jeewajee A, et al. (2013) Theta phase precession of grid and place cell firing in open environments. *Philosophical Transactions of the Royal Society B: Biological Sciences* 369(1635):20120532–20120532.

[113] van der Meer MAA, Redish AD (2011) Theta Phase Precession in Rat Ventral Striatum Links Place and Reward Information. *Journal of neuroscience* 31(8):2843–2854.

[114] Buhry L, Azizi AH, Cheng S (2011) Reactivation, Replay, and Preplay: How It Might All Fit Together. *Neural Plasticity* 2011(8):1–11.

[115] Foster DJ, Wilson MA (2006) Reverse replay of behavioural sequences in hippocampal place cells during the awake state. *Nature* 440(7084):680–683.

[116] Lisman J, Redish AD (2009) Prediction, sequences and the hippocampus. *Philosophical Transactions of the Royal Society B: Biological Sciences* 364(1521):1193–1201.

[117] Wikenheiser AM, Redish AD (2012) The balance of forward and backward hippocampal sequences shifts across behavioral states. *Hippocampus* 23(1):22–29.

[118] Lau T, Zochowski M (2011) The Resonance Frequency Shift, Pattern Formation, and Dynamical Network Reorganization via Sub-Threshold Input. *PLoS ONE* 6(4):e18983–8.

[119] Shtrahman E, Zochowski M (2015) Pattern segmentation with activity dependent natural frequency shift and sub-threshold resonance. *Scientific Reports* 5(1):574–10.

[120] Ognjanovski N, et al. (2017) Parvalbumin-expressing interneurons coordinate hippocampal network dynamics required for memory consolidation. *Nature Communications* 8:15039.

[121] Ognjanovski N, Maruyama D, Lashner N, Zochowski M, Aton SJ (2014) CA1 hippocampal network activity changes during sleep-dependent memory consolidation. *Frontiers in Systems Neuroscience* 8(1 APR):61.

[122] Pikovsky A, Rosenblum M, Kurths J (2002) *Synchronization: a universal concept in nonlinear science*. (Cambride University Press, New York).

[123] Bi G, Poo M (2001) Synaptic modification by correlated activity: Hebb's postulate revisited. *Annual Review of Neuroscience*.

[124] Lester RA, Clements JD, Westbrook GL, Jahr CE (1990) Channel kinetics determine the time course of NMDA receptor-mediated synaptic currents. *Nature* 346(6284):565–567.

[125] Colgin LL (2016) Rhythms of the hippocampal network. *Nature Reviews Neuroscience* 17(4):239–249.

[126] Wu J, et al. (2017) Functional network stability and average minimal distance - A framework to rapidly assess dynamics of functional network representations. *Journal of neuroscience methods* 296:69–83.

[127] Davidson TJ, Kloosterman F, Wilson MA (2009) Hippocampal replay of extended experience. *Neuron* 63(4):497–507.

[128] Zenke F, Gerstner W (2017) Hebbian plasticity requires compensatory processes on multiple timescales. *Philosophical transactions of the Royal Society of London. Series B, Biological sciences* 372(1715).

[129] Harvey CD, Collman F, Dombeck DA, Tank DW (2009) Intracellular dynamics of hippocampal place cells during virtual navigation. *Nature* 461(7266):941–946.

[130] Mehta MR, Quirk MC, Wilson MA (2000) Experience-dependent asymmetric shape of hippocampal receptive fields. *Neuron* 25(3):707–715.

[131] Lee AK, Wilson MA (2002) Memory of sequential experience in the hippocampus during slow wave sleep. *Neuron* 36(6):1183–1194.

[132] Jenkins JG, Dallenbach KM (1924) Obliviscence during sleep and waking. *American Journal of Psyhology* 35(4):605–612.

[133] Poe GR (2017) Sleep Is for Forgetting. *Journal of neuroscience* 37(3):464–473.

[134] Léna I, et al. (2005) Variations in extracellular levels of dopamine, noradrenaline, glutamate, and aspartate across the sleep–wake cycle in the medial prefrontal cortex and nucleus accumbens of freely moving rats. *Journal of neuroscience research* 81(6):891–899.

[135] Seol GH, et al. (2007) Neuromodulators Control the Polarity of Spike-Timing-Dependent Synaptic Plasticity. *Neuron* 55(6):919–929.

[136] Acebrón JA, Bonilla LL, Vicente CJP, Ritort F, Spigler R (2005) The Kuramoto model: A simple paradigm for synchronization phenomena. *Reviews of Modern Physics* 77(1):137–185.

[137] Osipov GV, Suchchik MM (1998) Synchronized clusters and multistability in arrays of oscillators with different natural frequencies. *Physical Review E* 58(6):7198–7207.

[138] Favaretto C, Cenedese A, Pasqualetti F (2017) Cluster synchronization in networks of kuramoto oscillators. *IFAC PapersOnLine* 50(1):2433–2438.

[139] Ratté S, Hong S, De Schutter E, Prescott SA (2013) Impact of Neuronal Properties on Network Coding: Roles of Spike Initiation Dynamics and Robust Synchrony Transfer. *Neuron* 78(5):758–772.

[140] Prescott SA, Sejnowski TJ (2008) Spike-Rate Coding and Spike-Time Coding Are Affected Oppositely by Different Adaptation Mechanisms. *Journal of neuroscience* 28(50):13649–13661.

[141] Gjorgjieva J, Mease RA, Moody WJ, Fairhall AL (2014) Intrinsic Neuronal Properties Switch the Mode of Information Transmission in Networks. *PLoS Computational Biology* 10(12):e1003962–19.

[142] Schäfer R, Vasilaki E, Senn W (2009) Adaptive Gain Modulation in V1 Explains Contextual Modifications during Bisection Learning. *PLoS Computational Biology* 5(12):e1000617–12.

[143] Atiani S, Elhilali M, David SV, Fritz JB, Shamma SA (2009) Task Difficulty and Performance Induce Diverse Adaptive Patterns in Gain and Shape of Primary Auditory Cortical Receptive Fields. *Neuron* 61(3):467–480.

[144] Williamson RS, Ahrens MB, Linden JF, Sahani M (2016) Input-Specific Gain Modulation by Local Sensory Context Shapes Cortical and Thalamic Responses to Complex Sounds. *Neuron* 91(2):467–481.

[145] Angeloni C, Geffen MN (2018) Contextual modulation of sound processing in the auditory cortex. *Current opinion in neurobiology* 49:8–15.

[146] Chance FS, Abbott LF, Reyes AD (2002) Gain modulation from background synaptic input. *Neuron* 35(4):773–782.

[147] Cardin JA, Palmer LA, Contreras D (2008) Cellular Mechanisms Underlying Stimulus-Dependent Gain Modulation in Primary Visual Cortex Neurons In Vivo. *Neuron* 59(1):150–160.

[148] Carvalho TP, Buonomano DV (2009) Differential Effects of Excitatory and Inhibitory Plasticity on Synaptically Driven Neuronal Input-Output Functions. *Neuron* 61(5):774–785.

[149] Barkai E, Hasselmo ME (1994) Modulation of the input/output function of rat piriform cortex pyramidal cells. *Journal of Neurophysiology* 72(2):644–658.

[150] Soma S, Shimegi S, Osaki H, Sato H (2012) Cholinergic modulation of response gain in the primary visual cortex of the macaque. *Journal of Neurophysiology* 107(1):283–291.

[151] Soma S, Shimegi S, Suematsu N, Sato H (2013) Cholinergic modulation of response gain in the rat primary visual cortex. *Scientific Reports* 3(1):159–7.

[152] Himmelheber AM, Sarter M, Bruno JP (2000) Increases in cortical acetylcholine release during sustained attention performance in rats. *Brain research. Cognitive brain research* 9(3):313–325.

[153] Parikh V, Kozak R, Martinez V, Sarter M (2007) Prefrontal Acetylcholine Release Controls Cue Detection on Multiple Timescales. *Neuron* 56(1):141–154.

[154] Kozak R, et al. (2007) Toward a Neuro-Cognitive Animal Model of the Cognitive Symptoms of Schizophrenia: Disruption of Cortical Cholinergic Neurotransmission Following Repeated Amphetamine Exposure in Attentional Task-Performing, but Not Non-Performing, Rats. *Neuropsychopharmacology* 32(10):2074–2086.

[155] Vertes RP, Kocsis B (1997) Brainstem-diencephalo-septohippocampal systems controlling the theta rhythm of the hippocampus. *Neuroscience* 81(4):893–926.

[156] Alger BE, Nagode DA, Tang AH (2014) Muscarinic cholinergic receptors modulate inhibitory synaptic rhythms in hippocampus and neocortex. *Frontiers in Synaptic Neuroscience* 6(SEP):18.

[157] Zhang H, Lin SC, Nicolelis MAL (2010) Spatiotemporal Coupling between Hippocampal Acetylcholine Release and Theta Oscillations In Vivo. *Journal of neuroscience* 30(40):13431–13440.

[158] Mizuseki K, Buzsáki G (2013) Preconfigured, Skewed Distribution of Firing Rates in the Hippocampus and Entorhinal Cortex. *CellReports* 4(5):1010–1021.